University of Ljubljana
Faculty of Civil and Geodetic Engineering

DOKTORSKI ŠTUDIJSKI
PROGRAM III. STOPNJE
GRAJENO OKOLJE

Kandidat:
MITJA PAPINUTTI

DINAMIČNA ANALIZA PLAVAJOČIH MOSTOV

Doktorska disertacija

DYNAMIC ANALYSIS OF FLOATING BRIDGES

Doctoral thesis

Ljubljana, maj 2021

University of Ljubljana
Faculty of Civil and Geodetic Engineering

Candidate:
MITJA PAPINUTTI

DYNAMIC ANALYSIS OF FLOATING BRIDGES

Doctoral thesis

Supervisor:
Prof. Boštjan Brank, Ph.D, University of Ljubljana, Slovenia

Cosupervisor:
Prof. Ole Øiseth, Ph.D, Norwegian University of Science and Technology, Norway

Ljubljana, May 2021

Mentor:	red. prof. dr. Boštjan Brank,	UL FGG
Somentor:	red. prof. dr. Ole Øiseth,	NTNU Trondheim

Poročevalci za oceno doktorske disertacije:

Član:	red. prof. dr. Nils Erik Anders Rønnquist,	NTNU Trondheim
Član:	red. prof. dr. Stojan Kravanja,	FGPA Maribor
Član:	izr. prof. dr. Dušan Žagar,	FGG Ljubljana

Lektura slovenskega jezika:

dr. Kaja Jošt

Lektura angleškega jezika:

American Journal Experts

Errata

Page	Line	Error	Correction

Bibliografsko-dokumentacijska stran in izvleček

UDK: 624.04:624.87(043)
Avtor: Mitja Papinutti
Mentor: red. prof. dr. Boštjan Brank
Somentor: red. prof. dr. Ole Øiseth
Naslov: Dinamična analiza plavajočih mostov
Obseg in oprema: 103 str., 4 pregl., 43 sl., 167 en., 99 virov
Ključne besede: dimenzioniranje plavajočih mostov, dinamika mostov, časovna integracija odziva, vetrna analiza, odvodi omahovanja, obtežba valov, obtežba morskih tokov

Izvleček:
Plavajoči mostovi so zasnovani za premagovanje velikih morskih razponov, katerih premostitve niso mogoče s konvencionalnimi rešitvami. Plavajoče mostove pogosto zaznamuje vitkost in so umeščeni neposredno na območja visokih morskih valov ter močnih vetrov. Dinamičen odziv pogosto pomembno vpliva na samo zasnovo mostu. Doktorsko delo predstavlja numerično modeliranje različnih zunanjih obtežb, kot so: obtežba turbulentnega vetra, aeroelastični odziv, radiacija valov, obtežba valov, viskozno dušenje vode, podvodni tokovi itd. Predstavljene obtežbe so izračunane s pomočjo časovne integracije, ki natančno izračunava nelinearne vezane dinamične enačbe konstrukcije. Podrobneje je predstavljeno vetrno modeliranje aeroelastičnega dušenja in togosti, v literaturi pogosto uporabljeni so kvazistatični modeli in modeli odvodov omahovanja. Prispevek k znanosti predstavlja na novo razvit matematični model aeroelastičnega odziva, ki temelji na vhodnih podatkih odvodov omahovanja. Razviti model je primeren za uporabo v različnih programskih kodih za izračun dinamike mostov v praksi. Numerični modeli so laboratorijsko testirani v vetrovniku na trondheimski univerzi.

Bibliographic-documentalist information and abstract

UDC: 624.04:624.87(043)
Author: Mitja Papinutti
Supervisor: Prof. Boštjan Brank, Ph.D.
Cosupervisor: Prof. Ole Øiseth, Ph.D.
Title: Dynamic analysis of floating bridges
Notes: 103 p., 4 graph., 43 fig., 167 eq., 99 ref.
Key words: floating bridge design, bridge dynamics, time integration, wind analyses, flutter derivatives, wave loads, current loads

Abstract:
The floating bridge is an ambitious structure that enables new long-span sea crossings. Floating structures are susceptible to dynamics due to their slender structures and interactions with the surrounding environment. The dynamic response can govern the floating bridge design; therefore, an accurate and representative dynamics model is crucial. This thesis provides a comprehensive overview of all the relevant environmental loads, such as turbulent wind loads, self-excited wind loads, wave radiation loads, wave loads, and viscous drag damping currents. All modeling is suited for a time-domain integration method that successfully calculates the nonlinear correlated bridge response. Different state-of-the-art wind self-excited modeling techniques are presented, such as the quasi-steady state and flutter derivative techniques. The scientific contribution is a new velocity convolution of the flutter derivative model based on the theory of linear flutter derivatives. The proposed models are designed to be successfully introduced into various commercial codes, thus allowing more integrative wind designs in practice. The newly developed models are also experimentally validated in the Norwegian University of Science and Technology wind tunnel.

Acknowledgments

I want to express my gratitude to the Norwegian Public Road Administration for their research support. The main contributors enabling my research are Veie Johannes, Holtberget Simen Hellgren and Eidem Mathias Egeland. I also wish to thank my supervisor Boštjan Brank and professor Matjaž Četina for their contribution to my Ph.D. thesis. Special gratitude is extended to my cosupervisor Ole Øiseth for his guidance regarding my research on self-excited force modeling. His assistance made this research possible and helped shape this excellent research work. Many thanks are also given for the outstanding scientific discussion with Yuwang Xu and Øyvind Wiig Petersen from NTNU Trondheim.

I want to acknowledge Arne Bruer, Mathias Huuse Marley, and Jørgen Kvaleid from COWI Oslo for sharing their experience with on floating bridge projects. Special thanks to Ketil Aas Jakobsen and Lars Halvor Kaasa from Dr. Ing. A. Aas-Jakobsen AS Oslo. Our project work made a significant contribution to my understanding of floating bridge responses and added value to this thesis. The effective algorithm coding and outstanding software development presented in this work were made possible by experienced software developer Joerg Sello and product manager Johan Stampler from Bentley Graz. I also appreciate the software support from Rakesh Pathak, Afshin Hatami and Lee Tanase from Bentley Infrastructure Exton.

I offer my thanks to all the bridge design experts, software developers, researchers and organizations for their contributions to this work. The research objective was to open up new crossing possibilities and establish a basis for different disciplines to work together. I hope that some of the ideas presented find application in future infrastructural projects.

University of Ljubljana
Faculty of Civil and Geodetic Engineering

NTNU
Norwegian University of Science and Technology

Statens vegvesen

AAS-JAKOBSEN

COWI

Bentley

WIND
onDemand

My sincerest gratitude goes to my parents Rosita and Ludvik Papinutti. Throught their own hard work and respect for other people's efforts, they taught me two important values that have guided my entire career.

<I dedicate this work to my wife Alja Papinutti and

to the beautiful family we have created together>

INDEX

1 INTRODUCTION

A long-term goal of Norwegian society is to develop the E39 as an improved and continuous Coastal Highway Route between the cities of Kristiansand and Trondheim. A political decision was made in 2017 in the National Transport Plan to build a motor highway route approximately 1100 km long to connect the coastal Norwegian cities of Stavanger, Bergen, Ålesund and Molde. Travel among these cities today requires approximately 21 hours and should be reduced to 11 hours. The aim is to create and improve E39 as a continuous connection without the need for ferries, resulting in the reduction in the route length by almost 50 km. The travel time will be reduced by replacing ferries with bridges and tunnels, in addition to upgrading several road sections on land. This goal will be managed by the Public Road Administration in Norway (Statens Vegvesen). Several aspects are evaluated in detail to improve highway connections from the aspects of society, safety, the environment, economics and engineering. This thesis explores the numerical analysis tools required to design bridge crossings that will be supported by floating pontoons. A series of projects were launched to find feasible technological solutions that will make fjord crossings possible. The feasibility studies investigated possible crossings of an extralong suspension bridge, a multispan suspension bridge founded on tension leg platform (TLP) supports, an underwater tunnel floating 20 m below the surface and a multipontoon cable-stayed bridge. The best-suited crossing alternative will depend on the environmental and geographical conditions of the fjord.

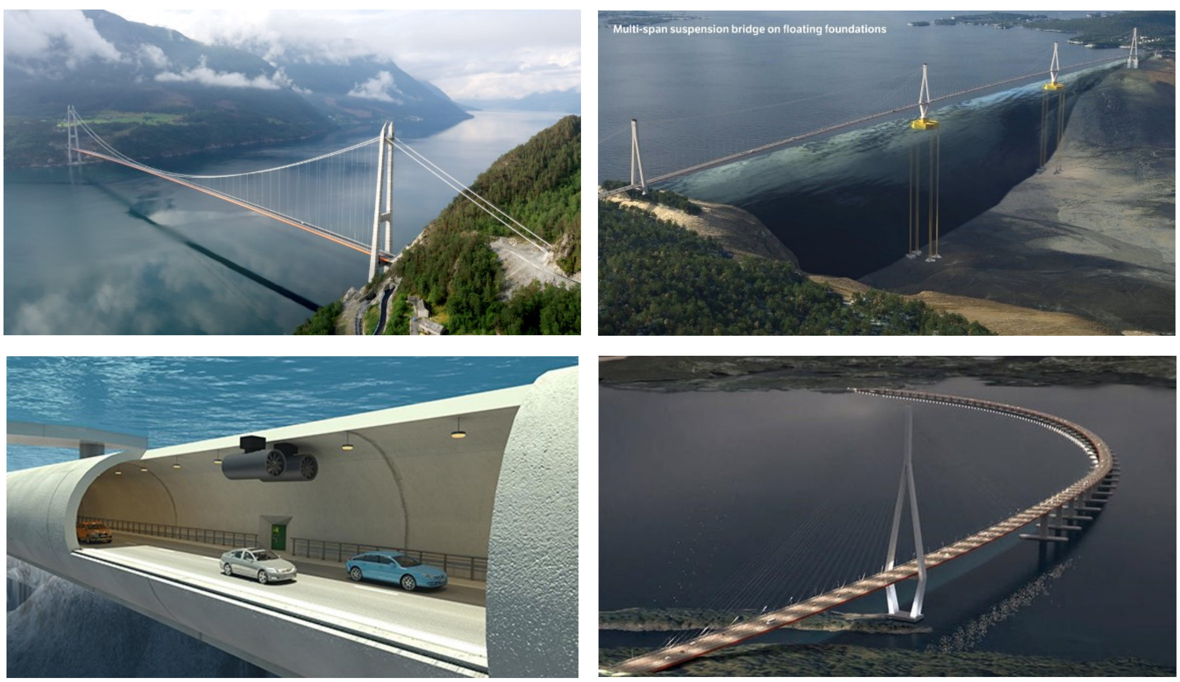

Figure 1-1: Crossing possibilities, long suspension bridge, floating bridge, underwater tunnel, pontoon bridge [1].
Slika 1-1:Premostitvene možnosti, viseči most, plavajoči most, podvodni tunel, pontonski most [1].

This research work is based on the experience gained in the bridge design industry sector and has been conducted in parallel with the author's full-time work on different bridge projects, which offers important assistance to the floating bridge design. The development of a new floating bridge concept is made possible by the multidisciplinary knowledge gained from different engineering disciplines, combining the efforts of bridge designers, marine engineers, researchers and software developers. This thesis provides an overview of all relevant environmental loads, with an emphasis on alternative dynamic wind load formulations. The new floating bridges are dominated by the dynamic excitation introduced by waves and turbulent winds. Therefore, these structures require new analysis tools to fully capture their complex dynamic responses to better understand their structural behavior and achieve efficient bridge designs. While individual environmental loads are successfully managed by industry, the simultaneous coupled response of all environmental loads is important to consider when attemption to understand the complex dynamic responses. To capture various dynamic loads and represent the nonlinear response of the bridge, the fully coupled nonlinear time-domain scheme was used. The combination of several engineering disciplines resulted in a lack of available numerical tools, giving rise to different research and commercial code development projects. This research work was implemented in the sophisticated commercial bridge software *RM Bridge*, which has been applied to several feasibility study designs. The author's main work has been to develop the required software extension for wind and wave calculations, which has involved theoretical investigation, individual load algorithm design, code implementation and testing work. The development extensions were achieved through an accumulation of knowledge from different engineering disciplines; individuals from these disciplines engaged in brainstorming exercises together to find optimal solutions for the given environmental load formulation. The developed mathematical models have been validated by software and applied to large finite element model bridges. Their successful implementation enables this work to be applied to any floating bridge type, making it possible for researchers and designers to continue this work. The final developed numerical models are suitable to calculate complex dynamic response load scenarios. The numerical tools of this thesis can provide accurate design values that will make floating bridge design safe and reliable. The presented work can be applied as a guideline for dynamical bridge analysis, helping investors achieve efficient design and, thus, reduce the project costs.

1.1 Current research

In structural engineering, the commonly applied and well-investigated time-integration methods are suitable for the evaluation of nonlinear structural responses. Long slender floating structures are subject to large displacement and rotations, where a third-order finite element formulation must be applied. For most linear systems, the frequency domain will provide accurate results, whereas nonlinear responses and nonlinear loads are best solved by time-domain algorithms. Hence, the time-domain method is chosen as the investigation tool for the final bridge design. A popular Newmark method can be applied to model geometrical nonlinear floating bridge responses, allowing the analysis of fully coupled hydrodynamic and aerodynamic effects. This implicit method offers longer time steps and shorter simulation times. A Newmark integration scheme is implemented in the *RM Bridge* software in this research investigation, as in [2]. This method was designed to resolve geometrical nonlinear and material nonlinear effects, various nonlinear loads and self-excited loads. A short overview of the applied time-integration code is presented in chapter 2.

The hydrodynamic effects are introduced in chapter 3, and the dynamic wind load is introduced in chapter 4. The environmental loads on a bridge can be further divided into constant, time-dependent loads and self-excited loads depending on the structural motion. The load formulation must be transformed into a selected time-domain [3] or frequency-domain [4] framework; here, time-domain transformations are investigated in detail. Both wind and wave self-excited loads are, per definition, linearized frequency-dependent matrix functions, representing the harmonic superposition of individual frequencies. The loads cannot be directly applied to the Newmark time-integration scheme since loads cannot be expressed as constant matrices of time or displacement vectors. The transformation into a time domain requires the environmental forces to be described as time-dependent signals, which is made possible by convolution integral transformation, presenting the frequency-dependent environmental loads as time vectors. The two-step convolution transformation first involves calculating the inverse Fourier transform (IFT) of a load and then transforming it into an impulse response function. In the second step, the convolution reflects the impulse response signal of the structural response or the corresponding time derivative. The underlying linear invariant causal theory can be applied to all time-domain transformations and is derived in detail in [5]. The convolution integration is evaluated at each time step and can result in time-intensive calculations. The classic convolution integration approach computes the convolution integral for all past motions in each nonlinear time step. Recently, the very popular state-space formulation has been used to transform the convolution integral into a first-order load equation as a combination of matrix operations [6]. State-space methods are computationally efficient; however, they require special fitted functions and user experience. In this research, a traditional convolution theorem was used and was found to deliver the required specifications. The implemented interface was specifically developed in commercial software used to conduct time-integration simulations of floating bridges [7] [8].

The hydrodynamic effects are well investigated in the offshore industry. In the past few decades, oil rigs have been successfully built in the tumultuous North Sea. Marine engineers have access to various hydrodynamic load formulations and corresponding commercial analysis tools [9]. Offshore hydrodynamic effects are not commonly present in regular bridge design; therefore, new extensions to the Newmark scheme are required. The potential theory can be applied to numerically evaluate the properties of hydrodynamic floaters, for which specialized hydrodynamic software can be a good choice [10]. Hydrodynamic properties such as hydrodynamic damping, hydrodynamic stiffness, hydrodynamic added mass and wave loads fully describe the bridge-water interaction. The precalculated input can be prepared by external hydrodynamic specialist groups. The self-excited wave radiation and wave loads fully describe the bridge motion in the wave environment. This can be resolved by the convolution theorem, where an interface has been built into the Newmark time-integration scheme in the floating bridge context [11] [12] [13] [14] [15] [16] [17] [18] [19] [20] [21].

The dynamic wind analysis examines a superposition of the incoming mean wind, turbulent wind and structure motion. The structure motion can be expressed by a linearized quasi-steady-state (QSS) formulation under the assumption of a fully developed flow. This wind interaction is described by constant aerodynamic damping and stiffness matrices. The QSS formulation might be suitable for examining the linear response under low wind speeds and is convenient for Newmark implementation. However, it neglects different coupling and aeroelastic effects. This method was successfully implemented in the Newark time-integration scheme and is the latest state-of-the-art wind tool for designing floating bridge projects [4]. However, the QSS load model is not suitable for the investigation of aeroelastic effects and delivers nonconservative response results, leading to a less economical and perhaps less safe bridge design. This research proposes an improvement involving the use of the flutter derivative model inside the current time-domain framework used for the analysis of floating bridges. Dimensionless flutter derivatives are wind-tunnel-measured results related to the movement of a section under laminar wind [22]. According to Scanlan regarding linear aeroelastic theory [23], the measured forces are a function of the reduced frequency, represented by eighteen functions arranged in the aeroelastic damping and aeroelastic stiffness. This self-excited wind interaction load model is suitable for aeroelastic instability and accurate wind buffeting responses [6]. Commonly scattered and available for limited frequency, flutter derivatives require some interpolation and extrapolation of data. The common rational function and indicial function models are well established to simulate aeroelastic effects. The time-domain transformation requires a more sophisticated approach. Specifically, designed functions fitted to the flutter derivatives have an analytical transformation solution in the time domain. The indicial functions approach is an approximative force model combining the QSS and self-excited models [24]. Rational functions are commonly used for wind self-excited load formulation; thus, they agree well with wind tunnel measurements. To fulfill the causal dynamic system requirement, the functions are simultaneously fitted to both the damping and stiffness functions, thus requiring a complex multiparameter nonlinear fitting [25]. This formulation is robust, behaves well for the limited frequency range data available and delivers an accurate self-excited force result. Analytically derived rational functions are resolved by a convolution integral. Hence, the rational function is a well-suited candidate for improving the current fully coupled time-domain floating bridge response analysis. The currently available rational functions are however, not suitable for implementation in the presently used time-domain floating bridge frameworks due to a lack of programming access to commercial code. As a result, researchers are motivated to find a possible rational function reformulation for convolution integration to fit inside the already available hydrodynamic implementation. The research work focuses on delivering reformulated self-excited load formulations in the form of aeroelastic damping tables using convolution over velocity routines in hydrodynamic wave radiation damping. A reformulation suitable for direct use could not be found in the available literature, leading to the development of a suitable numerical model for the current time-domain analysis framework. These research efforts provide a working model for floating bridge projects; thus, this research provides a unique contribution to the field. The work has also improved and simplified many aspects of the current rational function. In recent years, free and forced vibration wind tunnel tests have improved the quality of the extracted data and resulted in less scattered data. Thus, alternative nonparametric fitted functions, such as polynomial functions, are now made possible by independent fitting to the aeroelastic damping and stiffness functions.

Floating bridge analysis involves several disciplines, each belonging to the corresponding research area. A more comprehensive literature overview is provided in each subsequent chapter of this thesis, and different formulation alternatives are discussed. Few studies can be found on the dynamic excitation of floating bridges since it is a relatively new research field consisting of a combination of existing research areas. This work offers an overview of all relevant environmental load formulations and corresponding load assumptions. Several conventional load linearizations may no longer be valid for flexible floating bridge design. Therefore, a representative formulation of each load must be provided to ensure that the relevant dynamic effects are well investigated for these new bridge structures. Dynamic loads govern bridge designs; hence, accurate dynamic prediction is crucial. To achieve this goal, significant contributions in several aspects must be made, e.g., from the available and representative environmental measurements, by competent designers and from the available analysis tools, which is the focus of this monograph.

1.2 Thesis goals

This research provides a comprehensive overview of the environmental loads on floating structures. All environmental loads have been incorporated into the time-domain framework [26]. The current state-of-the-art wind implementations of the QSS wind buffeting theory have some room for improvement. The main goal of this thesis is to introduce a more accurate self-excited wind formulation into floating bridge design. Wind tunnel measurements have been confirmed to be well in line with linear self-excited models and thus are important to consider for any future floating bridge concept. Overall, self-excitation in the time domain is widely used in research investigations; however, it is commonly avoided in bridge design. The commonly applied self-excited models require specifically tailored fitted functions; thus, they require user expertise and developing a fully automated numerical procedure is difficult. This situation also presents a practical challenge for any commercial code developer and is the reason why commercial codes have not yet been implemented in time-domain floating bridge analysis. The goal is to find a suitable self-excited formulation that can be directly applied in the current time-domain analysis framework. Various self-excited wind load models are presented as candidates for various computer codes. The most important goal of this thesis is to reduce the practical challenges of self-excited models and make them more accessible to bridge designers. The developed self-excited load models should be suited for incorporation into the current time-domain framework, which can result in a reduction in the amount of software needed, thus reducing the modeling effort and the complexity of the simulations. The proposed framework can provide immediate feedback on various structural changes or different load scenarios. These compelling arguments can result in efficient design and immediate feedback on the nonlinear structural performance. This goal was accomplished by developing a new self-excited force model, which was evaluated by comparison with wind tunnel measurements.

The main objectives of this research can be summarized as follows:

- to provide an overview of the dynamic loads on floating bridges;
- to develop a new self-excited load model;
- to develop a load model suitable for future project work;
- to build on the already collected knowledge base of floating bridges and the available numerical tools;
- to mathematically simplify the complex self-excited formulation, if possible.

The environmental forces on a TLP floating bridge example are demonstrated, including the coupled hydrodynamic and wind load effects.

The testable hypothesis is the validation of a self-excited wind load model that is suitable for implementation in the time-integration dynamic equation of motion. Scientific validation is achieved by numerical tests and wind tunnel experiments.

2 DYNAMIC STRUCTURAL ANALYSIS

This chapter provides some insight into the dynamic calculation of floating structures. An overview of the possible dynamic solution algorithms in structural dynamic engineering is provided. In detail, linear and nonlinear time marching algorithms are discussed to resolve the dynamic equations of motion. The equations are resolved to extract the design values of the displacements and inner forces. Some guidelines on how to introduce proper modeling and input for the analysis of floating structures are provided. Two main groups of methods exist, i.e., frequency-domain and time-domain formulations. Both deliver equivalent results for a linear response; however, the time-domain methods are preferred in nonlinear response calculations. For each group method, different numerical algorithms and possibilities for resolving motion equations exist, depending on the type of problem. For the time-domain methods, the equations of motion are integrated over time, and the results are time-dependent signals of structural motion. Time-integration methods are very suitable for solving complex nonlinear and coupled equations of motion since the integration algorithms can resolve nonlinearities iteratively. These methods are very suitable for the dynamic analysis of floating bridges and are considered the most accurate methods. The frequency-domain methods are based on linearized decomposed dynamic systems and reduce large structural matrix systems into smaller modal equivalent systems. Eigenvalue decomposition is calculated by rotating the symmetric coupled dynamic equation and is possible for most civil structures. Modal decomposition methods are frequently used and provide valuable information on structural frequencies and their participation. Frequency-domain methods are favorable due to their computationally efficient algorithms, which can be extended to resolve nonsymmetrical coupled motion and thus are suitable for the investigation of wind and wave load effects. The main properties of both analysis methods are presented in the following table:

Table 2-1: Frequency- and time-domain methods for response calculations [2].

Preglednica 2-1: Primerjava frekvenčne in časovne metode računa odziva mostu [2].

Parameter	**Time domain**	**Frequency domain**
Linear system	Excellent	Excellent
Nonlinear – Large displacements	Excellent	Acceptable
Nonlinear – Material hysteretic	Excellent	Poor
Coupled loads	Excellent	Acceptable
Motion-induced loads	Excellent	Acceptable
Calculation speed	Poor	Excellent
General accuracy	Excellent	Acceptable
Structural damping definition	Poor	Excellent
Transient calculation	Excellent	Poor

2.1 Equations of motion

The equations of motion of a linear structure discretized in space by a mesh of finite elements can be written as flows:

$$\mathbf{M}\ddot{\mathbf{u}}(t)+\mathbf{C}\dot{\mathbf{u}}(t)+\mathbf{K}\mathbf{u}(t)=\mathbf{f}_{\text{ext}}(t) \tag{2.1}$$

Here, $\mathbf{M}$, $\mathbf{C}$ and $\mathbf{K}$ are the structural mass, damping and stiffness matrices, respectively; $\boldsymbol{f}_{\text{ext}}$ is the external loading vector; $\ddot{\mathbf{u}}, \dot{\mathbf{u}}$ and $\mathbf{u}$ are vectors of the nodal accelerations, velocities and displacements, respectively; $t \in [t_o = 0, \ldots, t_{\text{fin}}]$ is a time parameter; t_{fin} is the final time of interest; and each dot indicates the derivative with respect to time.

If nonlinearities are taken into account, such as geometric nonlinearity, nonlinear (and inelastic) material models, moving masses acting on the structure, nonlinear structural damping, and position-, velocity- and acceleration-dependent loads, equation (2.1) is replaced by the following equation:

$$\mathbf{M}(t)\ddot{\mathbf{u}}(t)+\mathbf{C}(\mathbf{u})\dot{\mathbf{u}}(t)+\mathbf{F}(\mathbf{u}(t))=\mathbf{f}_{\text{ext}}(t,\ddot{\mathbf{u}},\dot{\mathbf{u}},\mathbf{u}) \tag{2.2}$$

The displacement-dependent inner restoring forces $\boldsymbol{F}(\boldsymbol{u}(t))$ arise if large displacements/rotations and nonlinear (and inelastic) material models are considered. In bridge analysis, an example of geometric nonlinearities is cable effects (including cable sagging). Material nonlinear models that take into account cross-sectional steel yielding and concrete cracking also contribute to $\boldsymbol{F}$. The time-dependent mass matrix $\mathbf{M}$ may be due to the moving masses of traffic. For the time-varying structural mass and stiffness, the Rayleigh damping $\mathbf{C} = \alpha\mathbf{M} + \beta\mathbf{K}$ also changes with time. The external load vector $\mathbf{f}_{\text{ext}}$ can be quite complex. Hydrodynamic radiation-damping loads are commonly described as acceleration- and velocity-dependent loads. They are represented by the hydrodynamic mass $\mathbf{M}_{\text{hy}}$ and damping $\mathbf{C}_{\text{hy}}$ matrix. Wind self-excited forces are represented as velocity- and displacement-dependent loads. They are usually represented by aeroelastic damping $\mathbf{C}_{\text{se}}$ and stiffness $\mathbf{K}_{\text{se}}$ matrices. The loading vector also includes nonlinear viscous forces and structural viscus dampers.

In this work, author considers an equation of the form of (2.2) for a time-domain analysis of floating bridges subjected to environmental loads. For the integration of (2.2) with respect to time, a time-stepping schemes available in the *RM Bridge* commercial computer code [2] is used.

2.2 Time-stepping scheme

The systems of equations of motion of (2.1) and (2.2) are solved numerically by introducing discretization in time. The solutions are searched for at discrete time points $t_0, \cdots, t_{\text{n-1}}, t_{\text{n}}, t_{\text{n+1}}, t_{\text{fin}}$. Various solution methods are available, which are called time-stepping schemes or time-integration schemes for linear structural elastodynamics [27]. Many of them are also used for nonlinear structural dynamics. The methods are usually divided into two groups, i.e., explicit and implicit structural dynamic time-stepping schemes. The explicit methods compute the solution at $t_{\mathrm{n+1}}$ by using a known solution at t_{n} and known time derivatives at t_{n}. The implicit time-stepping schemes compute the solution at $t_{\mathrm{n+1}}$ by using a known solution at t_{n} and time derivatives at $t_{\mathrm{n+1}}$. The explicit methods are only conditionally stable. To be stable, they demand very small time steps. The implicit methods can be unconditionally stable for linear systems. They are much more accurate than the explicit schemes.

In the following, a brief describtion the implicit version of the Newmark family of time-stepping schemes is provided. The Newmark family of algorithms is commonly used to solve linear and nonlinear equations of motion, i.e., (2.1) and (2.2). By changing the values of the Newmark parameters, which are commonly denoted as β and γ, one can obtain different time-stepping schemes [28]. The parameter values are in the range of $1/6 \leq \beta \leq 1/4$ and $0 \leq \gamma \leq 1/2$. The value $\beta = 1/4$ yields an implicit constant acceleration scheme, and $\beta = 1/6$ yields an implicit linear acceleration scheme. Setting $\beta = 0$ and $\gamma = 1/2$ gives the explicit central difference method. The recommended value for the parameter γ is $1/2$, since only this value guarantees the second-order accuracy of the Newmark algorithm. Other values for γ provide only first-order-accurate Newmark algorithms but add numerical damping, which in many cases acts in a favorable manner.

Below is present derivation of the Newmark algorithm. The equilibrium equation for a linear problem is expressed in incremental form as follows:

$$\mathbf{M}\Delta\ddot{\mathbf{u}} + \mathbf{C}\Delta\dot{\mathbf{u}} + \mathbf{K}\Delta\mathbf{u} = \Delta\mathbf{f} \tag{2.3}$$

where:

$$\begin{aligned}
\Delta\mathbf{u} &= \mathbf{u}_{\mathrm{n+1}} - \mathbf{u}_{\mathrm{n}} \\
\Delta\dot{\mathbf{u}} &= \dot{\mathbf{u}}_{\mathrm{n+1}} - \dot{\mathbf{u}}_{\mathrm{n}} \\
\Delta\ddot{\mathbf{u}} &= \ddot{\mathbf{u}}_{\mathrm{n+1}} - \ddot{\mathbf{u}}_{\mathrm{n}} \\
\Delta\mathbf{f} &= \mathbf{f}_{\mathrm{n+1}} - \mathbf{f}_{\mathrm{n}}
\end{aligned} \tag{2.4}$$

Using a Taylor series yields the folowing:

$$\mathbf{u}_{\mathrm{n+1}} = \mathbf{u}_{\mathrm{n}} + \Delta t\dot{\mathbf{u}}_{\mathrm{n}} + \frac{1}{2}\Delta t^2\ddot{\mathbf{u}}_{\mathrm{n}} + \frac{1}{6}\Delta t^3\dddot{\mathbf{u}}_{\mathrm{n}} + \cdots \tag{2.5}$$

Thus,

$$\Delta\mathbf{u} = \Delta t\dot{\mathbf{u}}_{\mathrm{n}} + \frac{1}{2}\Delta t^2\ddot{\mathbf{u}}_{\mathrm{n}} + \frac{1}{6}\Delta t^3\dddot{\mathbf{u}}_{\mathrm{n}} + \cdots \tag{2.6}$$

The time derivative of (2.6) gives:

$$\Delta\dot{\mathbf{u}} = \Delta t\ddot{\mathbf{u}}_{\mathrm{n}} + \frac{1}{2}\Delta t^2\dddot{\mathbf{u}}_{\mathrm{n}} + \cdots \tag{2.7}$$

For assumed linear acceleration, the third derivative may be expressed by:

$$\dddot{\mathbf{u}}_{\mathrm{n}} = \frac{d\ddot{\mathbf{u}}}{dt} = \left(\frac{\ddot{\mathbf{u}}_{\mathrm{n+1}} - \ddot{\mathbf{u}}_{\mathrm{n}}}{\Delta t} \right) = \frac{\Delta\ddot{\mathbf{u}}}{\Delta t} \tag{2.8}$$

Figure 2-1 presents the third-derivative approximation with the linear acceleration assumption derived in (2.8).

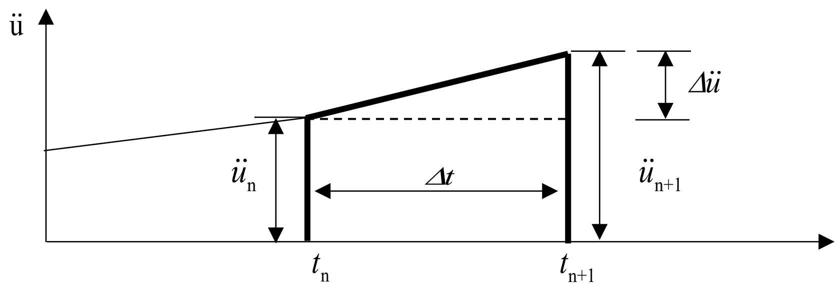

Figure 2-1: Approximation of the third-order term for linear acceleration.

Slika 2-1: Aproksimacija linearnega pospeška tretjega reda.

The parameter γ is introduced in (2.7) to model the third-order and higher-order terms as:

$$\Delta\dot{\mathbf{u}} = \Delta t\ddot{\mathbf{u}}_{\mathrm{n}} + \gamma\Delta t\Delta\ddot{\mathbf{u}} \tag{2.9}$$

and the parameter β in (2.6), in a similar fashion, is introduced in:

$$\Delta\mathbf{u} = \Delta t\dot{\mathbf{u}}_{\mathrm{n}} + \frac{1}{2}\Delta t^2\ddot{\mathbf{u}}_{\mathrm{n}} + \beta\Delta t^2\Delta\ddot{\mathbf{u}} \tag{2.10}$$

A comparison of (2.9) and (2.7) with (2.10) and (2.6) yields the parameters $\gamma = 1/2$ and $\beta = 1/6$ for linear acceleration. The average acceleration or trapezoidal rule gives $\gamma = 1/2$ and $\beta = 1/4$ and is commonly used for structural dynamics problems.

The acceleration increment $\Delta\ddot{\mathbf{u}}$ is expressed based on (2.10) as:

$$\Delta\ddot{\mathbf{u}} = \frac{1}{\beta\Delta t^2}\Delta\mathbf{u} - \frac{1}{\beta\Delta t}\dot{\mathbf{u}}_{\mathrm{n}} - \left(\frac{1}{2\beta} - 1 \right)\ddot{\mathbf{u}}_{\mathrm{n}} \tag{2.11}$$

Inserting (2.11) into (2.9) yields:

$$\Delta\dot{\mathbf{u}} = \frac{\gamma}{\beta\Delta t}\Delta\mathbf{u} + \left(1 - \frac{\gamma}{\beta} \right)\dot{\mathbf{u}}_{\mathrm{n}} + \Delta t\left(1 - \frac{\gamma}{2\beta} \right)\ddot{\mathbf{u}}_{\mathrm{n}} \tag{2.12}$$

Inserting (2.11) into the incremental equation of motion (2.3) gives:

$$\begin{aligned} &\mathbf{M}\left\{ \frac{1}{\beta\Delta t^2}\Delta\mathbf{u} - \frac{1}{\beta\Delta t}\dot{\mathbf{u}}_{\mathrm{n}} - \left(\frac{1}{2\beta} - 1 \right)\ddot{\mathbf{u}}_{\mathrm{n}} \right\} + \\ &\mathbf{C}\left\{ \frac{\gamma}{\beta\Delta t}\Delta\mathbf{u} + \left(1 - \frac{\gamma}{\beta} \right)\dot{\mathbf{u}}_{\mathrm{n}} + \Delta t\left(1 - \frac{\gamma}{2\beta} \right)\ddot{\mathbf{u}}_{\mathrm{n}} \right\} + \mathbf{K}\Delta\mathbf{u} = \Delta\mathbf{f} \end{aligned} \tag{2.13}$$

The effective dynamic stiffness $\bar{\mathbf{K}}$ collects terms with displacement increments $\Delta\mathbf{u}$. The effective dynamic increment force $\Delta\bar{\mathbf{F}}$ collects the known terms in (2.13).

$$\bar{\mathbf{K}} = \mathbf{K} + \frac{1}{\beta \Delta t^2}\mathbf{M} + \frac{\gamma}{\beta \Delta t}\mathbf{C}$$

$$\Delta\bar{\mathbf{F}} = \Delta\mathbf{f} + \mathbf{M}\left\{\frac{1}{\beta\Delta t}\dot{\mathbf{u}}_{\mathrm{n}} + \frac{1}{2\beta}\ddot{\mathbf{u}}_{\mathrm{n}}\right\} + \mathbf{C}\left\{\left(1-\frac{\gamma}{\beta}\right)\dot{\mathbf{u}}_{\mathrm{n}} + \Delta t\left(1-\frac{\gamma}{2\beta}\right)\ddot{\mathbf{u}}_{\mathrm{n}}\right\} \tag{2.14}$$

The dynamic equilibrium is written in incremental form as:

$$\bar{\mathbf{K}}\Delta\mathbf{u} = \Delta\bar{\mathbf{F}} \tag{2.15}$$

If $\bar{\mathbf{K}}$ is symmetric, (2.15) is commonly solved by using $\mathbf{LDL}$ factorization. The solution results are incremental displacements $\Delta\mathbf{u}$. These incremental displacements are inserted in (2.11) and (2.12) to calculate the increments $\Delta\ddot{\mathbf{u}}, \Delta\dot{\mathbf{u}}$, which are then inserted into (2.4) to evaluate the structural displacements. This procedure presents a solution for the linear dynamic equation in (2.1).

In Figure 2-2, a solution scheme for the nonlinear dynamic system (2.2) is depicted. This scheme is implemented in *RM Bridge* [2], which is further used in this work for computations of the responses of a floating bridge.

$\mathrm{n} = 0,1,2,...$ solution at $t_{\mathrm{n+1}} = t_{\mathrm{n}} + \Delta t$

$\mathrm{j} = 1,2,..., j_{tot}$ $\quad \Delta t = \Delta t j_{tot} / j$ timestep length

$i = 1,2,...$ Newton-Raphson iterations

Average structural properties:	$\mathbf{M}_{\mathrm{i+1}} = \dfrac{\mathbf{M}_{\mathrm{i}} + \mathbf{M}_{\mathrm{n}}}{2},\ \mathbf{K}_{\mathrm{i+1}} = \dfrac{\mathbf{K}_{\mathrm{i}} + \mathbf{K}_{\mathrm{n}}}{2}$
Rayleigh damping:	$\mathbf{C}_{\mathrm{i+1}} = \alpha \mathbf{M}_{\mathrm{i+1}} + \beta \mathbf{K}_{\mathrm{i+1}}$
External load increment:	$\Delta \mathbf{f} = \mathbf{f}_{\mathrm{i+1}} - \mathbf{f}_{\mathrm{n}}$
Iterative Newark implicit solution:	$\bar{\mathbf{K}}_{\mathrm{i+1}} \Delta \mathbf{u}_{\mathrm{i+1}} = \Delta \bar{\mathbf{F}} \rightarrow \mathbf{u}_{\mathrm{i+1}},\ \dot{\mathbf{u}}_{\mathrm{i+1}},\ \ddot{\mathbf{u}}_{\mathrm{i+1}},$
Nonlinear equilibrium:	$\mathbf{f}_{\mathrm{i+1}} = \mathbf{K}_{\mathrm{i+1}} \mathbf{u}_{\mathrm{i+1}}$
Norm of forces and displacements:	$\mathrm{R}_{\mathrm{force}} = \lVert \mathbf{f}_{\mathrm{i+1}} - \mathbf{f}_{\mathrm{i}} \rVert$ and $\mathrm{R}_{\mathrm{displ}} = \lVert \mathbf{u}_{\mathrm{i+1}} - \mathbf{u}_{\mathrm{i}} \rVert,$
Tolerance check:	$\mathrm{R}_{\mathrm{force}} < \mathrm{R}_{\mathrm{tol}},\quad \mathrm{R}_{\mathrm{disp}} < \mathrm{R}_{\mathrm{tol}}$

IF no equilibrium is found *THEN* reduce the time step *ELSE* go to the next

Figure 2-2: Nonlinear time integration scheme.

Slika 2-2: Shema nelinearne časovne integracije.

The average acceleration method with $\gamma = 1/2$ and $\beta = 1/4$ is used in the following simulations. A time step *Δt=0.2* s is chosen for all time-domain analyses. For an appropriate time step *Δt*, the following recommendations [2] can be used:

a) $\Delta t \leq 1/10\, T_{high}$, where T_{high} is the initial highest natural period.
b) More complex loads $\mathbf{f}_{\mathrm{ext}}$ require smaller time steps.
c) Geometrical and material nonlinearities require smaller time steps.

Equation (2.2) presents a complex set of coupled nonlinear equations of motion. Nonlinearities are sourced from geometrical nonlinearities, material nonlinearities, nonlinear loads and their interactions. The experience with extensive floating bridge dynamics gained during this research work is presented, showing the tuning of different parameters to improve the numerical scheme. The efficient and stable numerical scheme used in this thesis was achieved by:

a) setting the Newmark parameters to their default values ($\gamma = 1/2$ and $\beta = 1/4$);
b) applying stiffness-dependent damping β to flexible cable structures, rather than mass proportional damping α;
c) setting the convergence parameters for the Newton-Raphson algorithm (by adjustment of the relevant convergence values for the model, the nonlinear increments, the number of iteration steps, the final convergence steps, etc.);
d) avoiding the modeling of very stiff structural parts commonly attempted to reproduce some rigid behavior;
e) tuning the substepping for the nonlinear nonconverted time step.

During model setup, several numerical problems can occur. Here, the experience gained in modeling the structure is presented to avoid some common modeling mistakes. It is wise to avoid the modeling of very stiff elements with no mass, which results in an extremely high K/M ratio that cannot be resolved. This is related to the computer precision of the software code used for the analyses. Many loads are nonlinear and time-step dependent, thus requiring a sufficiently small time step to correctly resolve the hysteretic response. Some hydrodynamic and aeroelastic loads involve numerical convolution calculations. A representative response time length and a sufficiently small time step must be selected to obtain a proper calculation.

The discussion above shows that the time-integration parameters need to be determined to achieve proper dynamic modeling of floating bridges. This is a complex multiparameter search that requires some user experience. These guidelines might help readers in future investigations of floating bridges and in the initial setup of a numerical model.

3 HYDRODYNAMIC EFFECTS ON A FLOATING BRIDGE

3.1 Hydrodynamic effects on a floater

The submerged parts of a floating bridge interact with the surrounding sea. The movement of the bridge structure in the sea can be mathematically decomposed into two load types. The first type is the loads acting on a fixed rigid floater and is commonly modeled as static wave loads. The second type is self-excited floater movement in still water conditions and results in motion-dependent forces. Both effects can be linearly superimposed and are presented in Figure 3-1.

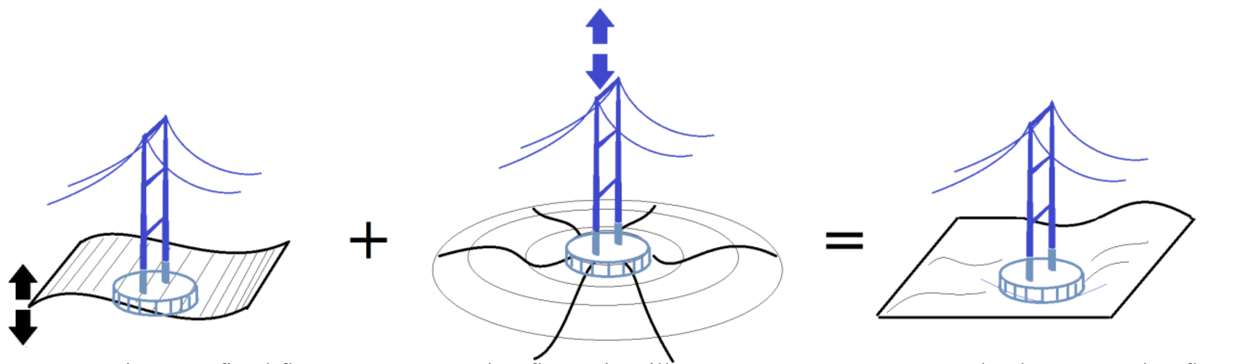

Figure 3-1: Wave load and wave radiation-damping superposition.

Slika 3-1: Obtežba valov in radiacija valov zaradi pomikov mostu v morju.

The hydrodynamic effects on floating towers can be summarized as follows:

a) wave loads on a nonmoving rigid object, which are modeled as time-dependent loads;
b) forces induced by tower movement in still water result in radiating waves, which are commonly described by linear frequency-dependent damping and inertia terms, hydrodynamic damping and frequency dependence on the hydrodynamic added mass;
c) other effects of inertia, viscous effects, nonlinear effects, etc.

The submerged hull of a floating tower is modeled as a rigid body in hydrodynamic analysis, neglecting the hydroelastic effects. All hydrodynamic loads are a resultant force of the integrated pressures of the wet surfaces. The motion-dependent hydrodynamic forces in b) are measured under still water conditions, where the nonmoving structure is exposed to the wave loads described in a). By summing a) and b) together, one can describe a moving structure in the wave sea environment. Floating bridge systems are commonly vertically restrained by a tether anchorage system, which considerably reduces the vertical deformations; therefore, first-order wave load models can provide sufficient accuracy for practical applications. Hydrodynamic loads contribute substantially to the floating bridge dynamics, altering the structural properties.

Several additional hydrodynamic effects are commonly found in the literature [9]. The underwater currents can be modeled as movements relative to the structure, expressed by nonlinear viscous drag damping (VDD) (chapter 3.8). Hydrodynamic inertia forces are present due to displaced water structures, commonly modeled with linear diagonal stiffness terms (chapter 3.7). The hydrodynamic effects of the floater are expressed as one "hydrodynamic node" describing all hydrodynamic loads. The hydrodynamic node is then assigned to a finite element mesh node on the bridge, commonly modeled at sea level. Hydrodynamic forces have six components, i.e., three forces and three moments. These are described in right-hand Cartesian coordinates as surge, sway and heave, as presented in Figure 3-2. This thesis bridge model uses a left-hand Cartesian coordinate system, i.e., x, y and z, which is described as follows.

$$\begin{array}{ccc} \textbf{Hydrodynamic} & \text{and} & \textbf{Bridge} \text{ coordinate system} \\ \begin{bmatrix} \text{Surge x} \\ \text{Sway y} \\ \text{Heave z} \\ \text{Roll rx} \\ \text{Pitch ry} \\ \text{Yaw rz} \end{bmatrix} & = & \begin{bmatrix} x \\ z \\ y \\ rx \\ rz \\ ry \end{bmatrix} \end{array} \tag{3.1}$$

The suspension floating bridge concept is supported by a floating TLP foundation, offering support for the bridge floating superstructure. The agreed-upon naming system provides vocabulary that is used across different engineering disciplines, as shown in Figure 3-2.

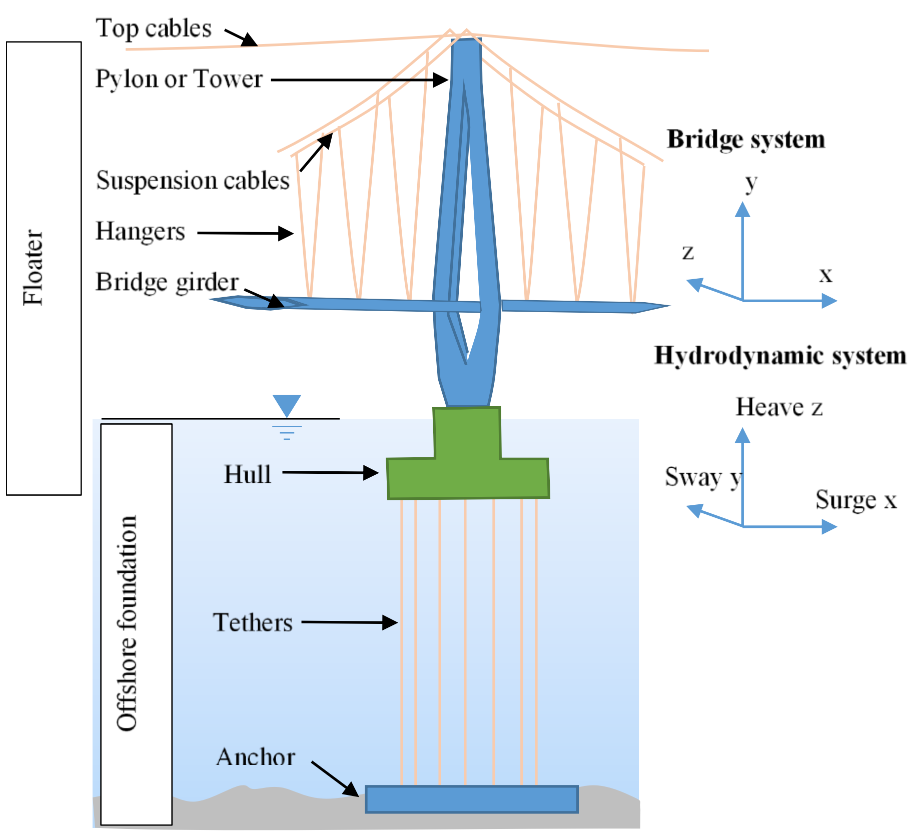

Figure 3-2: Parts of the floating bridge according to the hydrodynamic naming convention [29].

Slika 3-2: Sestavni deli plavajočega mostu [29].

3.2 Description of waves

Loading due to sea surface waves is simulated as periodic loading of the moving water fluid around the submerged structure. Different wave generation mechanisms exist, such as wind, earthquakes, the motion of objects in water, and astronomical tides. No universal model that covers all wave motion scenarios exists. Different assumptions can be introduced to model the waves. In general, wave loads can be divided into sea wave loads and swell wave loads [30].

a) **Sea waves** are a series of waves driven by local wind. The waves are short-crested, extending 2-3 wave heights perpendicular to the direction of propagation. They are irregular and are modeled as a summation of different random wave frequencies. The wave crests look sharp under random wave motion. The wave properties are described for continuously varying wave periods *T*.
b) **Swell loads** propagate without locally generated wind. They can spread hundreds of kilometers across the sea under calm winds. They have longer crest wavelengths, and their wave height is more predictable. They can pass an object with a sequence of waves.

Waves are free-surface fluctuations of the surrounding sea. The underwater particle movement can be mathematically described by wave potential theory. Complicated wave systems are a superposition of different trigonometric waves. Each wave is described by a one-dimensional free-surface elevation, resulting in horizontal and vertical underwater particle movement. Linear potential theory is then used to describe the velocity field of underwater particle movement. The displaced water movement results in changes in the surrounding pressure and hydrodynamic forces.

Wave forces are mathematically modeled as a product of the transfer function and wave movement. The transfer function consists of the amplitude and phase lag of three-transversal and three-moment forces. In general, the resulting forces depend on the shape of the submerged object and its pressure distribution. In fjords, deep-water waves, also known as short waves, are commonly present. The highest point (wave crest) and lowest point (wave trough) on a wave pass the zero-elevation surface. The vertical separation is the so-called wave height, calculated as $H = 2\xi_{\mathrm{a}}$. Free-surface motion can be mathematically described by a superposition of cosine functions, commonly called first-order waves. The horizontal separation distance between two wave crests is the wavelength λ. The ratio between the wave height H and wavelength λ is the wave steepness H/λ. This results in a commonly applied cosine wave function of free-surface displacement ξ, which is defined as:

$$\xi = \xi_{\mathrm{a}} \cos\left(kx - \omega t\right) \tag{3.2}$$

where $k = 2\pi / \lambda$ is the wavenumber, $\omega = 2\pi / T$ is the circular wave frequency and ξ_{a} is the amplitude.

These simple relations can be presented with one degree of freedom (DOF) of free-surface motion, as depicted in Figure 3-3.

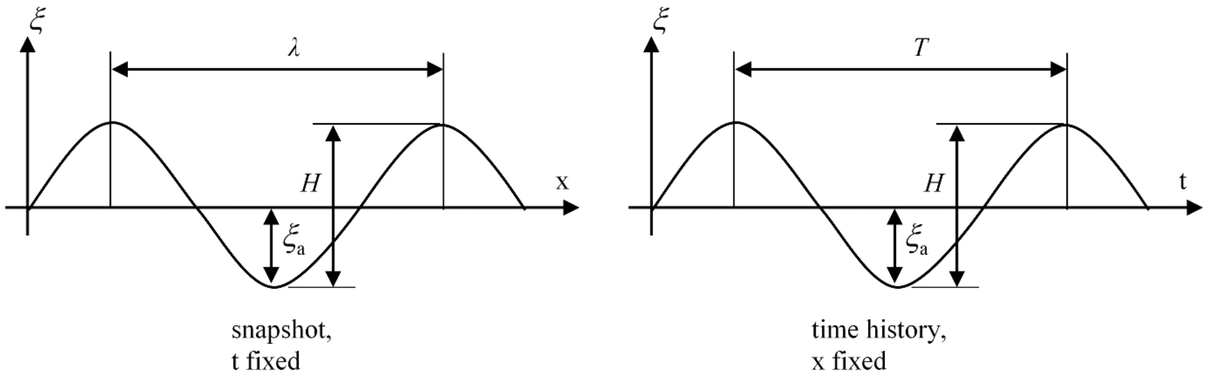

Figure 3-3: Harmonic wave definition

Slika 3-3: Prikaz formulacije harmoničnih valov.

The linear wave theory assumption is used, which assumes a small steepness of waves *H/λ,* also known as first-order waves of small amplitude, thus allowing for the linear harmonic superposition of displacements, velocities and accelerations.

3.3 Wave spectrum generation

A linear superposition of different cosine wave functions holds. Here, some well-known wave relations are presented for stationary random processes. The measured wind-sea wave spectrum has a significant wave height defined by $H_s \equiv 4\sigma$ with a peak period $T_p \equiv 2\pi/\omega_p$. This property defines the one-directional wave spectrum $S_\xi(\omega)$ and can be extended to a mathematical model that includes the directional distribution of incoming waves [31]. The spectral density fluctuation considering multiple directions is:

$$S_{\xi,\theta}(\omega,\theta) = S_\xi(\omega) D(\theta) \tag{3.3}$$

where $S_{\xi,\theta}$ is the directional spectrum, S_ξ is the one-dimensional spectral density, and D is the directional distribution function. The JONSWAP spectrum is commonly applied for wind-sea wave simulations of deep-water fjords [32] [33]. The spectrum shape can be suited for onsite-measured waves at the bridge location. The general spectrum expression is defined as:

$$S_\xi(\omega) = Ag^2\omega^{-5} \exp\left[-\frac{5}{4}\left(\frac{\omega_p}{\omega}\right)^4\right] \tag{3.4}$$

where ω_p is the peak frequency and A is the energy scaling parameter. Waves are spread around the main incoming wave direction by correcting the one-dimensional wave spectrum. For the directional distribution, the non-frequency-dependent formula can be defined as:

$$D(\theta)=\frac{\Gamma(s+1)}{2\sqrt{\pi}\Gamma(s+1/2)}\cos^{2s}\left(\frac{\theta}{2}\right) \tag{3.5}$$

where s is a directional parameter and Γ is a gamma function. The circular integral of the directional parameter $D(\theta)$ yields an area equal to one; thus the energy content of the one-dimensional wave spectrum is not changed. The gamma function is defined by the infinite integral:

$$\Gamma(s)=\int_0^\infty t^{s-1}e^{-t}dt \tag{3.6}$$

With these parameters, free-surface waves can be simulated for a chosen direction. An example of a synthetically generated power spectrum and a directional distribution for a directional angle of 0 is presented in Figure 3-4.

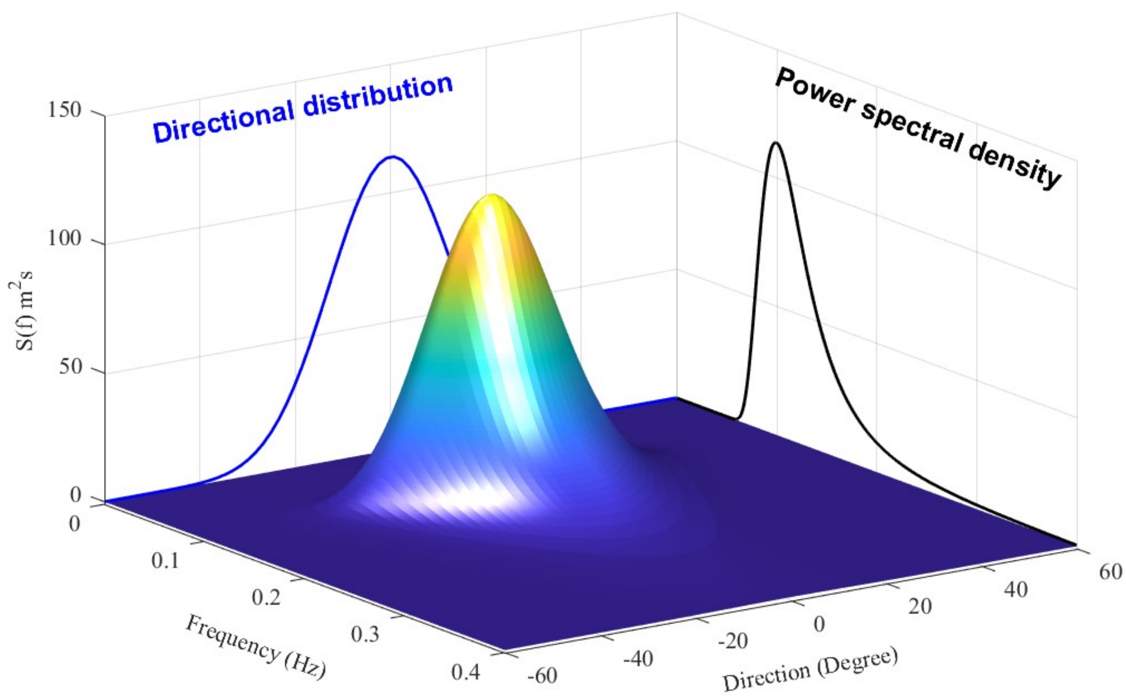

Figure 3-4: Wave power spectrum and directional distribution [34]

Slika 3-4: Spekter valov in porazdelitvena funkcija smeri valovanja [34].

3.4 Hydrodynamic potential theory

The hydrodynamic potential theory analytically describes the free-surface wave potential. It is a well-accepted hydrodynamic offshore theory and can be applied to the hydrodynamic models of floating bridges. An overview and the potential theory principles are presented in the following; interested readers can review the literature for a more detailed explanation [30] [5]. For an analytically defined velocity field, a numerical evaluation of the hydrodynamic forces on a submerged object is possible. This evaluation is accomplished by numerical discretization of the submerged object and application of the appropriate boundary conditions. In hydrodynamic analysis, this is a well-known 3D panel numerical method. The water potential is defined by the following boundaries a) to f):

a) **Continuity condition**, described by the Laplace equation of inviscid, incompressible and irrotational flow, without any surface tension effect.

$$\nabla^2 \phi = \frac{\partial^2 \phi}{\partial x^2} + \frac{\partial^2 \phi}{\partial y^2} + \frac{\partial^2 \phi}{\partial z^2} = 0 \tag{3.7}$$

b) **Seabed condition** for a relation valid for deep-water waves.

$$\frac{\partial \phi}{\partial z} = 0 \qquad \text{for: } z = -h \tag{3.8}$$

c) **Free-surface kinematic boundary surface condition**, describing the wave periodic surface oscillations.

$$\frac{\partial^2 \phi}{\partial t^2} + g \frac{\partial \phi}{\partial z} = 0 \qquad \text{for: } z = 0 \tag{3.9}$$

d) **Kinematic boundary condition on the oscillating body surface**, which assumes rigid body movement. The velocity values for the body and water at surface S are equal. The normal surface component n of the surface velocity v of the hull geometry f is:

$$\frac{\partial \phi}{\partial n} = \vec{v} \cdot \vec{n} = \sum_{j=1}^{6} v_j \cdot f_j \left(x, y, z \right) \tag{3.10}$$

e) **Radiation condition**, which states that for large distances, regarding middle-sea hull objects, the potential converges to zero and can be defined as:

$$\lim_{R \to \infty} \phi = 0 \tag{3.11}$$

f) **Symmetric or antisymmetric conditions** can simplify the numerical calculation efforts.

The wind-generated waves are approximated by a local homogeneous random field. Potential theory assumes a linear relation between the surface wave motion ξ and pressure distribution. The velocity potential equation requires a numerical solution for calculating three-dimensional submerged objects. For most floating bridge crossings, the deep-water wave modeling assumption is adequate. An analytical solution of the wave potential ϕ describing circulating vertical w and horizontal u velocities exists, as follows:

$$\begin{aligned} u &= \xi_a \omega e^{kz} \cos(kx - \omega t) \\ w &= \xi_a \omega e^{kz} \sin(kx - \omega t) \end{aligned} \tag{3.12}$$

The one-dimensional kinematics of deep-water waves resulting in subsea water movement in the vertical and horizontal directions are depicted in Figure 3-5.

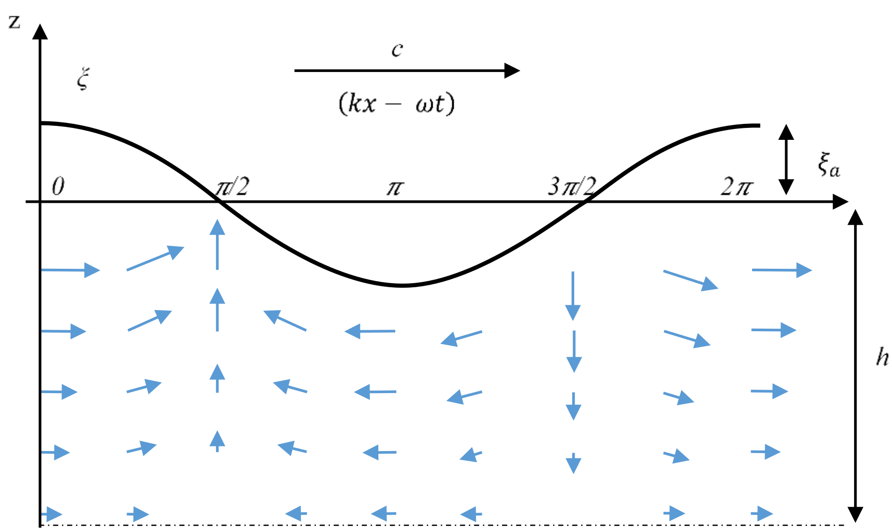

Figure 3-5: Velocity field in the deep-water model.

Slika 3-5: Potencial hitrosti valov pri večjih globinah.

The presented theoretical assumptions can be solved by a numerical 3D panel method, which is suitable for calculating complex hull geometry shapes. The three-dimensional potential is defined and numerically resolved, yielding radiation diffraction forces. The theory calculates the wave-frequency hydrodynamic loads of free-flowing objects. No leak condition is assumed for the submerged object or the seabed. The results for a steel hull object are presented in Figure 3-6.

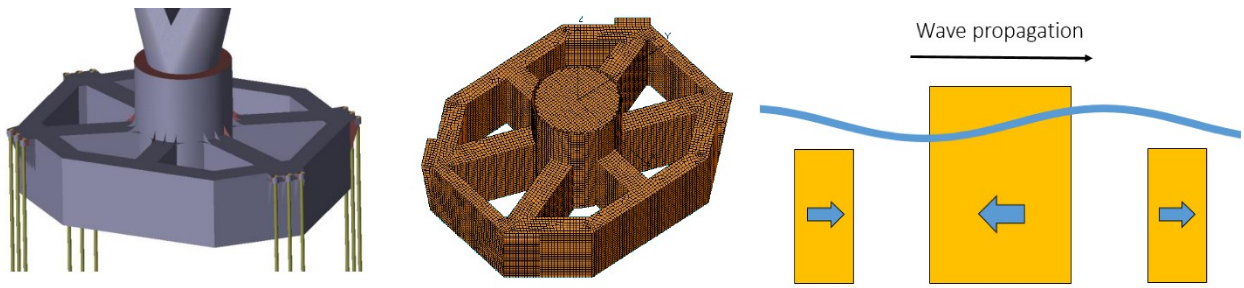

Figure 3-6: Steel hull (left), numerical model (middle), and excitation forces of wave propagation (right) [35].

Slika 3-6: Ponton iz jekla levo, numerična panelna metoda v sredini, sile valov na ponton desno [35].

In the 3D panel method, the potential flow around the hull is calculated numerically. According to Green's integral theorem, the three-dimensional linear homogeneous differential equation in Eq. (3.7) can be transformed into a two-dimensional integral equation. In this way, the three-dimensional Laplace (potential) equation is transformed into a surface integral equation with Green's identity theorem. The integral equation represents a distribution of sources (or sinks) and dipoles on the surface. The surface of the body is divided into a number of discrete panels, as shown in the middle of Figure 3-6. The water pressure during the wave potential is then integrated across panels and results in wave transfer functions. The advantage of this method is the two-dimensional surface calculation of any three-dimensional structure. It is suitable to investigate objects of any shape and size. The transfer function is then evaluated separately for each frequency, resulting in a transfer function of complex form. These functions are used for wave load generation or for potential radiation damping. The numerical approach provides results that agree well with the water tank measurement results and is a common tool used in hydrodynamic praxis. In addition, laboratory tests can be carried out for obtaining wave records and linear radiation-damping tests, as shown in Figure 3-7.

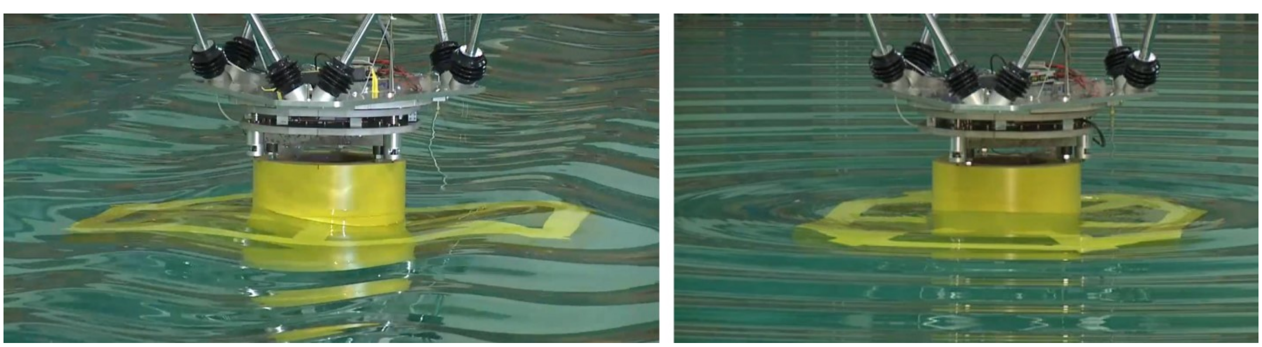

Figure 3-7: Laboratory tests at SINTEF Trondheim: wave excitation (left) and wave radiation damping (right) [35].
Slika 3-7: Laboratorij SINTEF v Trondheimu, obtežba valov (levo), dušenje pomikov gibanja (desno) [35].

3.5 Wave load time series

The wave load presents the integrated water pressure around the floater hull due to incoming waves. The water surface elevation can be presented as a collection of single wave frequencies and is represented by the power spectrum density (PSD), denoted as S_ξ. Conversation between the frequency and time domains is carried out via a pair of Fourier transforms that contain both real and imaginary components. This mathematical operation transforms the time-dependent measured wave time signal into a frequency-dependent wave PSD. These are commonly presented as spectrum amplitude and phase shifts. An IFT can then be applied to simulate the time-dependent wave records, which can be utilized in bridge response investigations. This conversion between measurements and wave signal generation is presented in Figure 3-10.

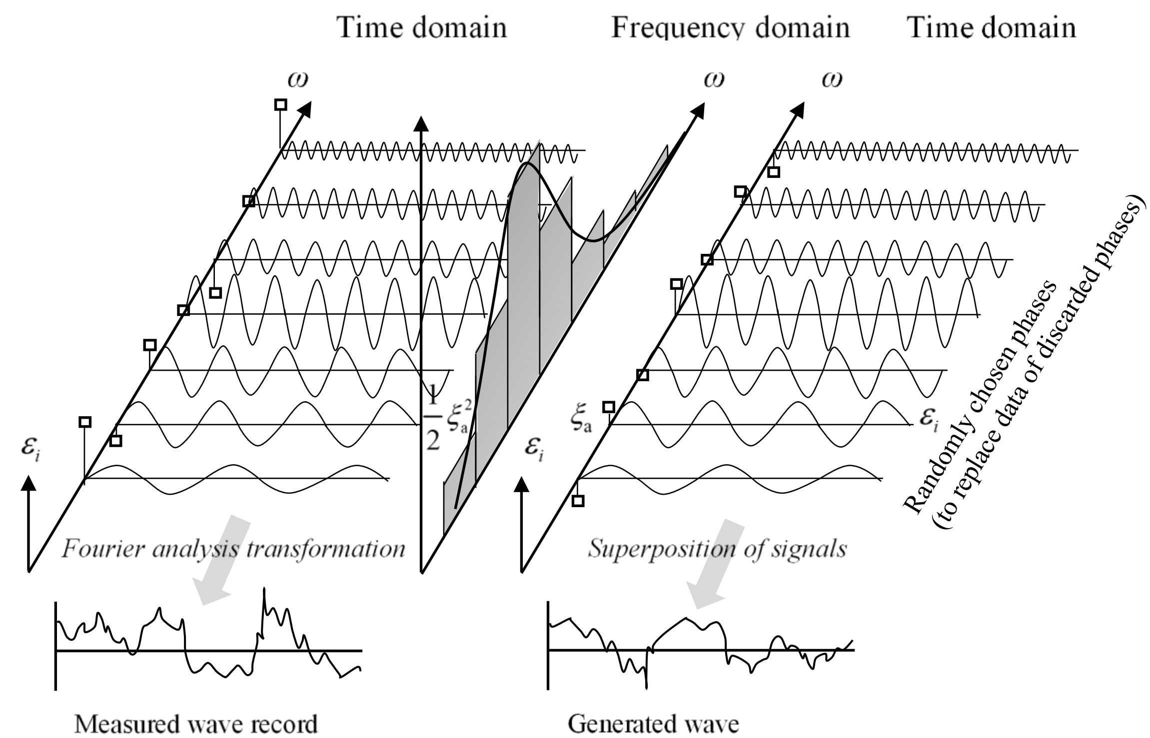

Figure 3-8: Wave record analysis and generation.

Slika 3-8: Meritve valov desno in sintetiziranje valov levo.

The phase shift information is typically neglected because no requirement exists for directly reproducing each individually measured wave signal. Instead, artificially generated waves can be representative of multiple scenarios containing similar wave response energies. The discarded measured imaginary phase information is replaced by the uniform random phases of white noise spectra, which requires the generation of multiple time series to obtain the equivalent average spectrum energy. This process presents a notable computational effort and is challenging for any time-domain application. The variance in the generated signals must be maintained for an average of all Fourier transformations. The root mean square (RMS) of several generated time series builds a median time-domain response. The median of the generated signals should be on average equal to the variance in the input frequency power spectrum variance. The power spectrum variance is calculated as the area below the input frequency power spectrum. The square of the following relation must be maintained between all time and frequency transformations:

$$\text{median}\left[\sqrt{\left\langle \xi^2(t) \right\rangle}\right] \equiv \sqrt{\int_0^\infty S_\xi(\omega)\,d\omega} \tag{3.13}$$

The same principle is also applicable to the wind time series, as presented in Figure 4-7. Fourier transformation of the generated wave time signal also involves the directional distribution. Homogeneous waves follow a linear stationary Gaussian model [25]. The rigid body behavior of the hull object is assumed, and no hydroelasticity effects are present. The wave forces F_{wave} are presented with a six-component vector n, which includes three forces and three moments. The forces are modeled by a transfer function F_n obtained using the first-order calculation of the potential theory presented in chapter 3.4. The time-domain wave force component is calculated as:

$$\begin{aligned} F_{\text{wave,n}}(x,y,t) = \sum_i^N \sum_j^M \left| F_{\text{n}}(\omega_i,\theta_j) \right| \sqrt{2S_{\xi,\theta}(\omega,\theta)\,\Delta\omega\Delta\theta} \\ \cos\left[\mathrm{k}_i x \cos(\theta_j) + \mathrm{k}_i y \sin(\theta_l) - \omega_i t + \varepsilon_{ij} - \phi_{ij} \right], \end{aligned} \tag{3.14}$$

$$\text{where} \quad \phi_{ij} = \tan^{-1}\left(\frac{\mathrm{Im}\left(F_{\text{n}}(\omega_i,\theta_j)\right)}{\mathrm{Re}\left(F_{\text{n}}(\omega_i,\theta_j)\right)} \right), \qquad \mathrm{k}_i = \frac{\omega_i^2}{g}$$

Here, $F_{\text{wave,n}}, n \in \{1\ldots6\}$ denotes the fixed force components, F_n is a complex hydrodynamic transfer function, and $\varepsilon_{ij}, n \in \{0\ldots2\pi\}$ is a random uniform distributed phase angle. The amplitudes describe the absolute values of the transfer function $|F_n(\omega)|$ and the corresponding phase angles. The frequency-dependent values represent a range of measured frequencies, where the wind-sea modeling is in the range of $[4s\ldots10s]$. The transfer functions can be calculated with the numerical hydrodynamic software AQWA, the results of which are validated through laboratory tests. COWI Norway [36] provided some numerical results, and SINTEF Trondheim made the laboratory measurements [37]. An example of the amplitudes of the wave transfer function for a steel hull is presented in Figure 3-9.

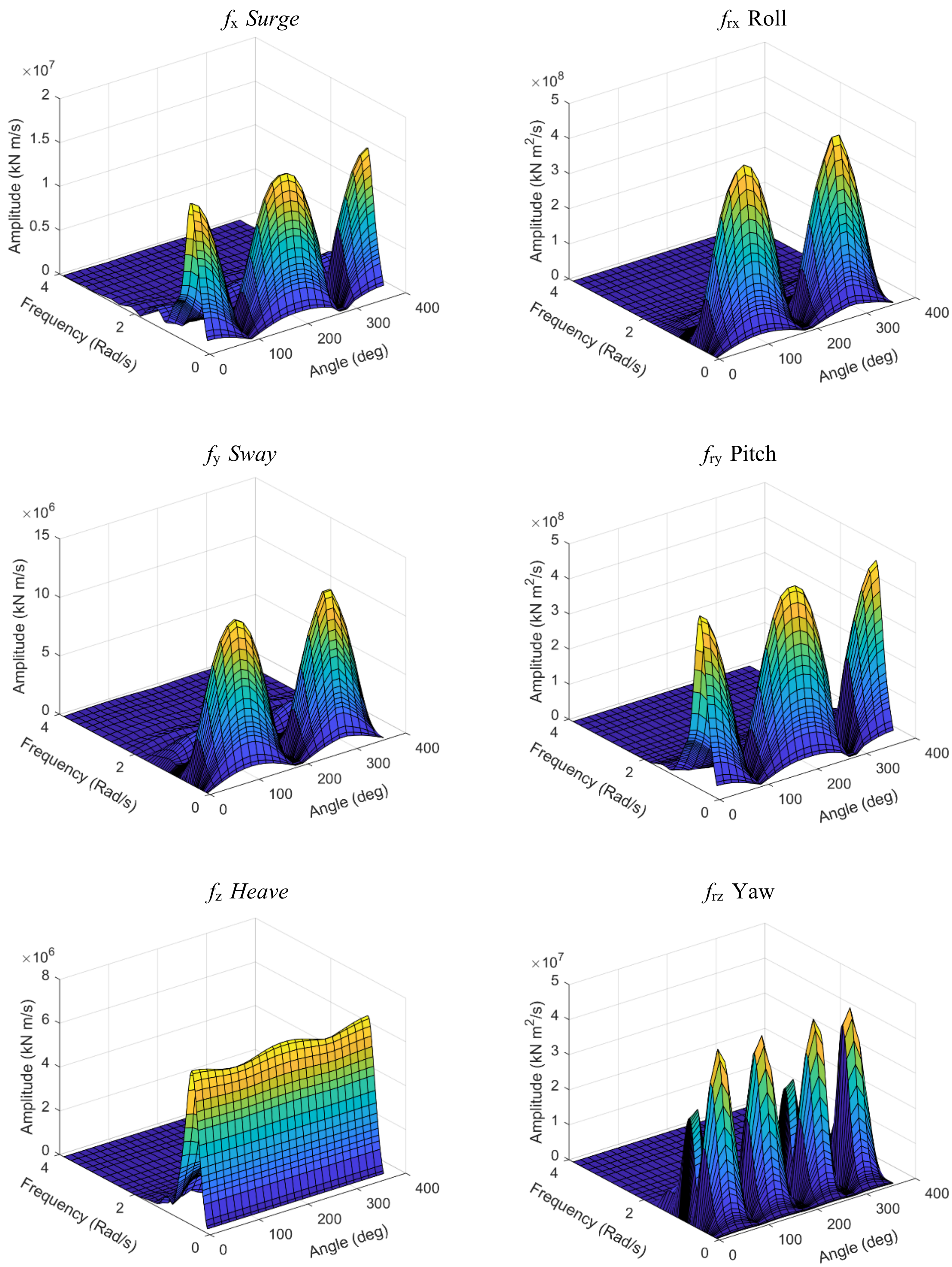

Figure 3-9: Hull wave amplitudes; the left column shows translations, and the right column shows rotations [38].

Slika 3-9: Amplitude pomikov valov, levi stolpec za pomike in desni stolpec rotacije jeklenega pontona [38].

3.6 Hydrodynamic wave radiation formulation

In this chapter, the motion-induced wave radiation loads are modeled with frequency-dependent hydrodynamic damping and added mass. These are isolated forces without wave action, according to Figure 3-1. Motion-dependent forces are measured at multiple discrete motion oscillation frequencies, resulting in a frequency-dependent force formulation. The formulation assumes a continuous linear superimposition at different frequencies. The linear hydrodynamic wave radiation forces are expressed on the left side of the structural dynamic equation as:

$$\left(\mathbf{M}+\mathbf{M}_{\mathrm{hy}}(\omega)\right)\ddot{\mathbf{u}}+\left(\mathbf{C}+\mathbf{C}_{\mathrm{hy}}(\omega)\right)\dot{\mathbf{u}}+\mathbf{K}\mathbf{u}=0 \tag{3.15}$$

The hydrodynamic self-excited forces are mainly acceleration-velocity dependent. The hydrodynamic force vector consists of frequency-dependent damping $\mathbf{C}_{\mathrm{hy}}(\omega)$ and a hydrodynamic mass $\mathbf{M}_{\mathrm{hy}}(\omega)$ contribution. Thus, the frequency-domain motion-induced hydrodynamic forces can be expressed as:

$$\mathbf{G}_{\mathrm{hy}}(\omega)=\mathbf{H}_{\mathrm{hy}}(\omega)\mathbf{G}_{\mathrm{v}}(\omega) \tag{3.16}$$

where $\mathbf{G}_{\mathrm{hy}}$ is a Fourier transform vector of hydrodynamic motion-induced forces, $\mathbf{H}_{\mathrm{hy}}$ is a transfer function matrix suitable for velocity transformation, and $\mathbf{G}_{\mathrm{v}}$ is a Fourier transform vector of structural velocities. Here, the hydrodynamic transfer function is defined as:

$$\mathbf{H}_{\mathrm{hy}}(\omega)=i\omega\mathbf{M}_{\mathrm{hy}}(\omega)+\mathbf{C}_{\mathrm{hy}}(\omega) \tag{3.17}$$

Eq. (3.15) cannot be resolved within the Newark time-integration method and requires convolution integration. The frequency-dependent properties are transferred to the time domain with the numerical IFT, resulting in the $\mathbf{J}_{\mathrm{hy}}(t)$ impulse response function or retardation function:

$$\mathbf{J}_{\mathrm{hy}}(t)=\frac{1}{2\pi}\int_{\infty}^{\infty}\mathbf{H}_{\mathrm{hy}}(\omega)e^{i\omega t}d\omega \tag{3.18}$$

With the convolution integral over the history of structural velocities, the hydrodynamic wave radiation forces are calculated as:

$$\mathbf{q}_{\mathrm{hy}}(t)=\mathbf{M}_{\mathrm{hy}}(\infty)\ddot{\mathbf{u}}(t)+\int_{-\infty}^{\infty}\mathbf{J}_{\mathrm{hy}}(t-\tau)\ \dot{\mathbf{u}}(\tau)d\tau \tag{3.19}$$

This convolution integral involves integrating all the way back to the start of the simulation at each time step, causing increasingly slower simulation time progress. The exact derivation is presented in an example with a single DOF to illustrate some theoretical principles.

The hydrodynamic radiation force can be split into infinite and frequency-dependent contributions:

$$\begin{aligned} M_{\mathrm{hy}}(\omega) &= \left[M_{\mathrm{hy}}(\omega) - M_{\mathrm{hy}}(\infty)\right] + M_{\mathrm{hy}}(\infty) \\ C_{\mathrm{hy}}(\omega) &= \left[C_{\mathrm{hy}}(\omega) - C_{\mathrm{hy}}(\infty)\right] + C_{\mathrm{hy}}(\infty) \end{aligned} \tag{3.20}$$

The frequency-dependent conversion into the time domain follows the IFT (3.18) and convolution over velocities (3.19) [5]. In hydrodynamic applications, the well-known Cummins transformation is used to calculate the hydrodynamic motion-induced forces [39] [40]. The wave radiation forces are extrapolated to fulfill a relation $C_{\mathrm{hy}}(\infty) = 0$. The frequency contribution of the hydrodynamic transfer function in (3.17) is defined as:

$$H_{\mathrm{hy}}(\omega) = i\omega\left[M_{\mathrm{hy}}(\omega) - M_{\mathrm{hy}}(\infty)\right] + i\omega M_{\mathrm{hy}}(\infty) + C_{\mathrm{hy}}(\omega) \tag{3.21}$$

where the IFT (3.18) can be written as:

$$\begin{aligned} J_{\mathrm{hy}}(t) = J_{\mathrm{hy}}^{\infty} + J_{\mathrm{hy}}^{\omega} &= \frac{1}{2\pi}\int_{-\infty}^{\infty} i\omega M_{\mathrm{hy}}(\infty)\, e^{i\omega t} d\omega \\ &+ \frac{1}{2\pi}\int_{-\infty}^{\infty}\left(i\omega\left[M_{\mathrm{hy}}(\omega) - M_{\mathrm{hy}}(\infty)\right] + C_{\mathrm{hy}}(\omega)\right) e^{i\omega t} d\omega \end{aligned} \tag{3.22}$$

The above equation consists of an infinite contribution J_{hy}^{∞} and a frequency-dependent contribution J_{hy}^{ω} impulse response function. The infinite contribution of infinite mass has an analytical solution as a derivative of a step function:

$$J_{\mathrm{hy}}^{\infty} = M_{\mathrm{hy}}(\infty)\dot{\delta}(t) \tag{3.23}$$

The frequency-dependent solution is found by a numerical Fourier transformation. Since the forces can be described by a continuous function, the complex exponential Fourier transformation $e^{i\omega t} = cos(\omega t) + i \cdot \sin(\omega t)$ is written in trigonometric form as:

$$J_{\mathrm{hy}}^{\omega}(t) = \frac{1}{2\pi}\int_{-\infty}^{\infty}\left(i\omega\left[M_{\mathrm{hy}}(\omega) - M_{\mathrm{hy}}(\infty)\right] + C_{\mathrm{hy}}(\omega)\right)\left(\cos(\omega t) + i\cdot\sin(\omega t)\right) d\omega \tag{3.24}$$

The double-sided spectrum can be written as a sum of two single-sided spectra, consisting of integrals from the negative and positive frequency axes:

$$\begin{aligned} J_{\mathrm{hy}}^{\omega}(t) = &\frac{1}{2\pi}\int_{-\infty}^{0}\left(i\omega\left[M_{\mathrm{hy}}(\omega) - M_{\mathrm{hy}}(\infty)\right] + C_{\mathrm{hy}}(\omega)\right)\left(\cos(\omega t) + i\cdot\sin(\omega t)\right) d\omega + \\ &\frac{1}{2\pi}\int_{0}^{\infty}\left(i\omega\left[M_{\mathrm{hy}}(\omega) - M_{\mathrm{hy}}(\infty)\right] + C_{\mathrm{hy}}(\omega)\right)\left(\cos(\omega t) + i\cdot\sin(\omega t)\right) d\omega \end{aligned} \tag{3.25}$$

Applying asymmetry and symmetry valid for the causal invariant dynamic system changes the integration limits and results in a single-sided spectrum:

$$J_{\mathrm{hy}}^{\omega}(t)=\frac{1}{2\pi}\int_{0}^{\infty}\left(-i\omega\left[M_{\mathrm{hy}}(\omega)-M_{\mathrm{hy}}(\infty)\right]+C_{\mathrm{hy}}(\omega)\right)\left(\cos(\omega t)-i\cdot\sin(\omega t)\right)d\omega+ \frac{1}{2\pi}\int_{0}^{\infty}\left(i\omega\left[M_{\mathrm{hy}}(\omega)-M_{\mathrm{hy}}(\infty)\right]+C_{\mathrm{hy}}(\omega)\right)\left(\cos(\omega t)+i\cdot\sin(\omega t)\right)d\omega \tag{3.26}$$

This expression simplifies to:

$$J_{\mathrm{hy}}^{\omega}(t)=-\frac{1}{\pi}\int_{0}^{\infty}\omega\left[M_{\mathrm{hy}}(\omega)-M_{\mathrm{hy}}(\infty)\right]\sin(\omega t)d\omega+\frac{1}{\pi}\int_{0}^{\infty}C_{\mathrm{hy}}(\omega)\cos(\omega t)d\omega \tag{3.27}$$

Introducing additional assumptions for all negative times, the response $I_{\omega}(-t)=0$. Since no motion information is present before t=0, this result is valid for nonvibrating structures. This will be reflected in the change in the integral limit, yielding the following relation:

$$C_{\mathrm{hy}}(\omega)\cos(\omega t)d\omega=-\omega\left[M_{\mathrm{hy}}(\omega)-M_{\mathrm{hy}}(\infty)\right]\sin(\omega t)d\omega \tag{3.28}$$

An important relation between frequency-dependent added mass and frequency-dependent radiation damping is derived that is valid for causal dynamic systems. Substituting the relation (3.28) into equation (3.27) yields:

$$J_{\mathrm{hy}}^{\omega}(t)=\frac{2}{\pi}\int_{0}^{\infty}C_{\mathrm{hy}}(\omega)\cos(\omega t)d\omega \tag{3.29}$$

The total impulse response function is convoluted over the velocity history of motion (3.19), yielding:

$$q_{\mathrm{hy}}(t)=\int_{0}^{t}M_{\mathrm{hy}}(\infty)\ \dot{\delta}(t-\tau)\ \dot{u}(t)d\tau+\frac{2}{\pi}\int_{0}^{t}\int_{0}^{\infty}C_{\mathrm{hy}}(\omega)\cos\left(\omega(t-\tau)\right)\dot{u}(t)d\omega d\tau \tag{3.30}$$

The analytical solution of an infinitely contributing hydrodynamic mass is:

$$q_{\mathrm{hy}}(t)=M_{\mathrm{hy}}(\infty)\ddot{u}(t)+\frac{2}{\pi}\int_{0}^{t}\int_{0}^{\infty}C_{\mathrm{hy}}(\omega)\cos\left(\omega(t-\tau)\right)\dot{u}(t)d\omega d\tau \tag{3.31}$$

Typical input data for frequency-dependent hydrodynamic wave radiation of added mass and damping are presented for the steel hull (Figure 3-6) in Figure 3-10. These principles are applied to a multi-DOF coupled dynamic system, yielding the linear wave radiation formulation in matrix format presented in (3.19).

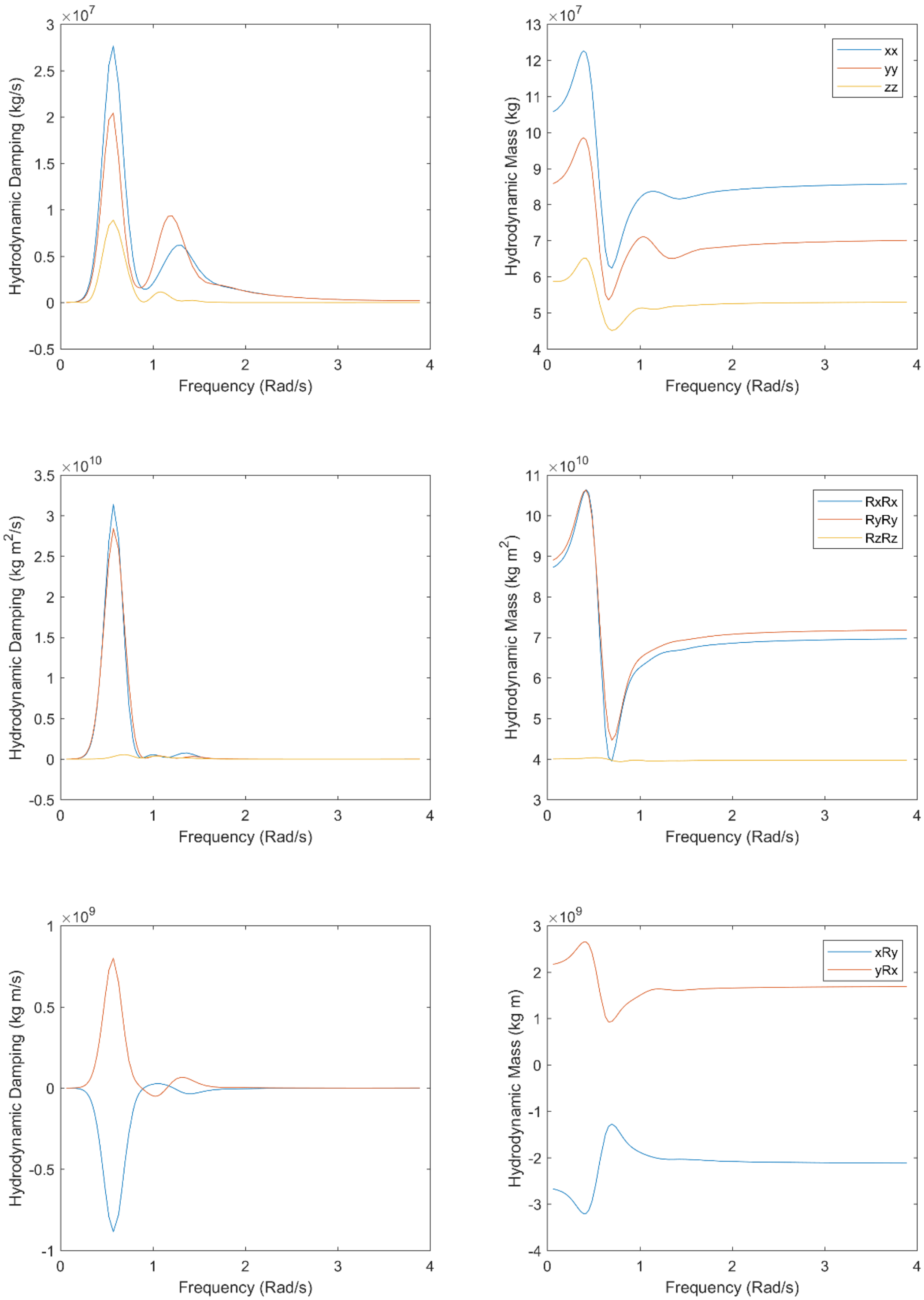

Figure 3-10: Frequency-dependent damping C(ω) and hydrodynamic mass M(ω) of a steel hull [29].
Slika 3-10: Rezultati jeklenega pontona za rekvenčno odvisno hidrodinamično dušenje C(ω) in maso M(ω) [29].

3.7 Hydrostatic restoring forces

The submerged hull has to provide buoyancy to the bridge superstructure. The hydrostatic force is constant over time and represents the floater buoyancy. According to Archimedes' principle, hydrostatic forces are equal to the floater volume of replaced water. This permanent vertical force gives the required uplift to balance the total permanent and dynamic bridge loads. The design requirement is that the buoyancy uplift force is always higher than the maximum possible combination of negative vertical loads on the floater. The excess vertical uplift forces are taken by the tether system and are therefore always subject to tension. This setup ensures a position in the sea with minimal vertical displacements and larger lateral deformations. This system works as a reverse pendulum, with the tethers designed to have tension at all times, as presented in Figure 3-11.

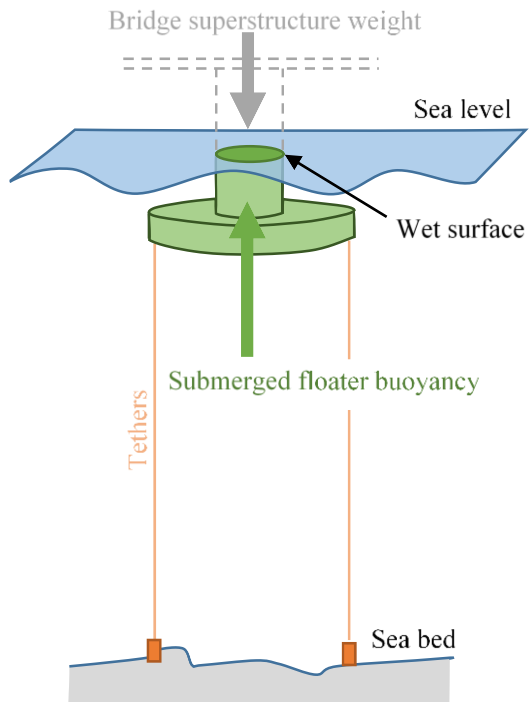

Figure 3-11: TLP suspension bridge concept.
Slika 3-11: Zasnova TLP visečega mostu.

The buoyancy force of the submerged object is calculated as:

$$\mathbf{F}_{\mathrm{buy}} = \rho g \mathbf{V}_{\mathrm{hull}} \tag{3.32}$$

where $\mathbf{F}_{\mathrm{buy}}$ is the vertical force component, g is the gravitational acceleration, $\mathbf{V}_{\mathrm{hull}}$ is the volume of the submerged floater, and ρ is the water density. For the dynamic variation in the loads, a linear change in forces is expressed by a linear spring coefficient related to a vertical stiffness $\mathbf{K}_{\mathrm{hy}}$, which is calculated as:

$$\begin{aligned} k_{\mathrm{hy,y}} &= \rho g A_{\mathrm{y,wp}} \\ k_{\mathrm{hy,rx}} &= \rho g I_{\mathrm{zz,wp}} \\ k_{\mathrm{hy,rz}} &= \rho g I_{\mathrm{xx,wp}} \end{aligned} \tag{3.33}$$

where $A_{\mathrm{y,wp}}$ is a wet surface defined by the intersection of the hull with the seaplane and $I_{\mathrm{zz,wp}}$, $I_{\mathrm{yy,wp}}$ are the moments of inertia of the wet surface cross-section. A linear set of the vertical spring system describes the constant variation in the wet surface interface cross-section. For the given final steel hull design geometry presented in Figure 3-7, the hydrostatic restoring forces are $k_{\mathrm{hy,y}} = 7\ \mathrm{MN}$, $k_{\mathrm{hy,rx}} = k_{\mathrm{hz,rx}} = 2200\ \mathrm{GN}$. The platform produces $F_{\mathrm{buy}} = 900\ \mathrm{MN}$ of the vertical uplift force to support the floating bridge [36].

3.8 Current load

The hydrodynamic drag force results from the inflow of underwater sea currents. The currents are represented by the velocity vectors of the sea and are nonlinearly distributed in the vertical direction. They are simulated as time constant loads, where the dynamic damping effect is present due to structural movement. These loads are commonly classified in the literature as viscous-drag damping (VDD) loads [41] [30]. The current load is the relative velocity between structural movement and the current velocity, as depicted in Figure 3-12. Its global bridge effects can be described by the static load contribution and low-frequency dynamic damping participation. All submerged elements, such as the hull and tethers, are subject to underwater current flows. The relative velocity V_{rel} between the structure and the current velocities is calculated as:

$$V_{\mathrm{rel}} = V_{\mathrm{stream}} - V_{\mathrm{elem}} f_{\mathrm{int}} \tag{3.34}$$

The interaction factor f_{int} is an empirical value that takes into account possible modified interactions caused by different oscillation frequencies and changes in surface roughness due to algae collected on the tethers. The VDD element distributed load is expressed as:

$$F_{\mathrm{cur}} = \frac{1}{2} \rho C_d D V_{\mathrm{rel}}^{\exp} \tag{3.35}$$

where ρ is the water density, C_d is the drag coefficient, D is the diameter and $exp = 2$ is the velocity exponent.

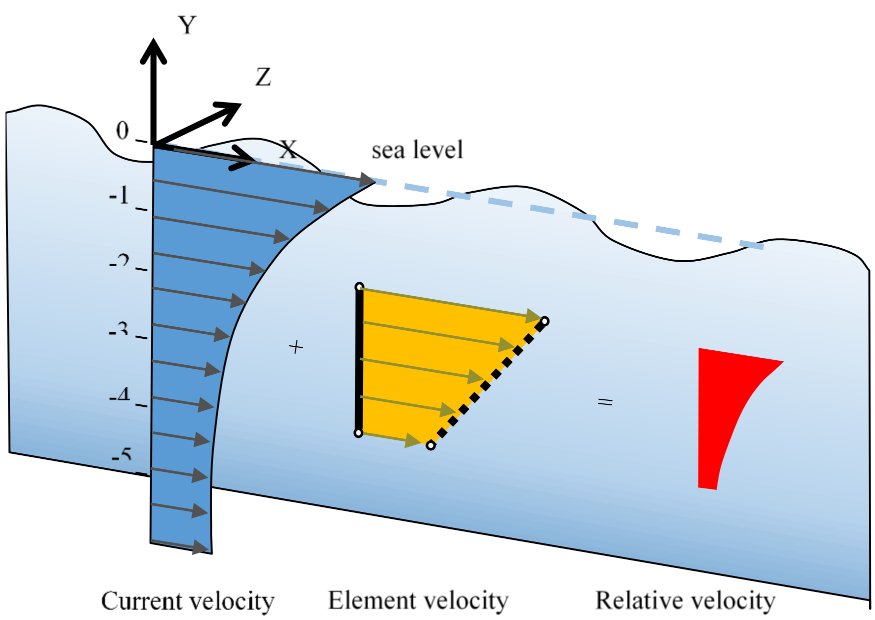

Figure 3-12: Viscous-drag damping load and the relative velocities.

Slika 3-12: Viskozno dušenje morskih tokov in prikaz relativnih hitrosti.

Load implementation can be carried out by applying a nonuniform load distribution to the submerged element. The current vector is defined as the global direction vector, and a table of the variable current profile along the selected axis is provided. The diameter of the element cross-section can be defined from a database catalog or can have a user-defined value. The hydrodynamic model coefficients are as follows: the drag coefficient, the density of water (approximately 1.0 t/m^3), and the exponent, which is set to 2 for viscous damping. The interaction factor f_{int} is commonly set to values near 1.0. Subdivision of the load distributes the nonuniform current loads along the finite element beam and thus enables a more exact force calculation. This feature has been implemented in *RM Bridge*, as depicted in Figure 3-13.

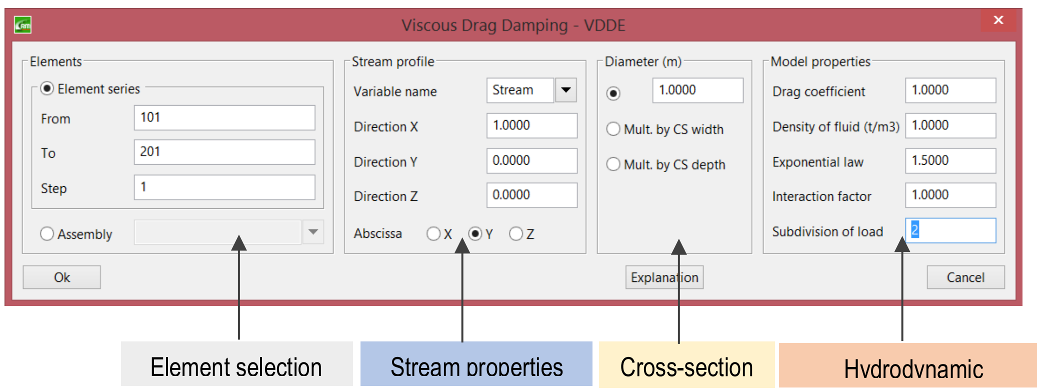

Figure 3-13: Implementation in RM Bridge [2].

Slika 3-13: Programiranje v programu RM Bridge [2].

3.9 Time-domain formulation

All the hydrodynamic effects presented in chapter 3 are summarized herein. Combining different hydrodynamic forces into a linear dynamic equation of motion yields:

$$\left(\mathbf{M}+\mathbf{M}_{\text{hy}}(\infty)\right)\ddot{\mathbf{u}}+\left(\mathbf{C}+\mathbf{C}_{\text{hy}}(\omega)\right)\dot{\mathbf{u}}+\left(\mathbf{K}+\mathbf{K}_{\text{hy}}\right)\mathbf{u}=\mathbf{F}_{\text{buy}}+\mathbf{F}_{\text{wave}}(t)+\mathbf{F}_{\text{cur}}(u) \tag{3.36}$$

The hydrodynamic effects are described in the "hydrodynamic" node at sea level relative to the pylon. The motion-induced hydrodynamic forces are calculated for each hull as a 6X6 matrix of added symmetric mass $\mathbf{M}_{\text{hy}}(\infty)$ and nonsymmetrical added damping $\mathbf{C}_{\text{hy}}(\omega)$. The hydrodynamic radiation forces and frequency-dependent participation are resolved via velocity convolution integration. The result of the convolution integral is a six-component force vector and is moved to the right side of the dynamic equilibrium. The infinite mass contribution is resolved implicitly on the left side of the dynamic equilibrium. The nonlinear and all the nonsymmetrical loads are moved to the right side, where they are resolved explicitly. The dynamic system is then resolved with the following final form:

$$\begin{aligned}\left(\mathbf{M}+\mathbf{M}_{\text{hy}}(\infty)\right)\ddot{\mathbf{u}}+\mathbf{C}\dot{\mathbf{u}}+\left(\mathbf{K}+\mathbf{K}_{\text{hy}}\right)\mathbf{u}=\mathbf{F}_{\text{buy}}+\mathbf{F}_{\text{wave}}(t)+\frac{1}{2}\rho C_d D\left(V_{\text{stream}}-V_{\text{elem}} f_{\text{int}}\right)\\ -\frac{2}{\pi}\int_0^t\int_0^\infty \mathbf{C}_{\text{hy}}(\omega)\cos(\omega t-\tau)\dot{\mathbf{u}}(\tau)\,d\omega\, d\tau\end{aligned} \tag{3.37}$$

Convolution integration is a time-consuming mathematical operation; hence, an efficient algorithm is necessary to evaluate the response. Several possibilities exist for improving the numerical efficiency. The calculation time is measured during implementation inside *RM Bridge* to investigate the numerical efficiency of the floating bridge analysis. The relatively long calculation time is due to many additional nonlinear effects, which cause an increase in the number of Newton-Raphson iterations. An average of 50 iterations is required to resolve the dynamic equilibrium convergence of floating bridges. This high number results in considerable additional numerical effort when evaluating the convolution integral areas inside the Newton-Raphson convergence. To reduce the calculation times, the convolution integration can be split into two parts, i.e., convolution before t_n and convolution participation of the last iterated time step:

$$\mathbf{q}_{\mathrm{hy}}(t) = \int_0^{t_{n+1}} \mathbf{I}_{\mathrm{hy}}(t-\tau)\ \dot{\mathbf{u}}(\tau)d\tau = \int_0^{t_n} \mathbf{I}_{\mathrm{hy}}(t-\tau)\ \dot{\mathbf{u}}(\tau)d\tau + \int_{t_n}^{t_{n+1}} \mathbf{I}_{\mathrm{hy}}(t-\tau)\ \dot{\mathbf{u}}(\tau)d\tau \tag{3.38}$$

This implementation speeds up the evaluation of the convolution integral up to 50 times and is beneficial for nonlinear structural responses. In addition, the retardation function $\mathbf{I}_{\mathrm{hy}}$ is precalculated and stored in the read access memory. Furthermore, different integration algorithms are tested, such as constant, linear and cubic integration rules. Linear integration offers the best accuracy-performance ratio and thus is chosen for the final implementation.

An interesting alternative is a state-space method that transforms the second-order convolution operations into a set of first-order linear system equations. The linear terms of this reduced matrix have to be fitted to the experimental hydrodynamic data. Thus, a linear system can be resolved with simple matrix multiplication operations, which results in significant computational efficiency compared to convolution. However, additional work on obtaining reliable matrices for an equivalent linear dynamic subspace system should not be neglected. This work is made possible with complicated expressions for fitting to self-excited forces, such as rationa and indicial fnctions, and requires user experience.

4 WIND LOAD ON BRIDGES

4.1 Preview

This chapter presents dynamic wind loads according to the strip theory of bridge aerodynamics [42]. The presented wind load formulations are suitable for the finite element method discretization of line-like bridge structures [43]. The wind load is a superposition of different force actions on a bridge strip section. The wind load effects are grouped as follows: I) mean wind, II) turbulent wind, III) self-excited motion and IV) vortex shedding loads, as depicted in Figure 4-1.

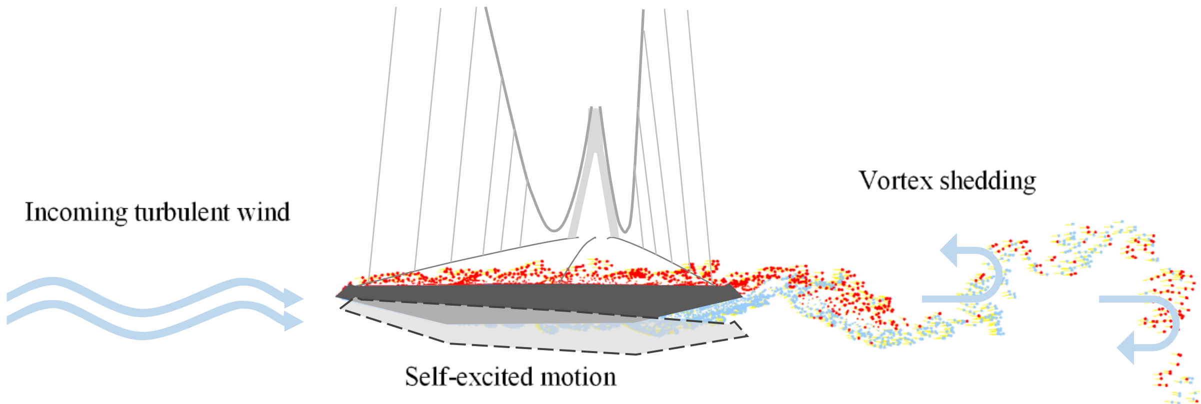

Figure 4-1: Different wind load components on a bridge deck section.

Slika 4-1: Različne vrste vetrnih obtežb na most.

Motion-induced load models can be simulated with steady aerodynamics, unsteady aerodynamics and nonlinear aerodynamics models. The popular QSS model is derived from the assumption of fully developed flow around the indicial wind angle. This approach is convenient for implementation due to the availability of aerodynamic input. This formulation is applied in the current time-domain floating bridge design and has been implemented in several commercial software programs. Unstable models are popular in aeroelastic research, where linearized flutter derivatives are especially convenient [44]. The wind tunnel measurements reveal that self-excited force models are more suited to capturing motion-induced forces than are QSS models, resulting in better accuracy in wind buffeting response prediction and opening up the possibility for aeroelastic investigations. The nonlinear structural response can be successfully resolved with a time-integration approach and requires a proper formulation for frequency-dependent self-excited forces. Rational functions are commonly used in time-domain investigations but are not often implemented in commercial codes. This research develops new possibilities for including a self-excited force model suitable for implementation in current floating bridge projects. An accurate prediction of fully coupled time-domain floating structures can be achieved by introducing a specifically tailored self-excited force formulation into the presented numerical scheme. This integration is made possible by using the existing hydrodynamic functionality inside the software together with the developed load models. New linear self-excited numerical models are developed and validated with wind tunnel measurements.

4.2 Turbulent wind description

The incoming wind vector $\boldsymbol{U}(t)$ is decomposed into a constant mean value $\boldsymbol{V}$ and fluctuations $\boldsymbol{v}(t)$ around the mean value, written in matrix notation as $\boldsymbol{U}(t) = \boldsymbol{V} + \boldsymbol{v}(t)$. The wind directions are described in a wind left-hand Cartesian coordinate system, where the component $u(t)$ is in the direction of the wind fluctuation, $v(t)$ is the vertical fluctuation in the reverse gravity direction, and $w(t)$ is the fluctuation in the horizontal direction, defined as:

$$\begin{bmatrix} U(t) \\ V(t) \\ W(t) \end{bmatrix} = \begin{bmatrix} V \\ 0 \\ 0 \end{bmatrix} + \begin{bmatrix} u(t) \\ v(t) \\ w(t) \end{bmatrix} \tag{4.1}$$

The wind field properties $\mathbf{U}$ are a function of the height and depend on the terrain roughness of the surrounding area. The wind flow is turbulent by nature and is commonly modeled with stochastic methods. Here, the Fourier transformations presented in Figure 3-8 are applied to model a homogeneous wind field. The information required for the determination of the load effect on a bridge commonly includes the mean wind profile, power spectrum, turbulence intensity and coherence of wind fluctuations. The wind field velocity (4.1) can be described as a fluctuating force around the mean wind velocity, as depicted in Figure 4-2.

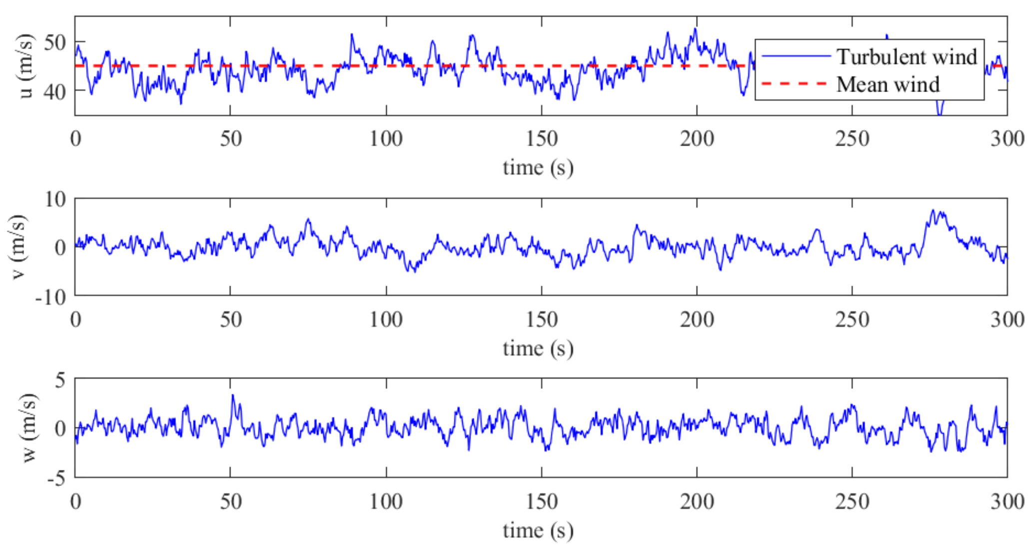

Figure 4-2: Example of turbulent wind fluctuations.

Slika 4-2: Prikaz primera simulacije turbulentnega vetra.

Wind fluctuations are modeled by time-dependent signals, and the input is commonly provided by a single-sided PSD [45] [46] [47]. The wind spectra of turbulent wind describe the amount of energy associated with different frequencies, as depicted in Figure 4-3. Typically, three spectra together with the associated coherence describe the turbulent wind field. The wind power spectrum is commonly presented as a product of the variance and its normalized frequency PSD distribution $S(\omega) = \sigma \cdot PSD(\omega)$.

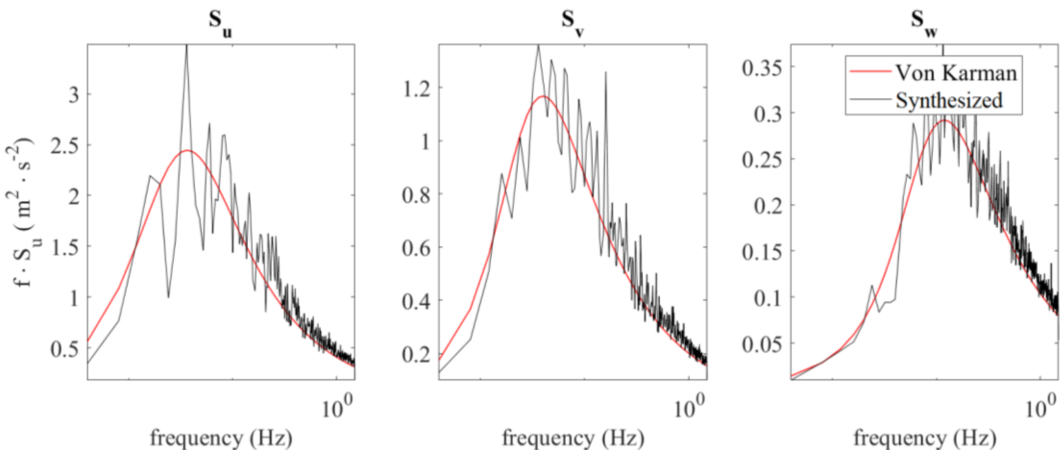

Figure 4-3: Normalized PSD and the corresponding time-domain transformation [48].

Slika 4-3: Normaliziran turbulentni spekter vetra in pripadajoča časovna transformacija signala [48].

For the time-domain simulations, reverse engineering from the frequency power spectra to time-domain signals is possible via IFT techniques, as shown in Figure 3-8. These synthesized signals do not exactly reproduce the input spectrum, as observed in Figure 4-3; however, they are statistically achieved for an average realization in Figure 4-7. The nonhomogeneous wind field is described by stochastic auto- and cross-correlation spectra, which define the wind field fluctuations. The fluctuations across the bridge are correlated time-varying fluctuations, which are described by the correlated wind fluctuations [49] [50] [51] [52] formulation as:

$$\mathbf{v}(t)=\sum_{j=1}^{\mathrm{M}}\sum_{k=1}^{\mathrm{N}}\sqrt{2\Delta\omega}\mathbf{S}_{\mathrm{ij}}\left(\omega_k\right)\cos\left(\omega_k t+\psi_{i,k}\right) \tag{4.2}$$

where i is the wind node number, k is the frequency, $\mathbf{S}_{\mathrm{ij}}$ is the decomposed correlated wind spectrum matrix, ω is the frequency and $\psi_{i,k}$ is the random phase angle of the white noise spectrum. In this approach, the correlation between different directions and wind nodes along the bridge is introduced. The correlated wind nodes are assembled in the form of a symmetrical lower triangular matrix, which is defined as follows:

$$\mathbf{S}_{\mathrm{ij}}=\begin{bmatrix}\mathbf{S}_{11} & \cdots & symm\\ \mathbf{S}_{i1} & \mathbf{S}_{ij} & \vdots\\ \mathbf{S}_{M1} & \mathbf{S}_{Mj} & \mathbf{S}_{MM}\end{bmatrix} \tag{4.3}$$

where the power spectra for two separated points i and j are calculated with an average spectrum and its coherence as:

$$\mathbf{S}_{ij}=\sqrt{\mathbf{S}_i\mathbf{S}_j}\,\mathbf{Coh}\left(\omega,\Delta s\right) \tag{4.4}$$

To solve (4.2), several techniques are available [53] [54] [55]. In this work, an inverse discrete fast Fourier transform (IDFFT) algorithm is applied and implemented. Sufficiently refined time, frequency and space discretization are required for accurate wind fluctuation calculations in the time domain. This represents a computational challenge for large 5 km long floating bridges.

Floating bridges are commonly represented by larger complex finite element models and require long simulation times [3] [56]. The time series generation (4.2) of approximately 40000 wind nodes is a challenging task for PCs. Good concept development and preformat numerical algorithms can considerably reduce the computational time. Therefore, a specifically tailored solution is programmed into the software increase the speed of the calculations. The first improvement is the generation of wind turbulence on the wind plane, as shown in Figure 4-4. From the wind plane, wind turbulence is interpolated on a finite element mesh. The wind plane can have independent space discretization based on wind generation requirements. Coarse frequency discretization is added in (4.2), where the assembly of (4.3) is performed at predefined frequencies of the wind power spectrum. To achieve the required fine discretization of frequencies for the IDFFT operation, a linear interpolation between different assembly planes is applied, as presented in Figure 4-4. The IDFFT algorithm is significantly faster than the trigonometric cosine operation of the IDFFT algorithms. The parallel solver in (4.3) is added to further increase the calculation speed. The directly used equation (4.2) would require more than 1 month of computation time. After the described algorithms are introduced, the computation time is reduced to approximately 15 min, achieving a speed-up factor of approximately 10^5. This work to develop an efficient algorithm for time series calculations is important for achieving an effective workflow. The presented implementation is applied to the example of the floating bridge time-domain simulations presented in chapter 6.

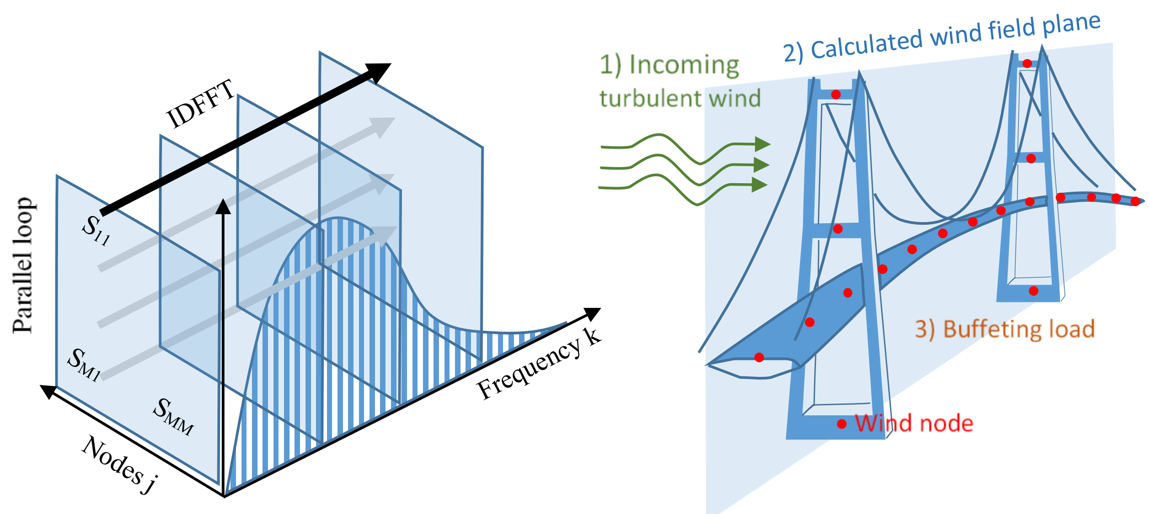

Figure 4-4: IDFFT algorithm calculations (left) and the wind plane (right).

Slika 4-4: IDFFT algoritem za izračun turbulentnega vetra (levo) in ravnina vetra (desno).

A demonstration is presented for a homogeneous wind field calculation. The wind is calculated for multiple points across the bridge length at an elevation of 20 m. The described wind field is calculated with equations from (4.2) to (4.4). The time scale is $t_{\mathrm{end}} = 2000s$ with $\Delta t = 0.2s$, and the frequency sampling is $f = \{0 \text{ - } 5\}$ Hz with $\Delta f = 5 \cdot 10^{-5}s$. The wind field is simulated for all three wind fluctuations *u, v*, and *w*. A constant mean wind *V*=45 m/s is applied over all domains, ensuring homogeneous properties. The coherence function is dependent on the frequency of the wind fluctuations and the distance between nodes. Several coherence modeling formulations are available, among which the popular exponential decay model is applied, as follows:

$$\begin{aligned} Coh_{\mathrm{u}} &= e^{-\frac{f}{\mathrm{V}}\sqrt{(\mathrm{C_{ux}}dx)^2+(\mathrm{C_{uy}}dy)^2+(\mathrm{C_{uz}}dz)^2}} \\ Coh_{\mathrm{v}} &= e^{-\frac{f}{\mathrm{V}}\sqrt{(\mathrm{C_{vx}}dx)^2+(\mathrm{C_{vy}}dy)^2+(\mathrm{C_{vz}}dz)^2}} \\ Coh_{\mathrm{w}} &= e^{-\frac{f}{\mathrm{V}}\sqrt{(\mathrm{C_{wx}}dx)^2+(\mathrm{C_{wy}}dy)^2+(\mathrm{C_{wz}}dz)^2}} \end{aligned} \quad \text{where C} = \begin{array}{cc} \begin{matrix} dx & dy & dz \end{matrix} & \\ \begin{bmatrix} 0 & 4 & 8 \\ 0 & 4 & 8 \\ 0 & 4 & 8 \end{bmatrix} & \begin{matrix} u \\ v \\ w \end{matrix} \end{array} \tag{4.5}$$

Here, f is the wind oscillation frequency in Hz, $\mathrm{C_{ij}}$ is the coherence exponential decay coefficient matrix, and dx, dy, dz are the length distances between wind nodes, where the length vector is rotated in the same direction as the incoming wind vector **U**. For a nonhomogeneous wind field, the average wind speeds between two nodes are taken as $V_{\mathrm{ij}} = (V_{\mathrm{i}} + V_{\mathrm{j}})/2$. The wind fluctuation can be described by various wind spectra, where a proper spectral application should be investigated for each construction side individually. In this thesis, the Kármán [57] continuous gust wind fluctuation is modeled as:

$$\begin{aligned} S_{\mathrm{uu}} &= \frac{(\mathrm{TI_u V})^2}{f} \cdot \left[4\frac{f}{\mathrm{V}}L_{\mathrm{u}} \Big/ \left(1+70.8\left(\frac{f}{\mathrm{V}}L_{\mathrm{u}}\right)^2\right)^{5/6} \right] \\ S_{\mathrm{vv}} &= \frac{(\mathrm{TI_v V})^2}{f} \cdot \left[4\frac{f}{\mathrm{V}}L_{\mathrm{v}}\left(1+755\left(\frac{f}{\mathrm{V}}L_{\mathrm{v}}\right)^2\right) \Big/ \left(1+283\left(\frac{f}{\mathrm{V}}L_{\mathrm{v}}\right)^2\right)^{11/6} \right] \\ S_{\mathrm{ww}} &= \frac{(\mathrm{TI_w V})^2}{f} \cdot \left[4\frac{f}{\mathrm{V}}L_{\mathrm{w}}\left(1+755\left(\frac{f}{\mathrm{V}}L_{\mathrm{w}}\right)^2\right) \Big/ \left(1+283\left(\frac{f}{\mathrm{V}}L_{\mathrm{w}}\right)^2\right)^{11/6} \right] \\ S_{\mathrm{uv}} &= S_{\mathrm{uw}} = S_{\mathrm{vu}} = S_{\mathrm{vw}} = S_{\mathrm{wu}} = S_{\mathrm{wv}} = 0 \end{aligned} \tag{4.6}$$

Here the integral length scales are selected as L_{u}= 180m, $\mathrm{L_v}$= 120m, $\mathrm{L_w}$= 40m , and the turbulence intensities are $\mathrm{TI_u}$= 6.66%, $\mathrm{TI_v}$= 4.44%, and $\mathrm{TI_w}$= 2.22%. The standard deviation is defined as $\sigma = V \cdot \mathrm{TI}/100\%$, resulting in σ_{u}= 3 m/s, σ_{v}= 2 m/s, and σ_{w}= 1 m/s. The defined wind power spectra in (4.6) are presented in Figure 4-3 in red, and the values numerically calculated with (4.2) are presented as fluctuating black curves. The three wind fluctuations calculated using (4.2) are presented for a single wind node, as shown in Figure 4-2. The wind field presented corresponds to a length of 2000 m (see Figure 4-5) and has a longitudinal component *u*(*t*). The extremely high (yellow) peak velocities are visually clustered in the reefs and represent an average integral length scale $L_{\mathrm{u}}= 180$ m, as introduced in (4.6).

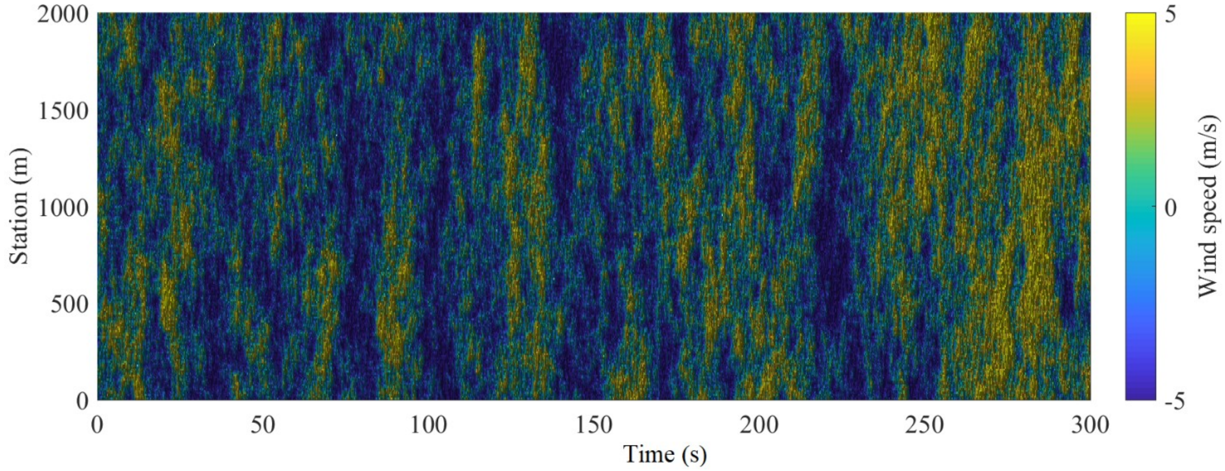

Figure 4-5: Homogeneous wind field fluctuation u(t) for a span length of 2000 m at a height of 20 m.

Slika 4-5: Homogena vetrna turbulenca u(t) v dolžini 2000 m, na višini 20 m.

Different parameters are investigated to achieve an accurate reproduction of the wind field from the wind spectra. Eq. (4.2) is used in Monte Carlo simulations and replaces the unknown phases with random variables [58]. The time and frequency domains are similar in wave generation (3.13) . To satisfy a statistical average, a set of 50 wind realizations with different random phase angles are calculated. Fifty different realizations of three components of the wind time series are presented in Figure 4-6. The RMS values of all signals agrees well with the input standard deviation σ and for the turbulence intensities. Possible deviations can lead to an investigation of the correctness of the chosen time scale or frequency scale. The scattered peak factors represent the ratio of the absolute maximal value to the standard deviation. The scattered maximal structural response calculation requires several wind time series calculations and the application of statistical methods.

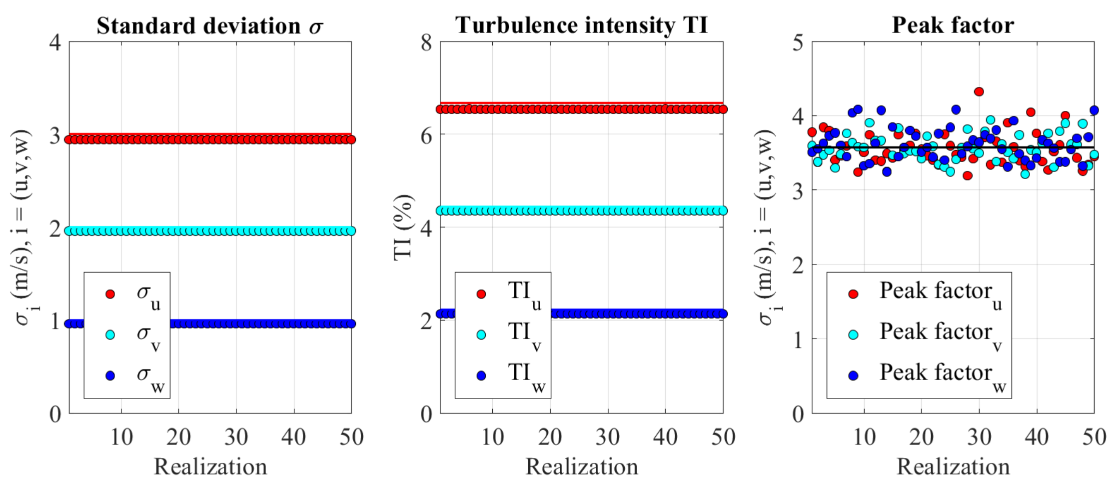

Figure 4-6: Properties for 50 different turbulent time series realizations

Slika 4-6: Lastnosti tridesetih simulacij turbulentnega vetra.

The generated time series realizations are transformed back to the wind spectrum to confirm the correct transformation. On average, turbulent wind time series tend to reproduce the energy of the input wind spectra. Figure 4-7 shows the calculated spectrum and coherence defined in Eq. (4.5), with an exponential decay factor $C_{uy} = 4$ and a separation of 20 m.

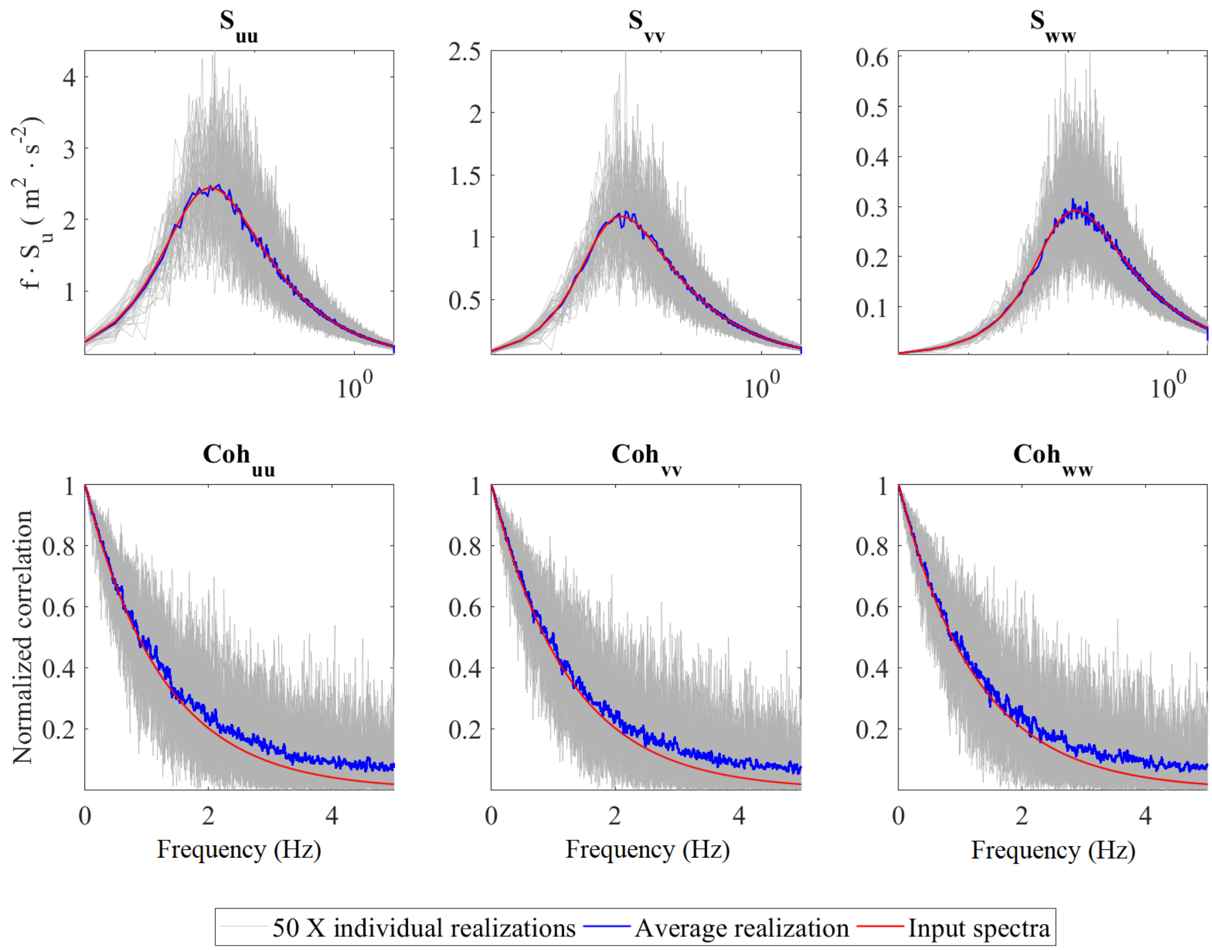

Figure 4-7: PSD of the generated time series and coherence in wind direction u.

Slika 4-7: Spektri in koherenca za različne časovne realizacije, prikaz v smeri vetra u.

Invariant processes are often used in bridge design practice and are verified in the literature. The wind field is often measured and represented as an invariant 10-minute peak period wind event. The simulated stationary invariant dynamic wind involves simplifications of the onsite-measured results, with the intention of covering all extreme responses. Most likely, 5 km long floating bridges will be exposed to variant and nonhomogeneous winds. To cover the worst-case scenario, some bridge standard recommendations involve load scenarios of nonhomogeneity in both the vertical and longitudinal directions [59] [60]. The methods described in (4.2) can be applied to model nonhomogeneous wind fields, such as the mean wind variation over the height. Thus, directly applying the methods in (4.3) can result in some numerical difficulties in the Cholesky decomposition, which requires specifically designed algorithms. Over large distances, extreme wind scenarios could occur for nonhomogeneous time variant wind events. To account for these variant scenarios, more sophisticated wind spectra analyses might be introduced. A wavelet transformation is a possible candidate for synthesizing and investigating the correlation between different variant time processes [61]. The wavelet transformation involves the frequency decomposition of continuous-time sections and is well applied in biomedicine, spectrography, image processing, the aerospace industry, etc. The transformation calculates the magnitude-squared correlation, evaluated between 1 and 0, presented as varying colors in the figure below. The varying frequency contest can be observed in the investigated time period. Figure 4-8 demonstrates the wavelet transformation of the invariant homogeneous wind fluctuation generated in Figure 4-5.

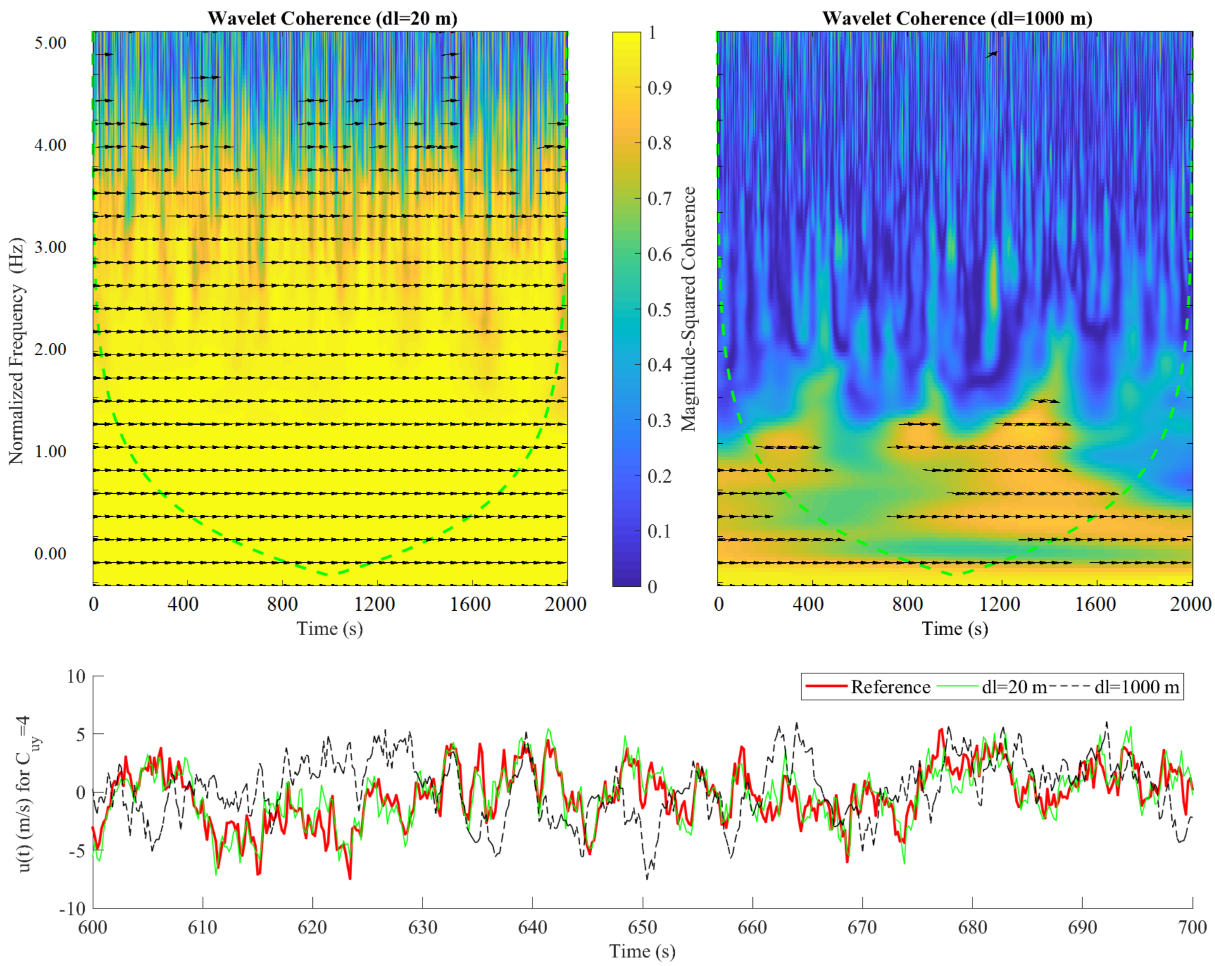

Figure 4-8: Wavelet for homogeneous invariant transformation of u(t) for 20 m and 1000 m separated nodes.

Slika 4-8: Wavelet transformcija vetra vzdolž 1000 m mostu na višini 20 m.

The time-invariant wind field is almost fully correlated over time for nodes separated by a short distance of 20 m, where a low correlation is observed for a separation of 1000 m. The imaginary phases of transformation are presented with arrows, where the arrow directions represent the phase angles. These methods have possible applications in extreme wind synthesis for long-span floating bridges. They could assist in the investigation of nonhomogeneity and variant winds to better match the onsite wind measurements and improve extreme wind event investigations.

4.3 Dynamic wind load

The aerodynamic wind forces are calculated according to the strip theory of a line-like structure [54] [62] [63]. The aerodynamic forces are defined with dimensionless coefficients, i.e., the drag C_D in the wind direction, the lift C_L in the vertical direction and the moment C_M around the element axis. The aerodynamic force is derived from the Bernoulli equation. This formulation allows the scaling of the aerodynamic forces measured in wind tunnels to real bridge sizes. The mean wind force $\mathbf{F}_\mathrm{mean}$ vector is defined for the central wind flow indicial angle α and is expressed as:

$$\mathbf{F}_\mathrm{mean} = \frac{1}{2}\rho V^2 B \begin{bmatrix} C_\mathrm{D}(\alpha) \\ C_\mathrm{L}(\alpha) \\ BC_\mathrm{M}(\alpha) \end{bmatrix} \tag{4.7}$$

where ρ is the air density, V is the laminar mean wind speed and B is the normalization width of the strip cross-section. The wind load is defined for a unit length of 1 m. The dynamic wind load formulation is a resultant force of the mean wind load component, incoming wind turbulence component, structural velocities and displacements. The nonlinear wind buffeting formulation $\mathbf{F}_\mathrm{buff,nl}$ is expressed as:

$$\mathbf{F}_\mathrm{buf,nl}(t) = \frac{1}{2}\rho V_\mathrm{tot}^2(t) B \begin{bmatrix} C_\mathrm{D}(\alpha+\beta(t)) \\ C_\mathrm{L}(\alpha+\beta(t)) \\ BC_\mathrm{M}(\alpha+\beta(t)) \end{bmatrix} \tag{4.8}$$

where the time variant resultant wind velocity V_tot and effective angle of wind attack β are defined by:

$$\begin{aligned} V_\mathrm{tot}^2(t) &= \left(V + u(t) - \dot{u}_\mathrm{y}(t)\right)^2 + \left(v(t) - \dot{u}_\mathrm{z}(t)\right)^2 \\ \beta(t) &= \tan\left(\frac{v(t) - \dot{u}_\mathrm{z}(t)}{V + u(t) - \dot{u}_\mathrm{y}(t)}\right) \end{aligned} \tag{4.9}$$

The velocity vector components according to QSS theory are presented in Figure 4-9.

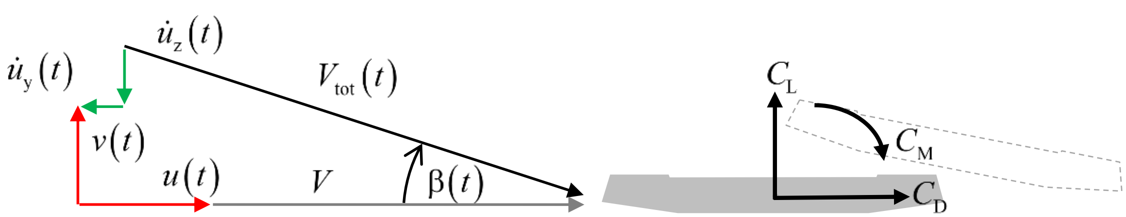

Figure 4-9: Wind buffeting load vector components on a bridge segment.

Slika 4-9: Obtežbeni vektor turbulentnega vetra na most.

Linearization of the wind buffeting formulation (4.8) according to the QSS airflow theory is common [54]. The first step involves linearization of the aerodynamic derivatives around the mean wind angle α with the help of the aerodynamic derivatives $C_{\mathrm{D}}', C_{\mathrm{L}}', C_{\mathrm{M}}'$ as:

$$\begin{aligned} C_{\mathrm{D}}\left(\alpha+\beta(t)\right) &= C_{\mathrm{D}}(\alpha)+\beta(t)C_{\mathrm{D}}' \\ C_{\mathrm{L}}\left(\alpha+\beta(t)\right) &= C_{\mathrm{L}}(\alpha)+\beta(t)C_{\mathrm{L}}' \\ C_{\mathrm{M}}\left(\alpha+\beta(t)\right) &= C_{\mathrm{M}}(\alpha)+\beta(t)C_{\mathrm{M}}' \end{aligned} \tag{4.10}$$

The second linearization neglects the small squared terms in (4.9) relative to the mean wind V:

$$\begin{aligned} V_{\mathrm{tot}}^2(t) &\approx V^2+Vu(t)-V\dot{u}_{\mathrm{y}}(t) \\ \beta(t) &\approx \frac{v(t)}{V}-\frac{\dot{u}_{\mathrm{z}}(t)}{V} \end{aligned} \tag{4.11}$$

Substituting the linearization of (4.10) and (4.11) into (4.8) forms the well-known linear wind buffeting matrices. They are superpositions of the mean wind load $\mathbf{F}_{\mathrm{mean}}$, turbulent wind load $\mathbf{F}_{\mathrm{buf}}$, quasi-static aerodynamic damping $\mathbf{C}_{\mathrm{qss}}$ and aerodynamic stiffness $\mathbf{K}_{\mathrm{qss}}$. The total load linearized wind buffeting format is expressed as:

$$\begin{aligned} \mathbf{F}_{\mathrm{buf,lin}} &= \mathbf{F}_{\mathrm{mean}}+\mathbf{F}_{\mathrm{buf}}\mathbf{v}(t)+\mathbf{C}_{\mathrm{qss}}\dot{\mathbf{u}}+\mathbf{K}_{\mathrm{qss}}\mathbf{u} \\ &= \frac{1}{2}\rho V^2 B\begin{bmatrix} C_{\mathrm{D}} \\ C_{\mathrm{L}} \\ BC_{\mathrm{M}} \end{bmatrix}+\frac{\rho VB}{2}\begin{bmatrix} 2C_{\mathrm{D}} & C_{\mathrm{D}}'-C_{\mathrm{L}} \\ 2C_{\mathrm{L}} & C_{\mathrm{L}}'+C_{\mathrm{D}} \\ 2BC_{\mathrm{M}} & BC_{\mathrm{M}}' \end{bmatrix}\begin{Bmatrix} u(t) \\ w(t) \end{Bmatrix} \\ &-\frac{\rho VB}{2}\begin{bmatrix} 2C_{\mathrm{D}} & C_{\mathrm{D}}'-C_{\mathrm{L}} & 0 \\ 2C_{\mathrm{L}} & C_{\mathrm{L}}'+C_{\mathrm{D}} & 0 \\ 2BC_{\mathrm{M}} & BC_{\mathrm{M}}' & 0 \end{bmatrix}\begin{Bmatrix} \dot{u}_{\mathrm{y}} \\ \dot{u}_{\mathrm{z}} \\ \dot{u}_{\mathrm{rx}} \end{Bmatrix}-\frac{\rho V^2 B}{2}\begin{bmatrix} 0 & 0 & C_{\mathrm{D}}' \\ 0 & 0 & C_{\mathrm{L}}' \\ 0 & 0 & BC_{\mathrm{M}}' \end{bmatrix}\begin{Bmatrix} u_{\mathrm{y}} \\ u_{\mathrm{z}} \\ u_{\mathrm{rx}} \end{Bmatrix} \end{aligned} \tag{4.12}$$

The linearized $\mathbf{F}_{\mathrm{buf,lin}}$ formulation can be inserted into the Newark time-integration scheme as:

$$\mathbf{M}\ddot{\mathbf{u}}+\left(\mathbf{C}+\mathbf{C}_{\mathrm{qss}}\right)\dot{\mathbf{u}}+\left(\mathbf{K}+\mathbf{K}_{\mathrm{qss}}\right)\mathbf{u}=\mathbf{F}_{\mathrm{mean}}+\mathbf{F}_{\mathrm{buf}}\mathbf{v}(t) \tag{4.13}$$

This formulation is suitable for both time history integration and modal decomposition [64] [65] [66] [67]. The linearization might make an important contribution and must be investigated for individual projects. This formulation is successfully implemented in floating bridge design and is discussed in chapter 6.

4.4 Self-excited aeroelastic forces

In the early 20th century, long-span bridges were built extensively and provided a cost-efficient solution for longer spans. The second-order theory was developed to incorporate the cable sagging effect on structural stiffness, resulting in up to 30% material savings and making slender structures more sensitive to dynamic vibrations. The well-known Tacoma Narrows bridge collapse of 1940 was due to a very low wind speed of only V=17 m/s. The detailed investigation concluded that the collapse was caused by then-unknown motion-induced phenomenon. The first airfoil theory of the 20th century was developed in the aerospace industry, and its principles were applied in the Scanlan theory of coupled flutter instability calculation [22]. This formulation enabled the investigation of the aeroelastic critical wind speeds of flexible structures. The inputs are linearized frequency-dependent flutter derivatives and are valid around the mean wind direction α. The dimensionless characteristics of the cross-section can be measured in a wind tunnel or can be calculated with modern CFD tools [68] [69]. The developed numerical methods have been validated using the experimental results obtained from the wind tunnel laboratory at NTNU Trondheim [70]. A modern force vibration rig can reproduce various deck motions and very accurately measure the self-excited force. Sophisticated motion-controlled sections are controlled by six servomotors, as shown in Figure 4-10.

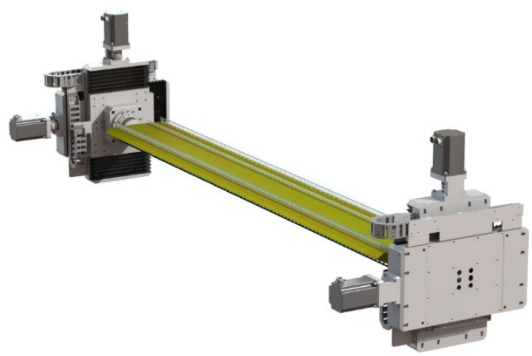

Figure 4-10: Wind tunnel rig at NTNU Trondheim [71].

Slika 4-10: Eksperimentalni instrument iz vetrovnika NTNU v Trondheimu [71].

The QSS motion-induced formulation in (4.12) is modeled by constant aerodynamic damping $\mathbf{C}_{\mathrm{qss}}$ and the stiffness matrix $\mathbf{K}_{\mathrm{qss}}$. The wind tunnel measurements show that the QSS models fail to properly reproduce aeroelastic instability and can lead to a poor aerodynamic damping estimate. Aeroelastic formulations are therefore preferred for flexible floating bridge structures and will deliver accurate results [72] [73] [74] [75] [76]. The nonsteady self-excited matrices $\mathbf{C}_{\mathrm{se}}(K)$ and $\mathbf{K}_{\mathrm{se}}(K)$ replace the steady-state aerodynamic matrices $\mathbf{C}_{\mathrm{qss}}$ and $\mathbf{K}_{\mathrm{qss}}$ in (4.12). The load directions are identical to the direction presented in Figure 4-9.

The measured results are commonly normalized on cross-section width B. The self-excited forces per unit length are expressed as:

$$\mathbf{F}_{\text{se}} = \mathbf{C}_{\text{se}}(K)\dot{\mathbf{u}} + \mathbf{K}_{\text{se}}(K)\mathbf{u} = \\ -\frac{\rho VBK}{2}\begin{bmatrix} P_1^* & P_5^* & BP_2^* \\ H_5^* & H_1^* & BH_2^* \\ BA_5^* & BA_1^* & B^2A_2^* \end{bmatrix}\begin{Bmatrix} \dot{u}_{\text{y}} \\ \dot{u}_{\text{z}} \\ \dot{u}_{\text{rx}} \end{Bmatrix} - \frac{\rho V^2K^2}{2}\begin{bmatrix} P_4^* & P_6^* & BP_3^* \\ H_6^* & H_4^* & BH_3^* \\ BA_6^* & BA_4^* & B^2A_3^* \end{bmatrix}\begin{Bmatrix} u_{\text{y}} \\ u_{\text{z}} \\ u_{\text{rx}} \end{Bmatrix} \tag{4.14}$$

The reduced frequency $K = \omega B/V$ is defined by the circular bridge deck frequency $\omega = 2\pi f$ [rad/s]. The flutter derivatives are represented by the drag P_i^*, lift H_i^* and moment A_i^* forces, where $i = (1, 2,...,6)$. The symbol * on the flutter derivatives indicates that the values are dimensionless and a function of the normalized reduced velocity $\hat{V} = \omega B/V$. This formulation is commonly applied in aeroelastic instability checks and is suitable for linearized wind buffeting in frequency-domain calculations. The wind effect, with the self-excited formulation substituted into the time-domain equation of motion, can be written as:

$$\mathbf{M}\ddot{\mathbf{u}} + \left(\mathbf{C} + \mathbf{C}_{\text{se}}(\omega)\right)\dot{\mathbf{u}} + \left(\mathbf{K} + \mathbf{K}_{\text{se}}(\omega)\right)\mathbf{u} = \mathbf{F}_{\text{mean}} + \mathbf{F}_{\text{buf}}\mathbf{v}(t) \tag{4.15}$$

The resolution of the frequency-dependent terms is made possible by convolution integration in the time domain. This research investigates several convolution formulations and different interpolation functions. The nonsymmetrical infinite aeroelastic matrices are moved to the left side of the equation. The frequency-dependent part can be resolved as aeroelastic damping with the hydrodynamic convolution integration presented in chapter 3.6. The implemented approach is flexible and can incorporate different self-excited models into the software solution as:

$$\mathbf{M}\ddot{\mathbf{u}} + \left(\mathbf{C} - \mathbf{C}_{\text{se,v}}^{\infty}\right)\dot{\mathbf{u}} + \left(\mathbf{K} - \mathbf{K}_{\text{se,v}}^{\infty}\right)\mathbf{u} = \mathbf{F}_{\text{mean}} + \mathbf{F}_{\text{buf}}\mathbf{v}(t) + \\ \frac{2}{\pi}\int_0^t\int_0^\infty \left[\mathbf{C}_{\text{se}}(\omega) - \mathbf{C}_{\text{se,v}}^{\infty}\right]\cos\left(\omega(t-\tau)\right)\dot{\mathbf{u}}(\tau)\,d\omega\,d\tau \tag{4.16}$$

This approach does not require additional implementation and reuses existing approaches available in the hydrodynamic software. To substitute the self-excited formulation into (4.16), the flutter equations have to be rewritten in a proper mathematical format. Several alternatives are presented and discussed in the following chapter.

4.5 Time-domain formulation of the self-excited forces

The flutter derivatives are measured at discrete points for a range of reduced frequencies. An interpolation function is applied for a continuous presentation. The fitted frequency-dependent function is then suitable for transferring the self-excited forces into the time domain. Equation (4.14) is valid for only a single-frequency harmonic motion. By introducing the principle of superposition, this can be extended to any periodic or aperiodic motion by applying the Fourier integral representation [77] [78] [79] [80]. The frequency-domain response of self-excited forces $\mathbf{G}_{\mathrm{q}}$ is expressed as:

$$\mathbf{G}_{\mathrm{q}}(\omega)=\mathbf{F}_{\mathrm{se}}(\omega)\mathbf{G}_{\mathrm{u}}(\omega) \tag{4.17}$$

where $\mathbf{G}_{\mathrm{q}}$ is the Fourier transform of the self-excited force vector, $\mathbf{G}_{\mathrm{u}}$ is the Fourier transform of the displacement vector, and $\mathbf{F}_{\mathrm{se}}$ is the self-excited transfer function matrix. The transfer matrix converges the displacement into self-excited forces and is defined by:

$$\mathbf{F}_{\mathrm{se}}(\omega)=i\omega\mathbf{C}_{\mathrm{se}}\left(\omega\right)+\mathbf{K}_{\mathrm{se}}\left(\omega\right) \tag{4.18}$$

Here, i is the imaginary unit, and ω is the oscillation frequency in radians. The self-excited force transfer function (4.18) is defined for flutter derivatives (4.14) as:

$$\mathbf{F}_{\mathrm{se}}(K)=\frac{1}{2}\rho V^2\begin{bmatrix} K^2(P_1^*i+P_4^*) & K^2(P_5^*i+P_6^*) & K^2B(P_2^*i+P_3^*) \\ K^2(H_5^*i+H_6^*) & K^2(H_1^*i+H_4^*) & K^2B(H_2^*i+H_3^*) \\ K^2B(A_5^*i+A_6^*) & K^2B(A_1^*i+A_4^*) & K^2B^2(A_2^*i+A_3^*) \end{bmatrix} \tag{4.19}$$

The impulse response matrix $\mathbf{I}_{\mathrm{se}}$ is obtained by taking the Fourier transform of the transfer function $\mathbf{F}_{\mathrm{se}}$ as:

$$\mathbf{I}_{\mathrm{se}}(t)=\frac{1}{2\pi}\int_{-\infty}^{\infty}\mathbf{F}_{\mathrm{se}}(\omega)e^{i\omega t}d\omega \tag{4.20}$$

where $e^{i\omega t}=cos(\omega t)+i\cdot\sin(\omega t)$ is a complex trigonometric vector. The time-domain counterpart is obtained by applying the convolution theorem and integrating via the displacement history as:

$$\mathbf{q}_{\mathrm{u}}(t)=\int_{-\infty}^{\infty}\mathbf{I}_{\mathrm{se}}(t-\tau)\,\mathbf{u}(\tau)d\tau \tag{4.21}$$

An alternative calculation using the Fourier transform and convolution over the velocity histories is developed. To reproduce the same self-excited forces using a higher-motion derivative, the transfer function should be modified, which can be achieved by investigating the relation between the Fourier derivatives of the displacement and velocity vectors:

$$\begin{aligned} &\mathbf{G}_{\mathrm{u}}(\omega) = e^{i\omega t} && \text{displacements} \\ &\mathbf{G}_{\mathrm{v}}(\omega) = \frac{1}{i\omega} e^{i\omega t} && \text{velocities} \end{aligned} \tag{4.22}$$

Therefore, the transfer function of the displacements (4.18) is divided by $i\omega$ to ensure that (4.17) and (4.23) provide equivalent responses. The self-excited force $\mathbf{G}_{\mathrm{q}}$ of the velocity formulation is defined as:

$$\mathbf{G}_{\mathrm{q}}(\omega) = \mathbf{H}_{\mathrm{se}}(\omega)\mathbf{G}_{\mathrm{v}}(\omega) \tag{4.23}$$

where $\mathbf{G}_{\mathrm{v}}$ is the Fourier transform vector of the structural velocity vector, $\mathbf{H}_{\mathrm{v}}$ is the transfer function matrix for velocities and $\mathbf{G}_{\mathrm{q}}$ is the frequency-dependent self-excited force vector. The velocity transfer function is:

$$\mathbf{H}_{\mathrm{se}}(\omega) = \mathbf{C}_{\mathrm{se}}\left(\omega\right) + \frac{1}{i\omega}\mathbf{K}_{\mathrm{se}}\left(\omega\right) \tag{4.24}$$

The flutter derivative transfer function is expressed as:

$$\mathbf{H}_{\mathrm{se}}(K) = \frac{1}{2}\rho VB \begin{bmatrix} K(P_1^* - iP_4^*) & K(P_5^* - iP_6^*) & KB(P_2^* - iP_3^*) \\ K(H_5^* - iH_6^*) & K(H_1^* - iH_4^*) & KB(H_2^* - iH_3^*) \\ KB(A_5^* - iA_6^*) & KB(A_1^* - iA_4^*) & KB^2(A_2^* - iA_3^*) \end{bmatrix} \tag{4.25}$$

The velocity transfer matrix now switches components into real damping terms and imaginary stiffness terms. The Fourier transform of the velocity transfer function matrix yields the impulse response function $\mathbf{J}_{\mathrm{se}}$:

$$\mathbf{J}_{\mathrm{se}}(t) = \frac{1}{2\pi}\int_{-\infty}^{\infty} \mathbf{H}_{\mathrm{se}}(\omega) e^{i\omega t} d\omega \tag{4.26}$$

The convolution theorem calculates the time-domain response by integrating the impulse response via the velocity history as:

$$\mathbf{q}_{\mathrm{se}}(t) = \int_{-\infty}^{\infty} \mathbf{J}_{\mathrm{se}}(t-\tau)\dot{\mathbf{u}}(\tau) d\tau \tag{4.27}$$

4.6 Parametric modeling of self-excited forces

Rational functions (RFs) and indicial functions are commonly used to interpolate scattered flutter derivative measurements. Both functions are especially suited for time-domain applications and provide an analytical solution expression. The fitted expression has an inherited tendency to converge to a constant value at infinite frequency ∞. This work presents only RFs; however, similar principles can be applied to indicial functions. An example involving a single DOF is demonstrated, and analogical expressions are derived for the coupled motion of equations presented from (4.18) to (4.20). The general dimensionless form of transfer functions can be represented as a function of reduced frequency K. The following fitting expression of RFs has been frequently used in the literature [81] [72]:

$$F_{\mathrm{se}}(K) = \frac{1}{2}\rho V^2 (a_1 + a_2 iK + a_3 (iK)^2 + \sum_{l=1}^{N-3} a_{l+3} \frac{iK}{iK + d_l}) \tag{4.28}$$

where a_{n} is a fitting coefficient, d_l is a pole fitting coefficient and N is the number of poles needed to fit the data. For practical applications, approximately three poles are used to fit the experiments. The coefficients related to inertia a_3 are neglected due to their minimal participation. For the vertical lift direction, the rational expression is fitted to the flutter derivatives as:

$$\frac{1}{2}\rho B^2 \omega^2 (H_1^* i + H_4^*) = \frac{1}{2}\rho V^2 \left(a_1 + a_2 iK + \sum_{l=1}^{N-3} a_{l+3} \frac{iK}{iK + d_l} \right) \tag{4.29}$$

To interpolate (4.28), i.e., the aeroelastic transfer function, Eq. (4.19) is split into real and imaginary components. The real part is fitted to the stiffness terms, and the imaginary part is fitted to the damping terms:

$$\begin{aligned} \frac{Re\left(F_{\mathrm{u}}(K)\right)}{\frac{1}{2}\rho V^2 K^2} &= V^2 \left(a_1 + \sum_{l=1}^{N-3} a_{l+3} \frac{1}{\left(\left(d_l V\right)^2 + 1\right)} \right) \\ \frac{\mathrm{Im}\left(F_{\mathrm{u}}(K)\right)}{\frac{1}{2}\rho V^2 K^2} &= V \left(a_2 + \sum_{l=1}^{N-3} a_{l+3} \frac{d_l}{\left(\left(d_l V\right)^2 + 1\right)} \right) \end{aligned} \tag{4.30}$$

The RF is fitted to a complex force vector, which requires a nonlinear regression fitting procedure. An efficient numeric fitting approach for a quick and successful regression generally exists. First, the pole coefficients are chosen as $d_l \;\; l \in (1, 2, \dots, N-3)$, and the rest of the coefficients $a_i \;\; i \in (1, 2, \dots, N)$ are calculated with linear regression. Second, the nonlinear regression fit is used to find the optimal d_l, and linear regression is used to calculate a_i. Third, when an optimal set of d is found, nonlinear regression is used to find all the coefficients a_i and d_l, which allows a slight adjustment of all the curves. It is often helpful to start with QSS asymptotes and iterate from there.

The coefficients a_l differ, and the same d_l values are chosen for all DOFs. This method requires considering how to appropriately choose the starting values for the nonlinear regression scheme, and the convergence results should be monitored. It has a rather complex curve fit, and therefore, the automated procedure is rather challenging, particularly for scattered and limited reduced-frequency data.

Displacement convolution format

The rational function (4.28) has a transfer function that is defined as:

$$F_{\mathrm{se}}(\omega)=\frac{1}{2}\rho V^2\left(a_1+a_2 i\omega B/V+\sum_{l=1}^{N-3}a_{l+3}\frac{i\omega B/V}{i\omega B/V+d_l}\right) \tag{4.31}$$

This expression has an analytical IFT (4.20) solution in the following form:

$$I_{\mathrm{se}}(t)=\frac{1}{2}\rho V^2\left(a_1\delta(t)+a_2\frac{B}{V}\dot{\delta}(t)+\sum_{l=1}^{N-3}a_{l+3}\left(\delta(t)-\frac{d_l V}{B}e^{\left(-\frac{d_l V}{B}t\right)}\right)\right) \tag{4.32}$$

The time-domain force in Eq. (4.21) is calculated for the impulse response (4.32) as:

$$q_{\mathrm{se}}(t)=\frac{1}{2}\rho V^2\left(\underbrace{a_1u(t)+a_2\frac{B}{V}\dot{u}(t)+\sum_{l=1}^{N-3}a_{l+3}\left(u(t)-\frac{d_l V}{B}\right.}_{\text{Infinite contribution }(\infty)}\left.\underbrace{\int_{-\infty}^{t}e^{\left(-\frac{d_l V}{B}(t-\tau)\right)}u(\tau)\,d\tau}_{\text{Frequency variation }(\omega)}\right)\right) \tag{4.33}$$

The expression has coefficients related to the infinite contribution and results in constant values. The frequency contribution convolutes over the displacement response history. The infinite and frequency variation contributions are depicted in Figure 3-8.

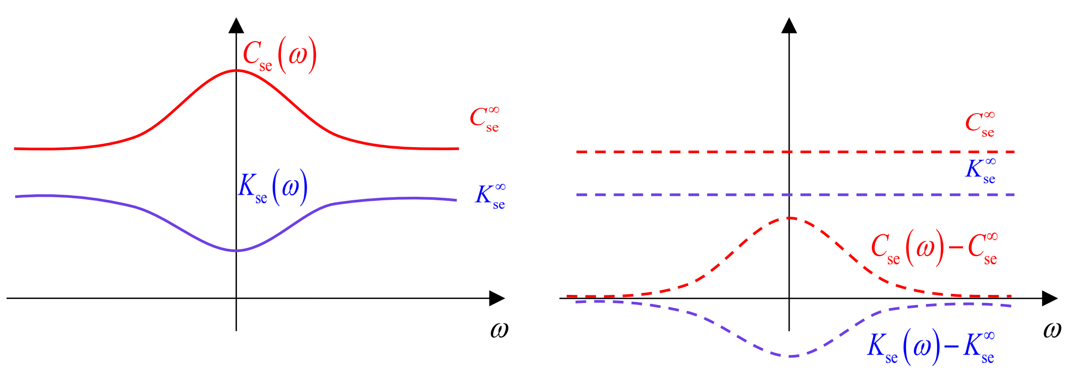

Figure 4-11: Aeroelastic damping and stiffness, and the infinite and frequency variation contributions.
Slika 4-11: Aeroelastično dušenje in togost, neskončni in frekvenčno odvisni prispevek.

Velocity convolution format

The transformation between (4.23) and (4.27) calculates the self-excited forces. The displacement transfer function format (4.31) of rational fit is expressed via (4.24) into a velocity transfer function format as:

$$H_{\mathrm{se}}(K)=\frac{1}{2}\rho V^{2}\left(a_{1}\frac{1}{i\omega}+a_{2}\frac{B}{V}+\sum_{l=1}^{N-3}a_{l+3}\frac{B/V}{i\omega B/V+d_{l}}\right) \tag{4.34}$$

The impulse response function is calculated with (4.26) as:

$$J_{\mathrm{se}}(t)=\frac{1}{2}\rho V^{2}\left(a_{1}+a_{2}\frac{B}{V}\delta(t)+\sum_{l=1}^{N-3}a_{l+3}\left(e^{\left(-\frac{d_{l}V}{B}t\right)}\right)\right) \tag{4.35}$$

The response is calculated with velocity convolution (4.27) as:

$$q_{\mathrm{se}}(t)=\frac{1}{2}\rho V^{2}\left(\underbrace{a_{1}u(t)+a_{2}\frac{B}{V}\dot{u}(t)}_{\text{Infinite contribution }(\infty)}+\sum_{l=1}^{N-3}a_{l+3}\left(\underbrace{\int_{0}^{t}e^{\left(-\frac{d_{l}V}{B}(t-\tau)\right)}\dot{u}(\tau)d\tau}_{\text{Frequency variation }(\omega)}\right)\right) \tag{4.36}$$

Equations (4.36) and (4.33) yield equivalent responses for the rational function fit. This outcome is related to the causal dynamic system property inherited in the parametrically fitted rational function. The presented alternative velocity convolution formulation may offer some advantages for the implementation of self-excited forces in various commercial software environments.

4.7 Nonparametric modeling of self-excited forces

A new novel approach to calculating the self-excited forces in the time domain is presented. It does not require the complex nonlinear regression fitting of causal dynamic systems. It offers further possibilities for the application of different freely chosen fitting functions, such as polynomial, spline, rational, and moving average interpolation functions, and is achieved by numerical evaluation via the IFT, an idea that is also applied to hydrodynamic wave radiation problems. The frequency-dependent transfer functions are numerically transformed into impulse response function (3.29) and then convoluted over the velocities (3.31). This procedure is not dependent on parametric fitted functions, allowing for an analytical mathematical transformation. The method is applied to independently fit the polynomial fitted stiffness and damping terms. The presented numerical convolution offers a faster computational algorithm compared to the convolution of RFs due to the required convolution operations. It is also attractive for implementation in commercial software without additional software extensions. Here, the MATLAB and *RM Bridge* code are investigated.

4.7.1 Theoretical background

The proposed numerical nonparametric model approach is designed for any continuous function fit. The transfer function can be split into frequency-dependent and constant contributions. A transfer function (4.24) suitable for velocity convolution is defined by:

$$H_{\mathrm{se}}(\omega) = H_{\mathrm{se}}^{\omega}(\omega) + H_{\mathrm{se}}^{\infty} \tag{4.37}$$

where the frequency contribution is

$$H_{\mathrm{se}}^{\omega}(\omega) = \left[C_{\mathrm{se}}(\omega) - C_{\mathrm{se}}^{\infty}\right] + \frac{1}{i\omega}\left[K_{\mathrm{se}}(\omega) - K_{\mathrm{se}}^{\infty}\right] \tag{4.38}$$

and the infinite contribution is

$$H_{\mathrm{se}}^{\infty}(\omega) = C_{\mathrm{se}}^{\infty} + \frac{1}{i\omega} K_{\mathrm{se}}^{\infty} \tag{4.39}$$

The infinite contribution has a straightforward analytical solution to the impulse response function:

$$J_{\mathrm{se}}^{\infty} = C_{\mathrm{se}}(\infty) + \delta(t) K_{\mathrm{se}}(\infty) \tag{4.40}$$

where $\delta(t)$ is the Dirac delta function. The frequency-dependent terms can be expressed in trigonometric form: $e^{i\omega t} = cos(\omega t) + i \cdot \sin(\omega t)$. The proposed transfer function can have general frequency-dependent numerical values and does not necessarily possess an analytical solution form. Therefore, the frequency-dependent part is resolved by a numerical Fourier transformation. The IFT (4.26) of the velocity transfer function (4.38) yields:

$$\begin{aligned} J_{\mathrm{se}}^{\omega}(t) &= \frac{1}{2\pi} \int_{-\infty}^{\infty} F_{\mathrm{se}}(\omega)\, e^{i\omega t} d\omega = \\ &\frac{1}{2\pi} \int_{-\infty}^{\infty} \left[C_{\mathrm{se}}(\omega) - C_{\mathrm{se}}^{\infty}\right]\left(\cos(\omega t) + i \cdot \sin(\omega t)\right) d\omega \\ &+ \frac{1}{2\pi} \int_{-\infty}^{\infty} \frac{1}{i\omega}\left[K_{\mathrm{se}}(\omega) - K_{\mathrm{se}}^{\infty}\right]\left(\cos(\omega t) + i \cdot \sin(\omega t)\right) d\omega \end{aligned} \tag{4.41}$$

The double-sided frequency spectrum can be expressed as a sum of negative and positive frequency spectrum values as:

$$\begin{aligned} J_{\mathrm{se}}^{\omega}(t) &= \frac{1}{2\pi} \int_{-\infty}^{0} \left(\left[C_{\mathrm{se}}(\omega) - C_{\mathrm{se}}^{\infty}\right] + \frac{1}{i\omega}\left[K_{\mathrm{se}}(\omega) - K_{\mathrm{se}}^{\infty}\right]\right)\left(\cos(\omega t) + i \cdot \sin(\omega t)\right) d\omega + \\ &+ \frac{1}{2\pi} \int_{0}^{\infty} \left(\left[C_{\mathrm{se}}(\omega) - C_{\mathrm{se}}^{\infty}\right] + \frac{1}{i\omega}\left[K_{\mathrm{se}}(\omega) - K_{\mathrm{se}}^{\infty}\right]\right)\left(\cos(\omega t) + i \cdot \sin(\omega t)\right) d\omega \end{aligned} \tag{4.42}$$

For linear causal time-invariant dynamic systems, the frequency-dependent spectrum is symmetric for the real and asymmetric imaginary parts. The transformation from a double-sided infinite spectrum into a single-sided infinite spectrum is as follows:

$$\begin{aligned} J_{\text{se}}^{\omega}(t) = & \frac{1}{2\pi}\int_0^\infty \left(\left[C_{\text{se}}(\omega) - C_{\text{se}}^\infty \right] - \frac{1}{i\omega}\left[K_{\text{se}}(\omega) - K_{\text{se}}^\infty \right] \right)\left(\cos(\omega t) + i \cdot \sin(\omega t) \right) d\omega + \\ & + \frac{1}{2\pi}\int_0^\infty \left(\left[C_{\text{se}}(\omega) - C_{\text{se}}^\infty \right] + \frac{1}{i\omega}\left[K_{\text{se}}(\omega) - K_{\text{se}}^\infty \right] \right)\left(\cos(\omega t) + i \cdot \sin(\omega t) \right) d\omega \end{aligned} \tag{4.43}$$

which can be simplified to:

$$J_{\text{se}}^{\omega}(t) = \frac{1}{\pi}\int_0^\infty \left[C_{\text{se}}(\omega) - C_{\text{se}}^\infty \right] \cos(\omega t)\, d\omega + \frac{1}{\pi}\int_0^\infty \frac{1}{\omega}\left[K_{\text{se}}(\omega) - K_{\text{se}}^\infty \right] \sin(\omega t)\, d\omega \tag{4.44}$$

An additional assumption is that the response is not present before the integration starts. In practice, the forces might not be correctly evaluated for the initial condition $q_{\text{se}}(t = 0)$. This temporary starting convolution effect usually diminishes quickly. (4.44) indicates that for negative values of time, the response $I_\omega(-t) = 0$ is equal to zero:

$$0 = \frac{1}{\pi}\int_0^\infty \left[C_{\text{se}}(\omega) - C_{\text{se}}^\infty \right] \cos(\omega(-t))\, d\omega + \frac{1}{\pi}\int_0^\infty \frac{1}{\omega}\left[K_{\text{se}}(\omega) - K_{\text{se}}^\infty \right] \sin(\omega(-t))\, d\omega \tag{4.45}$$

This also provides an important relation between the frequency-dependent data of $C_{\text{se}}(\omega)$ and $K_{\text{se}}(\omega)$:

$$\int_0^\infty \left(\left[C_{\text{se}}(\omega) - C_{\text{se}}^\infty \right] \cos(\omega t) \right) d\omega = \int_0^\infty \left(\frac{1}{\omega}\left[K_{\text{se}}(\omega) - K_{\text{se}}^\infty \right] \sin(\omega t) \right) d\omega \tag{4.46}$$

This relation is an interesting assumption that is further exploited in the published article. Exploring this relation opens up the possibility for new nonparametric flutter derivative fitting, where independent fitting of the real and imaginary parts is possible. Introducing relation (4.46) into equation (4.41) following the frequency-dependent Fourier transformation can yield:

$$J_{\text{se}}^{\omega}(t) = \frac{2}{\pi}\int_0^\infty \left[C_{\text{se}}(\omega) - C_{\text{se}}^\infty \right] \cos(\omega t)\, d\omega \tag{4.47}$$

Thus, joining the constant (4.40) and frequency-dependent (4.47) parts results in:

$$J_{\text{se}}(t) = J_{\text{se}}^{\infty}(t) + J_{\text{se}}^{\omega}(t) = K_{\text{se}}(\infty) + \delta(t) C_{\text{se}}(\infty) + \frac{2}{\pi}\int_0^\infty \left[C_{\text{se}}(\omega) - C_{\text{se}}^\infty \right] \cos(\omega t)\, d\omega \tag{4.48}$$

The application of flutter derivative aerodynamic normalization introduces fitting to reduce the velocity values. The numerator {*se, u*} represents the terms related to the displacement convolution, while the numerator {*se, v*} represents the velocity convolution terms.

Convolution of the impulse response function over the velocities with (4.27) yields:

$$q(t)=\frac{1}{2}\rho V^2\left(K_{\text{se,v}}^{\infty}u(t)+C_{\text{se,v}}^{\infty}\dot{u}(t)+\frac{2}{\pi}\int_0^t\int_0^{\infty}\left[C_{\text{se}}(\omega)-C_{\text{se,v}}^{\infty}\right]\cos\left(\omega(t-\tau)\right)\dot{u}(\tau)\,d\omega d\tau\right) \tag{4.49}$$

A similar derivation of the numerical Fourier transform can be performed for the convolution over the displacement. The transfer function of flutter derivatives (4.19) is split into constant and variation parts. The impulse response function is obtained by (4.20) and convoluted over the displacements (4.21). The reader can follow these steps, which lead to displacement numerical convolutions as:

$$q(t)=\frac{1}{2}\rho V^2\left(K_{\text{se,u}}^{\infty}u(t)+C_{\text{se,u}}^{\infty}\dot{u}(t)+\frac{2}{\pi}\int_0^t\int_0^{\infty}\left[K_{\text{se}}(\omega)-K_{\text{se,u}}^{\infty}\right]\cos\left(\omega(t-\tau)\right)u(\tau)\,d\omega d\tau\right) \tag{4.50}$$

4.7.2 Coefficient determination

Parametric modeling

The parametric model is used to validate the newly developed expression to ensure that the analytical and newly developed numerical convolution will deliver the same self-excited forces. Numerical tests are best performed on the parametric interpolation function of the rational function. The limit search determines the coefficients of the corresponding infinite and frequency contributions of the transfer function. The coefficients for the numerical velocity convolution expression (4.49) are as follows:

$$\begin{aligned}
K_{\text{se,v}}^{\infty}&=\lim_{\omega\to 0}\left(Im\left(H_{\text{se}}(\omega)\right)\cdot-\omega\right) &&\Rightarrow\quad a_1\\
C_{\text{se,v}}^{\infty}&=\lim_{\omega\to\infty}\left(Re\left(H_{\text{se}}(\omega)\right)\right) &&\Rightarrow\quad a_2\frac{B}{V}\\
\left[C_{\text{se}}(\omega)-C_{\text{se,v}}^{\infty}\right]&=Re\left(H_{\text{se}}(\omega)\right)-C_{\text{se,v}}^{\infty} &&\Rightarrow\quad \sum_{l=1}^{N-3}a_{l+3}\frac{B}{V}\frac{d_l}{K^2+d_l^2}
\end{aligned} \tag{4.51}$$

and are as follows for the displacement convolution expression (4.50):

$$\begin{aligned}
K_{\text{se,u}}^{\infty}&=\lim_{\omega\to\infty}\left(Re\left(F_{\text{se}}(\omega)\right)\right) &&\Rightarrow\quad a_1+\sum_{l=1}^{N-3}a_{l+3}\\
C_{\text{se,u}}^{\infty}&=\lim_{\omega\to\infty}\left(Im\left(F_{\text{se}}(\omega)\right)/\,\omega\right) &&\Rightarrow\quad a_2\frac{B}{V}\\
\left[K_{\text{se}}(\omega)-K_{\text{se,u}}^{\infty}\right]&=Re\left(F_{\text{se}}(\omega)/\,\omega\right)-K_{\text{se,u}}^{\infty} &&\Rightarrow\quad \sum_{l=1}^{N-3}a_{l+3}\frac{-d_l^2}{K^2+d_l^2}
\end{aligned} \tag{4.52}$$

Nonparametric modeling

The numerical Fourier transformation method allows the application of various interpolation techniques, such as independently fitted aeroelastic damping and stiffness curves. Coefficient extraction for higher-order polynomials is demonstrated, where the fit is divergent outside the available experimental data between ω_1 and ω_2. Extrapolation corrections are applied to ensure convergence to a constant infinite value plateau, thus satisfying the infinity convolution requirement. The following function ensures a smooth transition to a constant value before and after the experiment:

$$\begin{aligned} f(\omega) = {} & g(\omega_1)\left[1 - B(\omega - \omega_1)\right] \\ & + g(\omega)\left[B(\omega - \omega_1)\left(1 - B(\omega - \omega_2)\right)\right] \\ & + g(\omega_2)\left[B(\omega - \omega_2)\right] \end{aligned} \tag{4.53}$$

Here, $g(\omega)$ is the function used within the range of the experimental data, and $B(\omega)$ denotes the logistic function, which smooths the sharp transition around the cutoff frequency. The smooth function applied is the Heaviside unit step function, which is defined as follows:

$$B(\omega) = \frac{1}{1 - \exp\left(-2k(\omega - \omega_n)\right)} \tag{4.54}$$

Here, ω_n is the circular frequency in which the unit step function is activated, and a larger k corresponds to a sharper transition at ω_n. The infinite damping and stiffness values are simply chosen at the cutoff frequency. The described techniques can be applied well to the polynomial fit of the velocity convolution (4.49) by calculating the coefficients as:

$$\begin{aligned} K_{se,v}^{\infty} &= Im\left(H_{se}\left(\omega_1\right) \cdot -\omega_1\right) \\ C_{se,v}^{\infty} &= Re\left(H_{se}\left(\omega_2\right)\right) \\ \left[C_{se}\left(\omega\right) - C_{se,v}^{\infty}\right] &= Re\left(H_{se}\left(\omega\right)\right) - C_{se,v}^{\infty} \end{aligned} \tag{4.55}$$

and to the polynomial displacement convolution (4.50) by calculating the coefficients as:

$$\begin{aligned} K_{\mathrm{se,u}}^{\infty} &= Re\left(F_{\mathrm{se}}\left(\omega_2\right)\right) \\ C_{\mathrm{se,u}}^{\infty} &= Im\left(F_{\mathrm{se}}\left(\omega_2\right)\right) / \omega_2 \\ \left[K_{\mathrm{se}}\left(\omega\right) - K_{\mathrm{se,u}}^{\infty}\right] &= Re\left(F_{\mathrm{se}}\left(\omega\right) / \omega\right) - K_{\mathrm{se,u}}^{\infty} \end{aligned} \tag{4.56}$$

The proposed approach allows a more engineering-type approach to flutter simulations, eliminating the need to undertake complex parametric fitting procedures.

4.8 Algorithm validation

The presented self-excited models were tested numerically and experimentally in a wind tunnel laboratory [82]. The Hardanger bridge deck cross-section was tested at a scale of 1:50. Aeroelastic tests were performed for the following three DOFs: the lateral, vertical and torsional directions. First, the flutter derivatives were extracted with force vibration tests, providing individual flutter derivative points. The flutter derivatives were fitted with parametric rational function expression (4.28) and an individual polynomial fit, as shown in Figure 4-12 and Figure 4-13. The rational function complex value fit was calculated via a nonlinear regression algorithm [52]. The two $N=2$ poles provided a well-correlated and representative fit. For polynomials, a second-order fit provided reasonable accuracy.

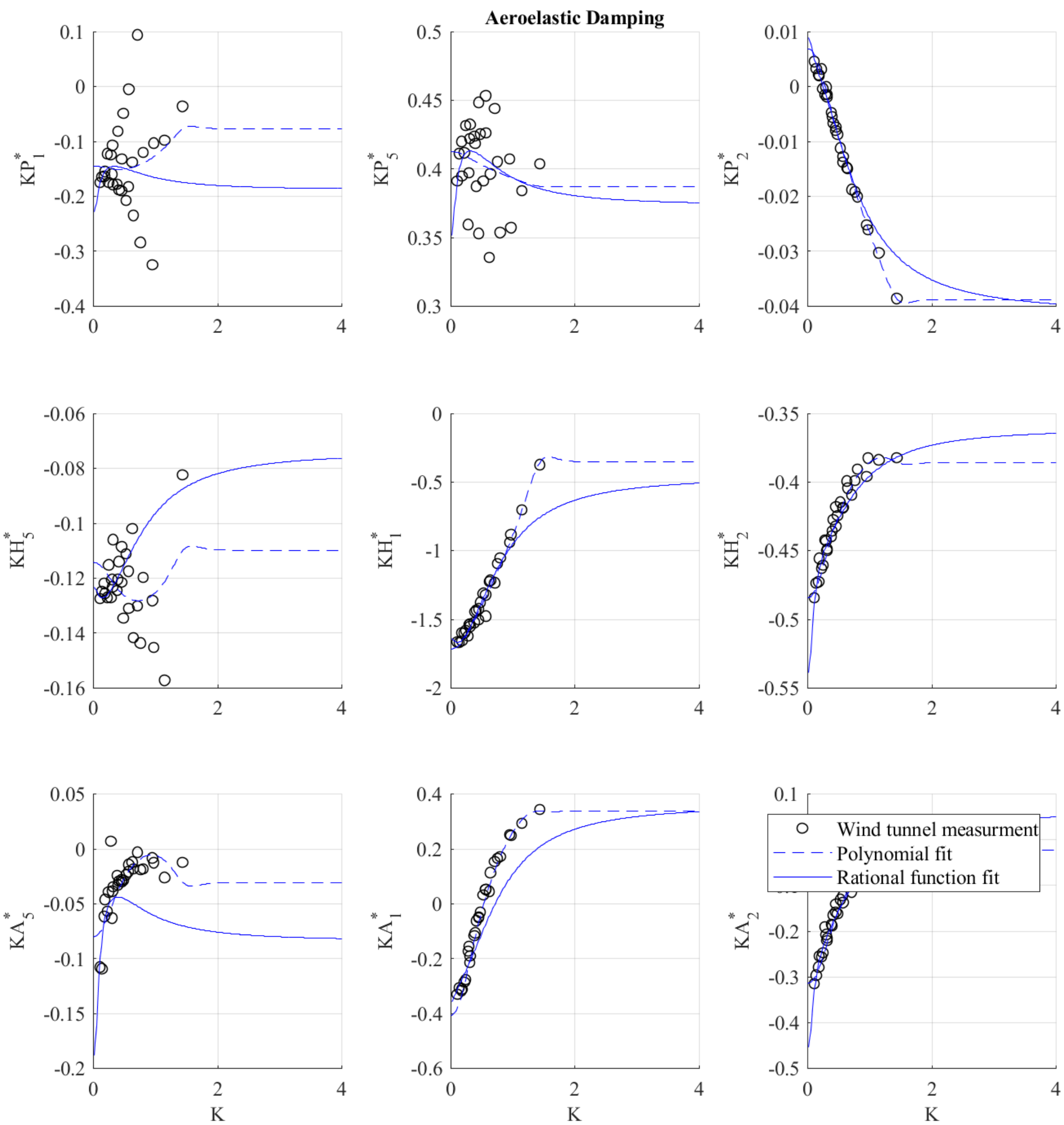

Figure 4-12: Fitting of the aeroelastic damping terms.

Slika 4-12: Interpolacija aeroelastičnega dušenja.

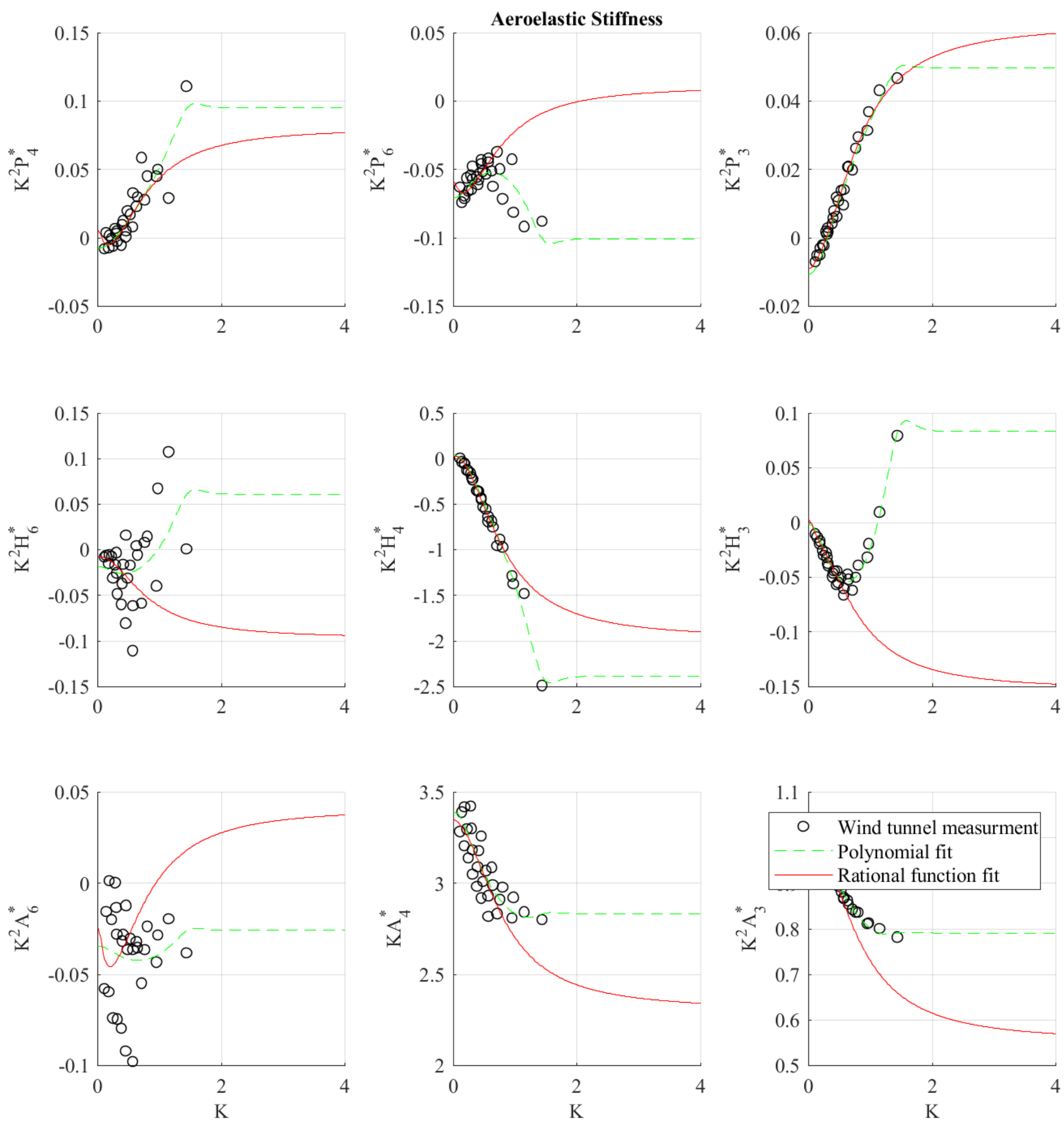

Figure 4-13: Fitting of the aeroelastic stiffness terms.

Slika 4-13: Interpolacija aeroelastične togosti.

In general, the torsional and vertical motion data are well correlated and provide very similar fits. The measured accuracy of the scattered lateral flutter derivatives can be compromised due to laboratory measurement inaccuracies or false linear model assumptions. The two different fitting techniques, i.e., the parametric and nonparametric fit, show some discrepancies for highly reduced frequencies and more scattered data. The second-order polynomial effectively captures all the flutter derivative trends, while the third-order polynomial is excellent for complex lateral motion trends. The two-pole rational function fit is satisfying and could be further improved by increasing the number of poles, thus leading to a minimal self-excited force improvement. Increasing the number of poles proportionally increases the number of calculations, while adding a higher polynomial has no effect on the calculation performance.

4.8.1 Numerical validation

The numerical validation compares the parametric fitted rational function inputs of the different self-excited models. The experimentally fitted parametric rational function on the flutter derivative data, depicted in Figure 4-12 and Figure 4-13, has an analytical solution. Analytically derived rational function expressions are presented for the displacement convolution $q_{\mathrm{se},1}$ in Eq. (4.33) and for the velocity convolution $q_{\mathrm{se},2}$ in Eq. (4.36). The explicit expression provides a literature reference for validation of the newly developed nonparametric numerical models. The numerical velocity convolution $q_{\mathrm{se},3}$ in Eq. (4.49) is determined by the rational function input presented in Eq. (4.51). The numerical displacement convolution $q_{\mathrm{se},4}$ in Eq. (4.50) is determined by the rational function input presented in Eq. (4.52). All the presented models are validated with 87 s of random motion, depicted in Figure 4-15. The 3-DOF tests of the four presented self-excited forces are depicted in Figure 4-14.

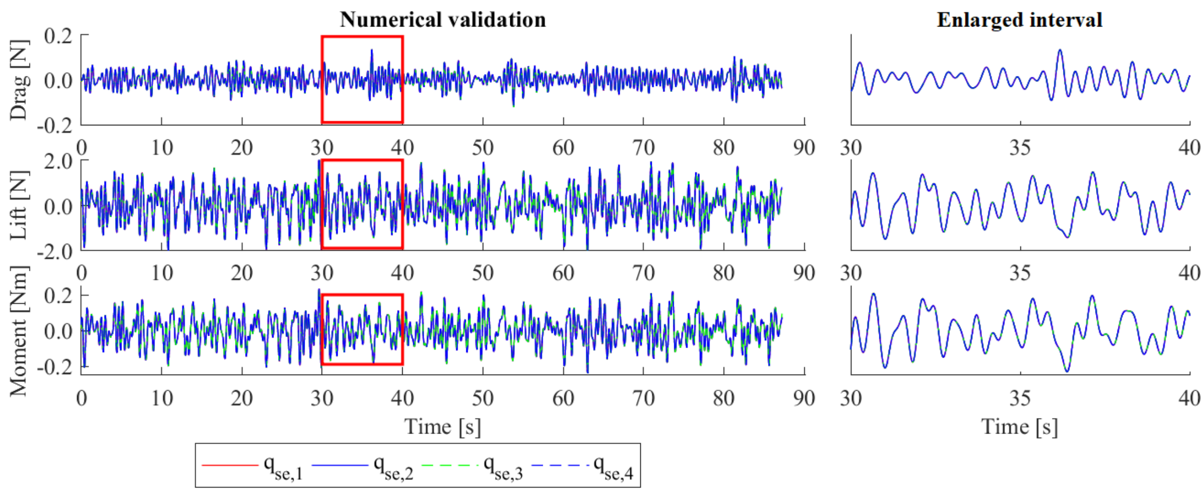

Figure 4-14: Self-excited force models for rational function input.

Slika 4-14: Različni numerični modeli aeroelastičnih sil.

Clearly, all self-excited models result in excellent overlap of the curves. Minor differences are observed for the first few seconds, which is expected due to the absence of motion information before time t=0. The well-matched curves confirm the correct implementation of the parametric and nonparametric numerical self-excited force models. During the development, several additional self-excited models were implemented that are not presented in this validation. The Scanlan model frequency superposition model superimposes individual harmonic components. The state space is an alternative calculation method based on applying the order reduction method of convolution into the matrix operation. The frequency-domain representation is made possible with a Fourier transformation of the displacement format in (4.17) and the velocity format (4.23). The additional variations were well tested during the stepwise implementation. All mentioned models result in well-matched self-excited forces, thus further confirming the correct implementation of all self-excited force models. The presented convolution integral models are therefore fully suited to represent the self-excited multiharmonic forces [70] [83] [84] [85].

4.8.2 Experimental validation

A multiharmonic 3-DOF motion test is performed in a wind tunnel rig. The measured forces are then compared to the developed numerical self-excited formulation models. The experimental motion is introduced by a synthetically generated signal as a superposition of randomly chosen amplitudes, frequencies and phases. The time histories have a constant rectangular frequency spectrum (16 mm, 16 mm, and 2.4°) between 0.25 and 2.5 Hz. One such realization is presented in Figure 4-15.

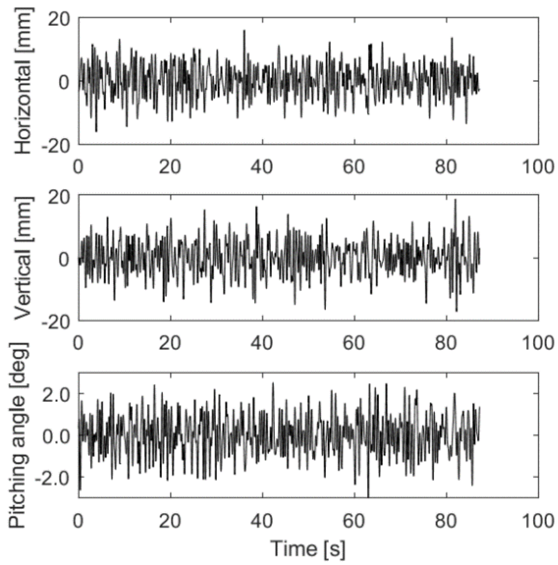

Figure 4-15: Random motion in three directions, i.e., horizontal, vertical and pitching motion, tested at 8 m/s.

Slika 4-15: Harmonični pomik horizontalno, vertikalno in torzijsko, testirani pri hitrosti vetra 8 m/s.

In the experimental test depicted in Figure 4-16, the parametric (rational function) and nonparametric (individual polynomial fit) models were compared. The polynomial damping interpolation convolutes over velocities in (4.49) and is determined by the coefficients in (4.55). The individual damping interpolation includes only the frequency contribution of the aeroelastic damping terms and does not relate to the frequency contribution of the aeroelastic stiffness. The polynomial stiffness interpolation convolutes over the displacements in (4.50) and is determined by the coefficients in (4.56). The rational function (4.33) uses nonlinear regression techniques, where the polynomial is simply fitted to individual aeroelastic damping and stiffness terms. The linear polynomial fitting represents a significant simplification in the fitting procedures, thus considerably simplifying the aeroelastic analysis.

The linear multiharmonic test indicates the accuracy of the harmonic linear assumption and compares the accuracies of the nonparametric numerical models. The experimental tests indicate that linear superposition supports the aerodynamic cross-sectional shape of the Hardanger Bridge, as evidenced by the good agreement between the experimentally measured forces and the numerical models regarding the lift and moment forces. The modeled drag force, however, strongly deviates from the measurements. The rather scattered lateral DOF flutter derivatives indicate possible false linear force identification. The drag force has a typical nonlinear multiharmonic force pattern and therefore cannot be simulated successfully with any of the presented linear models.

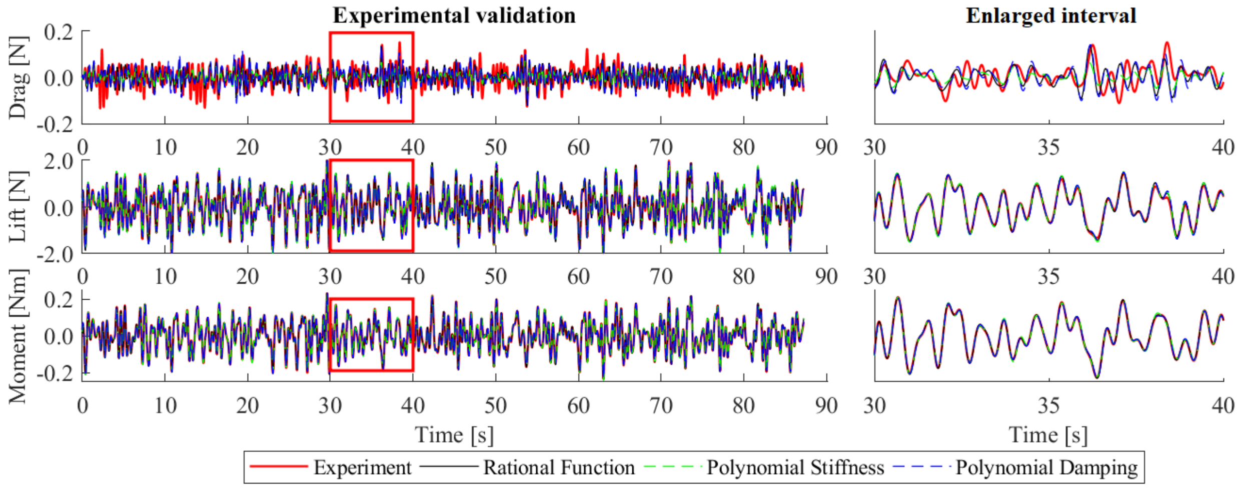

Figure 4-16: Parametric and nonparametric models.

Slika 4-16: Primerjava rezultatov parametričnih in neparametričnih interpolacij.

Additional extended testing is performed for 15 random motion realizations, the details of which are presented in the published paper. All tests confirm the suitability of the presented parametric and nonparametric models. Thus, we can conclude that the mathematically derived relation between aeroelastic damping and aeroelastic stiffness in Eq. (4.46) holds. This relation results in the nonparametric models providing accurate results in the presented tests and being well suited to simulate the Hardanger cross-section self-excited forces. The causal dynamic system relation is automatically satisfied without the need for a nonlinear complex parametric fitting of the transfer functions. Clearly, the lateral flutter derivatives have a lower confidence level due to the data being more scattered. More scattered flutter derivative data can also be expected for various cross-sections, such as open box girders, I-beams, and T-beams. This scenario could lead to a possible discrepancy between the aeroelastic damping and stiffness contributions. Here, the nonparametric model offers an individual fitting to either the damping or stiffness terms, which are selected based on the engineering judgment of the aeroelastic damping and stiffness measurement quality. In wind tunnel experiments, the measured damping terms are typically more trustworthy than the stiffness terms of sectional forces. The presented numerical convolutional models offer the ability to choose the type of fit, individual damping, individual stiffness only or a parametric interpolated result. Nonparametric models provide much needed simplification compared to a complex parametric self-excited force model.

4.8.3 Software validation

A comprehensive overview of the literature commonly applied for self-excited models is provided. Various alternatives of self-excited models are presented, providing different possibilities for a time-domain implementation. This research focuses on well-tested parametric models and provides newly developed nonparametric self-excited models. Reformulation of the well-known rational function expression into the numerical convolution calculation makes these models the best candidates for a possible bridge industry application. Over the past few years, several fully coupled time-domain models of wind-wave-bridge interactions have been developed. Due to the complex modeling requirements, commercial codes are commonly applied in bridge response calculations. Different time-domain solutions have different input possibilities and can be somewhat limited to self-excited modeling possibilities. Suitable candidates for floating bridge analysis and design will have to incorporate the linear wave radiation solution. Several candidates that fulfill the needed hydrodynamic functionality have been identified, as follows: *RM Bridge*, *OrcaFlex, SOFiSTiK*, and *Ansys*. These solutions can potentioally implement the numerical velocity convolution self-excited models presented in this work, allowing the incorporation of the self-excited forces or replacement of the less accurate QSS aerodynamic matrices. To date, this task has been challenging, and aeroelastic analysis is commonly performed as a separate investigation. In this work, suggested extensions are implemented in the software, thus resolving fully coupled floating bridge dynamics. A single node with three DOFs is demonstrated in Figure 4-17.

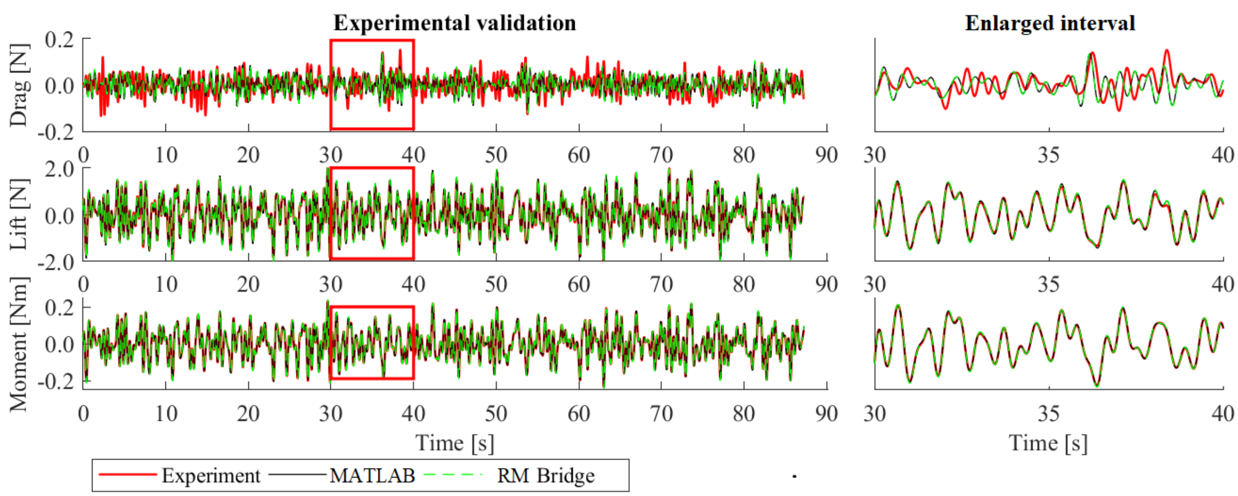

Figure 4-17: Software validation in the MATLAB and RM Bridge programs.

Slika 4-17: Aeroelastični numerični modeli, sprogramirani v programih MATLAB in RM Bridge.

The models agree well with the *MATLAB* implementation and follow the wind tunnel measurement. The frequency-dependent tables are imported into the convolution over the velocity calculations. With the same interface as that used for hydrodynamic wave radiation damping, self-excited forces are now simulated within the *RM Bridge* software environment. The aeroelastic damping tables in Eq. (4.51) are applied in the hydrodynamic convolution nodal load interface. The wind nodes are assigned to the structural deck nodes, where those effects are observed on the structure. As a result, engineers can introduce self-excited models for the design of floating bridges. Furthermore, the various nonparametric models can considerably simplify the aeroelastic design process without a loss in accuracy.

5 FREQUENCY-DOMAIN ANALYSIS

5.1 Preview

Modal decomposition techniques are frequently used in every engineering discipline and are commonly applied in bridge design. They are strong supplemental tools in addition to time-domain methods, providing important insight into the structural response. The structural response is represented for the most relevant structural frequencies, masses, and corresponding deformation shapes. The method results are easy to understand, and no special response postprocessing is required. Frequency-domain methods are considerably computationally more efficient than time-domain analysis. The different modal results can be merged with a combination rule, providing an overview of the bridge response. The structural response is mathematically described in uncoupled generalized coordinates, and coupled environmental loads are added.

This chapter provides a brief overview of a linear modal decomposition method referred to as frequency-domain analysis. The presented method is used to validate and compare the time-domain models applied to the floating bridge example. An additional explanation of the environmental load formulation and a corresponding introduction to the floating bridge dynamic equation of motion are provided.

5.2 Modal decomposition

The global assembled structural matrices are uncoupled by eigenvalue analysis and form equivalent modal structural properties. The additional global environmental loads are time-dependent loads and are transformed into a frequency-domain representation. The self-excited loads can be expressed by adding additional frequency-dependent matrices, altering the structural properties. The additional environmental matrices are coupled and prevent standard mode-by-mode decomposition. Therefore, the dynamic system has to be analyzed in two steps. First, the dynamic properties of the structure and hydrodynamic masses must be uncoupled into a generalized coordinate system. Second, various coupled loads on the small generalized coordinates must be considered. The dynamic equation of motion for a global structural nonlinear system is as follows:

$$\mathbf{M}\ddot{\mathbf{u}}(t)+\mathbf{C}(t)\dot{\mathbf{u}}(t)+\mathbf{K}(t)\mathbf{u}(t)=\mathbf{F}_{\text{load}}(t,\ddot{u},\dot{u},u) \tag{5.1}$$

where $\mathbf{M},\mathbf{C},\mathbf{K}$ are equivalent global matrices of the mass, damping and nonlinear structural stiffness, respectively. Different environmental loads $\mathbf{F}_{\text{load}}(t,\ddot{u},\dot{u},u)$ are added stepwise to the calculation procedure. The initial nonlinear structural system is determined by permanent loads such as the self-weighted loads $\mathbf{F}_{\text{sw}}$, prestressing of the cable initial geometry $\mathbf{F}_{\text{cable}}$, mean wind $\mathbf{F}_{\text{mean}}$, and mean current load $\mathbf{F}_{\text{curr}}$. The system is linearized around the tangential stiffness, which consists of the linear structural stiffness and higher-order geometrical nonlinear stiffness.

The nonlinear geometrical stiffness is a result of nonlinear deformations under the influence of permanent static loads and is calculated with the Newton-Raphson iterative algorithm:

$$\mathbf{M}\ddot{\mathbf{u}}(t)+\mathbf{C}\dot{\mathbf{u}}(t)+\mathbf{K}_{\mathrm{nl}}\mathbf{u}(t)=\mathbf{F}_{\mathrm{sw}}+\mathbf{F}_{\mathrm{cable}}+\mathbf{F}_{\mathrm{mean}}+\mathbf{F}_{\mathrm{curr}} \tag{5.2}$$

where $\mathbf{K}_{\mathrm{nl}}$ represents the linearized tangential stiffness matrix of permanent loads, introducing the approximation of linearized nonlinear systems. Since the added masses participate much more in the hydrodynamic interaction compared to the structural mass, the modal shapes are expected to be strongly alterable. Therefore, the hydrodynamically added masses and hydrodynamic plane stiffness are added to the frequency decomposition procedure, forming the global dynamic equation of motion, as follows:

$$\left(\mathbf{M}+\mathbf{M}_{\mathrm{hy}}(\omega)\right)\ddot{\mathbf{u}}(t)+\mathbf{C}\dot{\mathbf{u}}(t)+\left(\mathbf{K}_{\mathrm{nl}}+\mathbf{K}_{\mathrm{hy}}\right)\mathbf{u}(t)=\mathbf{F}_{\mathrm{perm}} \tag{5.3}$$

This dynamic system can be solved by eigenvalue decomposition. Here, ω is an eigenvalue, and $\boldsymbol{\phi}$ is the modal shape. Accounting for additional hydrodynamic added mass, the eigenvalue analysis equation is formulated as:

$$\left[\left(\mathbf{K}_{\mathrm{nl}}+\mathbf{K}_{\mathrm{hy}}\right)-\omega^2\left(\mathbf{M}+\mathbf{M}_{\mathrm{hy}}(\omega)\right)\mathbf{u}(t)\right]\boldsymbol{\phi}=0 \tag{5.4}$$

Here, the damping is assumed to have a negligible effect on the frequencies. The representative equivalent modal response relative to the global response can be expressed in generalized coordinates as:

$$\begin{aligned}
&\mathbf{u}(x,t)=\boldsymbol{\phi}(x)\boldsymbol{\eta}(t)\\
&\boldsymbol{\phi}(x)=\left[\boldsymbol{\varphi}_1 \quad \cdots \quad \boldsymbol{\varphi}_i \quad \cdots \quad \boldsymbol{\varphi}_{\mathrm{N\ mode}}\right]\\
&\boldsymbol{\eta}(t)=\left[\eta_1 \quad \cdots \quad \eta_i \quad \cdots \quad \eta_{\mathrm{N\ mode}}\right]^{\mathrm{T}}\\
&\boldsymbol{\varphi}_i=\left[\phi_{\mathrm{y}} \quad \phi_{\mathrm{z}} \quad \phi_{\mathrm{rx}}\right]^{\mathrm{T}}
\end{aligned} \tag{5.5}$$

Eq. (5.4) contains real value vectors that are the result of the uncoupled global system in Eq. (5.3) . This decomposition is made possible with some commonly available commercial codes. The eigenanalysis software should have available functionality to model nonlinear geometrical bridge stiffness and allow for symmetric 6×6 fully correlated mass matrix definitions. Here, the developed calculation approach resolves the individual frequency-by-frequency mode as a set of independent calculations [86], requiring an external algorithm to run a series of eigenanalyses with manipulation of the added masses. The externally running algorithm runs a commercial code to calculate the frequency, masses and modal shapes. The convergences and iteration of each mode are controlled. Good convergence is made possible by selecting the infinite hydrodynamic mass $\mathbf{M}_{\mathrm{hy}}(\infty)$ as an initial starting point, from which the frequency variation $\mathbf{M}_{\mathrm{hy}}(\omega)$ is adjusted through convergence of the eigenfrequencies. A procedure allowing the modal decomposition of the frequency-dependent structural properties is presented herein. The hydrodynamic added mass approaches a constant value above 1.5 rad/s, which allows for the calculation of higher spectrum modes with constant $\mathbf{M}_{\mathrm{hy}}(\infty)$. The lower spectrum of eigenfrequencies requires an iterative algorithm to consider the hydrodynamic mass variation $\mathbf{M}_{\mathrm{hy}}(\omega)$. The iterative solution starts with the lowest frequency and progresses to higher frequencies, as presented in the numerical algorithm depicted in Figure 5-1.

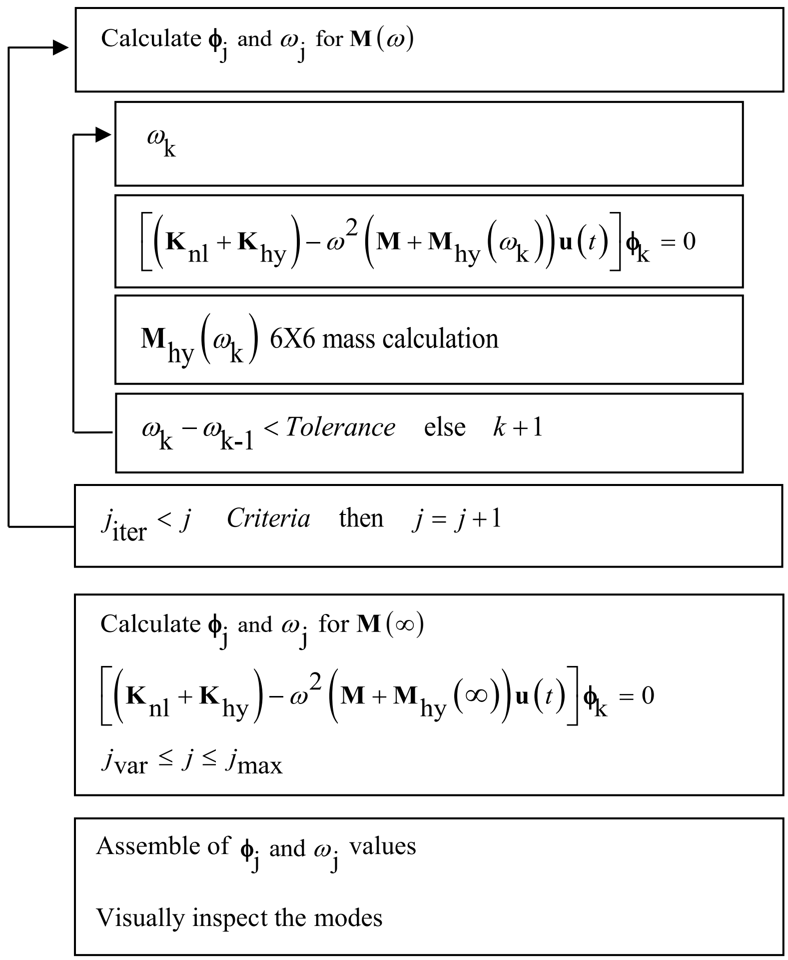

Figure 5-1: The iterative scheme used for the eigensolution for a frequency-dependent mass.

Slika 5-1: Iterativna shema reševanja problema lastnih vrednosti, kjer nastopa frekvenčno odvisna masa.

The convergence is monitored for possible frequency shifts and sudden changes in the modal shape. The external algorithm controls the stepwise iteration and convergence of each eigenmode. Due to the possible relatively large participation of frequency-dependent hydrodynamic masses, the possibility of a modal shift exists. These phenomena can be investigated by comparing the evolution of modes and visual inspection of the modal shapes [86].

5.3 Environmental loads

After the first step of modal decomposition, the additional environmental loads are added to the decomposed system in the generalized coordinate system. The added loads are unsymmetrical coupled loads and cannot be resolved by using the classic real eigenvalue techniques. A complex-eigenvalue analysis procedure allowing the introduction of self-excited and time-dependent loads is discussed herein. The presented mathematical derivation is suitable to calculate the complex coupled environmental response, with a similar approach being commonly applied in the aeroelastic instability analysis of bridges. On the left side of the dynamic equation, the frequency-dependent self-excited loads, hydrodynamic damping loads, current loads and structural damping are included. On the right side of the dynamic equation, time-dependent environmental loads, such as wind buffeting and wave loads, are introduced. Adding additional environmental loads to Eq. (5.3) yields the following global equation of motion:

$$\mathbf{M}_{\mathrm{s+hy}}\ddot{\mathbf{u}}(t)+\left(\mathbf{C}_{\mathrm{s}}-\mathbf{C}_{\mathrm{curr}}-\mathbf{C}_{\mathrm{hy}}(\omega)-\mathbf{C}_{\mathrm{se}}(\omega)\right)\dot{\mathbf{u}}(t)+\left(\mathbf{K}_{\mathrm{nl+hy}}-\mathbf{K}_{\mathrm{se}}(\omega)\right)\mathbf{u}(t)=\mathbf{F}_{\mathrm{env}}(t) \tag{5.6}$$

where the modal analysis results in Eq. (5.4) incorporates the effect of the frequency-dependent mass in the $\mathbf{M}_{\mathrm{s+hy}}$ term and the tangent stiffness and hydrodynamic plane stiffness in the $\mathbf{K}_{\mathrm{nl+hy}}$ term. The current VDD is a nonlinear load that can be approximated by the linearized value around the mean current velocity of the static component $\mathbf{F}_{\mathrm{cur}}$. The tangent damping approximation can be a reasonable simplification for practical applications due to its limited participation in the first few lateral modes. Eq. (5.6) can be rewritten into a generalized mode by substituting $\mathbf{u}=\phi\eta$ as:

$$\mathbf{M}_{\mathrm{s+hy}}\boldsymbol{\phi}\ddot{\boldsymbol{\eta}}+\left(\mathbf{C}_{\mathrm{s}}-\mathbf{C}_{\mathrm{cur}}-\mathbf{C}_{\mathrm{hy}}(\omega)-\mathbf{C}_{\mathrm{se}}(\omega)\right)\boldsymbol{\phi}\dot{\boldsymbol{\eta}}+\left(\mathbf{K}_{\mathrm{nl+hy}}-\mathbf{K}_{\mathrm{se}}(\omega)\right)\boldsymbol{\phi}\boldsymbol{\eta}=\mathbf{F}_{\mathrm{env}}(t) \tag{5.7}$$

where ϕ is the reduced modal matrix for the set of eigenvectors and presents each eigenmode. Multiplying (5.7) by ϕ^{T} yields:

$$\boldsymbol{\phi}^{\mathrm{T}}\mathbf{M}_{\mathrm{s+hy}}\boldsymbol{\phi}\ddot{\boldsymbol{\eta}}+\boldsymbol{\phi}^{\mathrm{T}}\left(\mathbf{C}_{\mathrm{s}}-\mathbf{C}_{\mathrm{curr}}-\mathbf{C}_{\mathrm{hy}}(\omega)-\mathbf{C}_{\mathrm{se}}(\omega)\right)\boldsymbol{\phi}\dot{\boldsymbol{\eta}}+\boldsymbol{\phi}^{\mathrm{T}}\left(\mathbf{K}_{\mathrm{nl+hy}}-\mathbf{K}_{\mathrm{se}}(\omega)\right)\boldsymbol{\phi}\boldsymbol{\eta}=\boldsymbol{\phi}^{\mathrm{T}}\mathbf{F}_{\mathrm{env}} \tag{5.8}$$

The equations can be rewritten in simplified form as:

$$\tilde{\mathbf{M}}_0\ddot{\boldsymbol{\eta}}+\mathbf{C}_{\mathrm{R}}\boldsymbol{\eta}+\mathbf{K}_{\mathrm{R}}\dot{\boldsymbol{\eta}}=\boldsymbol{\phi}^{\mathrm{T}}\mathbf{F}_{\mathrm{env}} \tag{5.9}$$

where the residual damping and stiffness are defined by:

$$\begin{aligned}\mathbf{C}_{\mathrm{R}}&=\tilde{\mathbf{C}}_0-\tilde{\mathbf{C}}_{\mathrm{cur}}-\tilde{\mathbf{C}}_{\mathrm{hy}}-\tilde{\mathbf{C}}_{\mathrm{se}}\\ \mathbf{K}_{\mathrm{R}}&=\tilde{\mathbf{K}}_0-\tilde{\mathbf{K}}_{\mathrm{se}}\end{aligned} \tag{5.10}$$

The modal matrix notation $\sim$ can be written in an integral form suitable for finite element implementation, with the dynamic structural properties expressed as:

$$\begin{aligned}\tilde{\mathbf{M}}_{0,\mathrm{nn}}&=\int_L\left(\boldsymbol{\phi}_{\mathrm{n}}^{\mathrm{T}}\mathbf{m}_{\mathrm{s+hy}}\boldsymbol{\phi}_{\mathrm{n}}\right)dl\\ \tilde{\mathbf{C}}_{0,\mathrm{nn}}&=2\xi_{\mathrm{n}}\omega_{\mathrm{n}}\tilde{\mathbf{M}}_0\\ \tilde{\mathbf{K}}_{0,\mathrm{nn}}&=\omega_{\mathrm{n}}^2\tilde{\mathbf{M}}_0\end{aligned} \tag{5.11}$$

where $\tilde{\mathbf{M}}_0$ is the modal mass matrix, $\tilde{\mathbf{C}}_0$ is the modal damping, $\tilde{\mathbf{K}}_0$ is the modal stiffness, ξ_n is the structural logarithmic modal damping, ω_n are natural frequencies, and n is the number of modes. All structural matrices are diagonal and have zero off-diagonal terms. Different environmental loads, presented for different vector sizes, are assembled in generalized coordinates as:

$$
\begin{aligned}
&\underset{1\times1}{\tilde{\mathbf{C}}_{\mathrm{hy,nm}}}(\omega)=\sum_{n=1}^{\mathrm{Npon}}\left(\underset{6\times1}{\boldsymbol{\varphi}_{\mathrm{n}}^{\mathrm{T}}}\,\underset{6\times6}{\mathbf{C}_{\mathrm{hy}}}(\omega)\,\underset{1\times6}{\boldsymbol{\varphi}_{n}}\right)\\
&\underset{1\times1}{\tilde{\mathbf{C}}_{\mathrm{cur,nn}}}(V_{\mathrm{cur}})=\int_L\left(\underset{2\times1}{\boldsymbol{\varphi}_{\mathrm{n}}^{\mathrm{T}}}\,\underset{2\times2}{\mathbf{C}_{\mathrm{cur}}}(V_{\mathrm{cur}})\,\underset{1\times2}{\boldsymbol{\varphi}_{\mathrm{m}}}\right)dl\\
&\underset{1\times1}{\tilde{\mathbf{C}}_{\mathrm{se,nm}}}(V_{\mathrm{mean}},\omega)=\int_L\left(\underset{3\times1}{\boldsymbol{\varphi}_{\mathrm{n}}^{\mathrm{T}}}\,\underset{3\times3}{\mathbf{C}_{\mathrm{ae}}}(V,\omega)\,\underset{1\times3}{\boldsymbol{\varphi}_{\mathrm{m}}}\right)dl\\
&\underset{1\times1}{\tilde{\mathbf{K}}_{\mathrm{se,nm}}}(V_{\mathrm{mean}},\omega)=\int_L\left(\underset{3\times1}{\boldsymbol{\varphi}_{\mathrm{n}}^{\mathrm{T}}}\,\underset{3\times3}{\mathbf{K}_{\mathrm{ae}}}(V,\omega)\,\underset{1\times3}{\boldsymbol{\varphi}_{\mathrm{m}}}\right)dl
\end{aligned}
\tag{5.12}
$$

The wind self-excited and VDD loads are commonly modeled with the linear load distribution assumption. Hydrodynamic damping is modeled for the discrete hydrodynamic nodes of pontoons, representing a nonsymmetrical frequency-dependent matrix. The linearized current damping is a diagonal matrix without any off-diagonal terms. The structural damping, masses and stiffnesses constitute diagonal matrices as a result of modal decomposition.

For any periodic and aperiodic motion, the Fourier integral representation $\eta=\eta_0 e^{i\omega t}$ is applied to the motion and to the time-dependent forces:

$$\left[-\omega^2\tilde{\mathbf{M}}_0+i\omega\mathbf{C}_{\mathrm{R}}+\mathbf{K}_{\mathrm{R}}\right]\boldsymbol{\eta}_0 e^{i\omega t}=\boldsymbol{\phi}^{\mathrm{T}}\mathbf{F}_{\mathrm{env}}(t)e^{i\omega t} \tag{5.13}$$

Applying Fourier integration over the investigated frequency range yields:

$$\left[\left(\mathbf{K}_{\mathrm{R}}-\omega^2\tilde{\mathbf{M}}_0\right)+i\omega\mathbf{C}_{\mathrm{R}}\right]\int_{-\infty}^{\infty}\boldsymbol{\eta}_0 e^{i\omega t}=\boldsymbol{\phi}^{\mathrm{T}}\int_{-\infty}^{\infty}\mathbf{F}_{\mathrm{env}}(t)e^{i\omega t} \tag{5.14}$$

The frequency-domain representation of the structural response, similar to the wind self-excitation calculation in Eq. (4.17), is defined as:

$$\mathbf{G}_{\mathrm{q}}(\omega)=\mathbf{F}_{\mathrm{env}}(\omega)\mathbf{G}_{\mathrm{u}}(\omega) \tag{5.15}$$

where $\mathbf{F}_{\mathrm{env}}$ is the transfer function matrix of environmental forces, $\mathbf{G}_{\mathrm{u}}$ is the Fourier transform of the displacements and $\mathbf{G}_{\mathrm{q}}$ is the Fourier transform of the forces. The environmental loads are calculated as:

$$\mathbf{G}_{\mathrm{q}}=\left[\left(\mathbf{K}_{\mathrm{R}}-\omega^2\tilde{\mathbf{M}}_0\right)+i\omega\mathbf{C}_{\mathrm{R}}\right]\mathbf{G}_{\mathrm{u}} \tag{5.16}$$

The goal is to calculate the structural displacement; therefore, the displacements in Eq. (5.15) are expressed as:

$$\mathbf{G}_{\mathrm{u}}=\mathbf{H}_{\mathrm{env}}\mathbf{G}_{\mathrm{q}} \tag{5.17}$$

where the impedance matrix is calculated as the inverse of the transfer function:

$$\mathbf{H}_{\mathrm{env}}(V_{\mathrm{mean}},V_{\mathrm{cur}},\omega)=\left[\left(\mathbf{K}_{\mathrm{R}}-\omega^2\tilde{\mathbf{M}}_0\right)+i\omega\mathbf{C}_{\mathrm{R}}\right]^{-1} \tag{5.18}$$

Each term of the impedance matrix $\mathbf{H}_{\mathrm{env}}(\omega)_{\mathrm{ij}}$ presents an amplitude and phase response of the structure as a function of the frequency ω and mode j. One can rewrite the impedance matrix in the well-known nondimensional form $\widehat{\mathbf{H}}_{\mathrm{env}}$ by dividing (5.17) by $\widetilde{\mathbf{K}}_0 = \omega_n^2 \widetilde{\mathbf{M}}_0$:

$$\hat{\mathbf{H}}_{\mathrm{env}}\left(V,\omega\right)=\left[-\frac{\omega^2}{\omega_{\mathrm{n}}^2}+2i\frac{\mathbf{C}_{\mathrm{R}}\tilde{\mathbf{M}}_0^{-1}}{2\omega_{\mathrm{n}}}\left(\frac{\omega}{\omega_{\mathrm{n}}}\right)+\frac{\mathbf{K}_{\mathrm{R}}\tilde{\mathbf{M}}_0^{-1}}{\omega_{\mathrm{n}}^2}\right]^{-1} \tag{5.19}$$

5.4 Structural stability

Global dynamic stability is an important aspect of a safe long-span bridge design. The commonly used linear flutter derivatives can be applied to describe the self-excited wind forces. The dynamic instability of flutter causes undamped oscillations at the central wind speed, resulting in permanent damage to or collapse of the bridge. Several modes can contribute to the flutter and can be analyzed with a multimodal coupled flutter formulation. Multimodal flutter methods have been extended for various environmental loads, such as hydrodynamic wave radiation, VDD and aeroelastic self-excited forces. Two deterministic methods are briefly described based on an eigenvalue analysis of the dynamic equation of a floating bridge in Eq. (5.8).

The first method analyzes the instability of a structure by analyzing the impedance matrix $\mathbf{H}_{\mathrm{env}}$. The selected variable for the calculation of instability is the mean wind speed influencing the aeroelastic flutter derivative contribution. The determinate calculation of the independent matrix $\left|\det\left(\mathbf{H}(V_{\mathrm{mean}})\right)\right| = 0$ provides the critical flutter wind speed. The mean wind speed is increased stepwise until instability is achieved. The advantage of this method is its direct application to Eq. (5.18) without the need to perform a complex-eigenvalue analysis. The approach requires a sufficiently small frequency discretization and wind speed discretization, which presents a computational challenge. The recommendation is to use visual inspection and the plotted impendence matrix as a function of the frequency and wind speed to confirm possible instability.

The second alternative is to resolve the coupled mode dynamic system in generalized coordinates by complex conjugate eigenvalue analyses [69] [87] [88] [89]. The aeroelastic self-excited and hydrodynamic wave radiation forces are nonsymmetric and frequency dependent; therefore, the classic eigenvalue procedure cannot be applied. An iterative nonlinear calculation scheme is required to consider changes in the aeroelastic damping and stiffness. Mathematical packages are also available, such as MATLAB, to resolve the nonlinear eigenvalue problem. Convergence tolerance is commonly resolved within a few iterations. The complex-eigenvalue problem can be formulated as:

$$\left[\mu\begin{pmatrix}\mathbf{I} & 0\\ 0 & \mathbf{I}\end{pmatrix}\begin{pmatrix}\mu^2\mathbf{w}\\ \mu\mathbf{w}\end{pmatrix}+\begin{pmatrix}\mathbf{C}_{\mathrm{R}} & \mathbf{K}_{\mathrm{R}}\\ -\mathbf{I} & 0\end{pmatrix}\begin{pmatrix}\mu\mathbf{w}\\ \mathbf{w}\end{pmatrix}\right]e^{\mu t}=0 \tag{5.20}$$

The eigensolution has $2N$ pairs of complex conjugate eigenvalues $\mu = (\mu\mathbf{w}\ \mathbf{w})$. The real part presents the frequency of oscillation, and the imaginary part presents the modified structural dynamics, as depicted in Figure 5-2. Once damping becomes negative, unstable fluttering occurs.

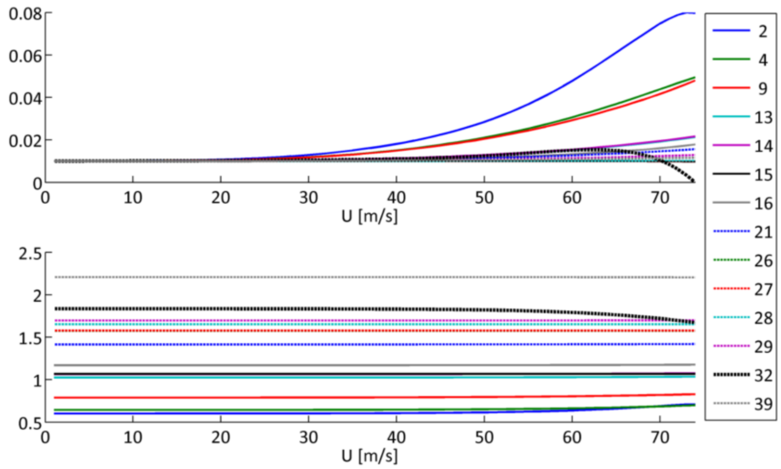

Figure 5-2: Multimodal flutter instability analysis. The upper diagram presents critical damping, and the lower diagram presents the frequencies per vibration mode [90].

Slika 5-2: Modalna aeroelastična stabilnostna analiza, zgoraj prikaz dušenja in spodaj prikaz frekvenc [90].

5.5 Structural response under wind loads

A dynamic response analysis of wind buffeting in the frequency domain that is suitable for correlated multimodal responses is presented herein. The proposed equations can be applied to calculate the floating bridge response under central turbulent wind events. For this analysis, the modal load vector is defined as:

$$\begin{aligned}\boldsymbol{\varphi}(x_\mathrm{r}) &= \begin{bmatrix} \boldsymbol{\varphi}_1(x_\mathrm{r}) & \cdots & \boldsymbol{\varphi}_i(x_\mathrm{r}) & \cdots & \boldsymbol{\varphi}_\mathrm{M}(x_\mathrm{r}) \end{bmatrix} \\ &= \begin{bmatrix} \begin{bmatrix} \phi_\mathrm{y}(x_\mathrm{r}) \\ \phi_\mathrm{z}(x_\mathrm{r}) \\ \phi_\mathrm{rx}(x_\mathrm{r}) \end{bmatrix}_1 & \cdots & \begin{bmatrix} \phi_\mathrm{y}(x_\mathrm{r}) \\ \phi_\mathrm{z}(x_\mathrm{r}) \\ \phi_\mathrm{rx}(x_\mathrm{r}) \end{bmatrix}_i & \cdots & \begin{bmatrix} \phi_\mathrm{y}(x_\mathrm{r}) \\ \phi_\mathrm{z}(x_\mathrm{r}) \\ \phi_\mathrm{rx}(x_\mathrm{r}) \end{bmatrix}_\mathrm{M} \end{bmatrix}\end{aligned} \tag{5.21}$$

The wind buffeting load at a single point is modified with an aerodynamic admittance function, correcting the QSS buffeting load in Eq. (4.12) as:

$$\mathbf{B}_\mathrm{q}(\omega) = \frac{\rho V B}{2} \begin{bmatrix} 2C_\mathrm{D} A_\mathrm{yu}(\omega) & (C'_\mathrm{D} - C_\mathrm{L}) A_\mathrm{yw}(\omega) \\ 2C_\mathrm{L} A_\mathrm{zu}(\omega) & (C'_\mathrm{L} + C_\mathrm{D}) A_\mathrm{zw}(\omega) \\ 2C_\mathrm{M} A_\mathrm{rxu}(\omega) & BC'_\mathrm{M} A_\mathrm{rxw}(\omega) \end{bmatrix} \tag{5.22}$$

The two-point spectral wind buffeting load is calculated with the integration of the coherent spectral load across the exposed wind length as:

$$\mathbf{S}_{\text{load,ij}}(\omega)=\int_L\int_L \boldsymbol{\varphi}_i^{\mathrm{T}}(x_i)\mathbf{B}_{\text{q,i}}(\omega)\mathbf{S}_{\mathrm{V}}(\omega)\mathbf{B}_{\text{q,j}}^{\mathrm{T}}(\omega)\boldsymbol{\varphi}_j(x_j)dx_i dx_j \tag{5.23}$$

Here, the frequency-domain representation of vertical lateral wind fluctuations is described with a correlated wind fluctuation matrix:

$$\mathbf{S}_{\mathrm{V}}(\omega)=\begin{bmatrix} S_{\mathrm{uu}}(\Delta \mathrm{x},\omega) & S_{\mathrm{uw}}(\Delta \mathrm{x},\omega) \\ S_{\mathrm{wu}}(\Delta \mathrm{x},\omega) & S_{\mathrm{ww}}(\Delta \mathrm{x},\omega)\end{bmatrix} \tag{5.24}$$

where the off-diagonal entries are commonly modeled as $S_{\mathrm{wu}} = S_{\mathrm{uw}} = 0$. The spectral response containing the single-sided spectrum is computed as:

$$\mathbf{S}_{\mathrm{qq}}(\omega)=\boldsymbol{\varphi}(x_{\mathrm{r}})\left[\mathbf{H}_{\mathrm{env}}(\omega)\mathbf{S}_{\mathrm{load}}\mathbf{H}_{\mathrm{env}}^{*}(\omega)\right]\boldsymbol{\varphi}^{\mathrm{T}}(x_{\mathrm{r}}) \tag{5.25}$$

The corresponding covariance is computed as a 3×3 covariance matrix:

$$\mathbf{Cov}(x_{\mathrm{r}})=\boldsymbol{\varphi}(x_{\mathrm{r}})\int_0^{\infty}\left[\mathbf{H}_{\mathrm{env}}(\omega)\mathbf{S}_{\mathrm{load}}\mathbf{H}_{\mathrm{env}}^{*}(\omega)\right]d\omega\boldsymbol{\varphi}^{\mathrm{T}}(x_{\mathrm{r}}) \tag{5.26}$$

A fully coretlated and uncorrelated response is demeonstrated in Figure 5-3 from From chapter 6.

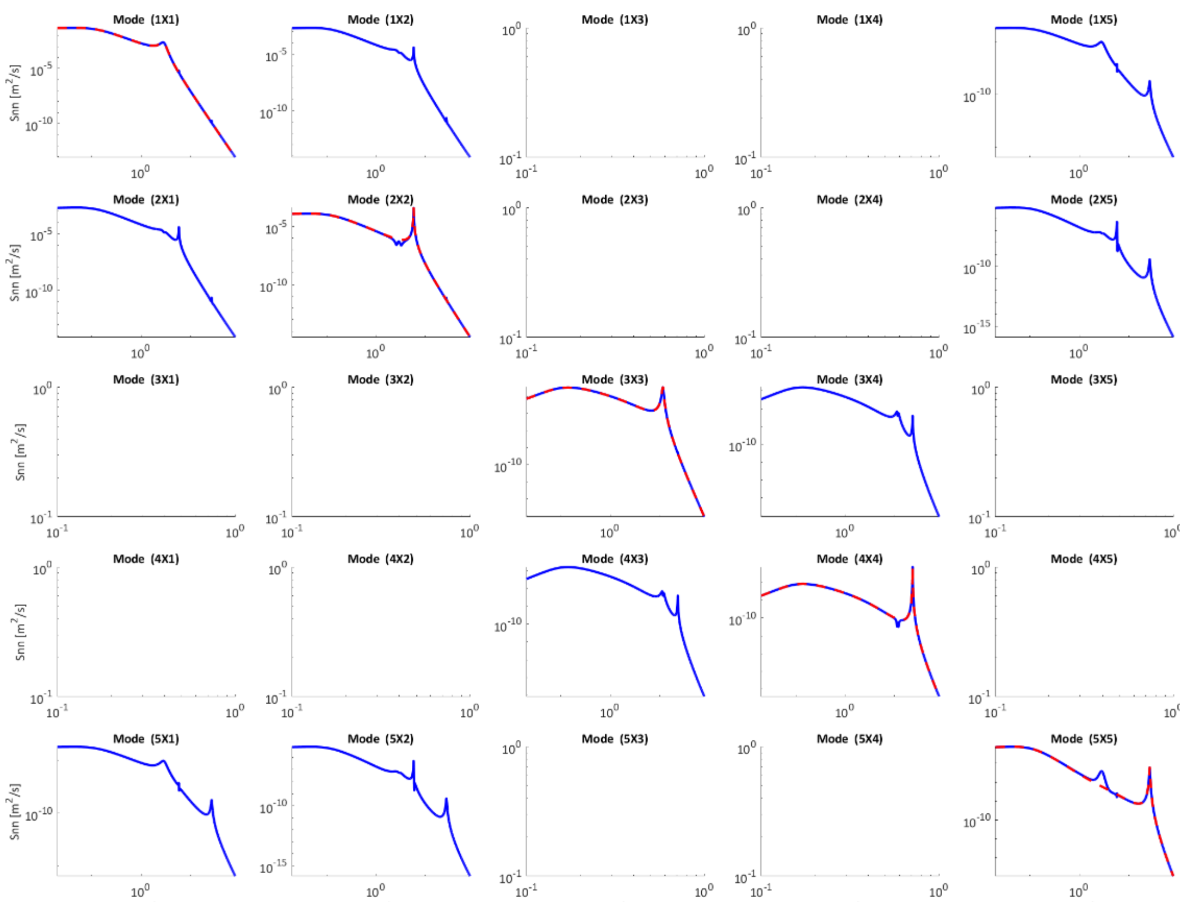

Figure 5-3: 5DOF fully corelated (blue) and uncorrelated (red) wind buffeting response.
Slika 5-3: Dinamična analiza odziva mustu z vezanimi (modra) in nevezanimi (rdeča) enačbami odziva.

6 STUDY CASE OF A TLP FLOATING BRIDGE

This demonstration presents a practical example of a floating bridge feasibility study investigation. This thesis presents the environmental loads that were introduced in this time-domain numerical model. Floating bridge design is a rather complex project, requiring many steps to build the dynamic equations of motion. This research work was developed and implemented stepwise for over five years. Different phases of the project added increasingly sophisticated hydrodynamic and wind load models. One of the most promising crossings is the 5 km wide Bjørnafjord. Its 1/2 kilometer deep fjord presents several alternatives, such as underwater tunnels, multipontoon floating bridges and TLP multispan suspension bridges. The demonstration herein involves an attractive TLP suspension bridge. The bridge concept was developed in a cooperation between the NPRA and a group of consultants, consisting of Aas-Jakobsen, COWI, Johs Holt, Moss Maritime, Wind OnDemand, Aker Solutions, NGI and Plan Arkitekter. A multispan suspension bridge is itself a challenging project when combined with the Bjørnafjord dynamic excitation, thus requiring the special project development presented in this thesis.

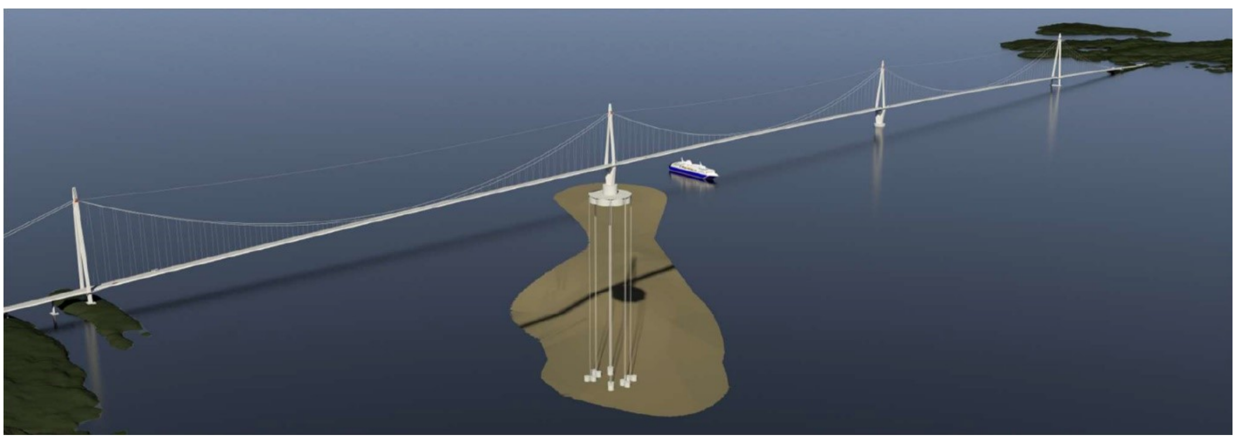

Figure 6-1: TLP Bjørnafjorden suspension bridge rendering [1].

Slika 6-1: Vizualizacija TLP visečega mostu preko ožine Bjørnafjorden [1].

The Bjørnafjord suspension bridge consists of a three-span bridge with two rock-founded towers on each side of the fjord and two floating pylons in the fjord. The floating pylons are found on TLP platforms at depths of 550 and 450 m. These TLP floaters are subject to water-bridge interactions and wave loads, introducing some new aspects to a multispan suspension bridge. Normally, the ULS design loads are dynamic wind, traffic and road traffic accidents, but in the case of Bjørnafjorden, we also need to consider the wave, current and ship impact loading. To reproduce the environmental factors, the dynamic loads simulate wind and waves in a fully coupled time-domain analysis. Additional top cables are unique design features of TLP bridges; they reduce vertical sagging and suppress some dynamic excitation. This bridge design is not feasible without an accurate time-domain analysis, as presented in this thesis.

6.1 Structural finite element model

A structural model of the bridge, depicted in Figure 6-2, is developed in *RM Bridge*. Twelve-DOF line beam elements, with a weak finite formulation, are used for the numerical model of the pylons and bridge deck. The steel pylons have variable cross-sections with stiffeners and cross diaphragms inside the tower. The proper mass is applied to represent the dead load and superimposed dead load. The main cables, hanger, and top cables are modeled with a special nonlinear cable formulation, allowing compensation of the axial stiffness due to normal forces and transversal loads. A set of linear springs is used to simulate the soil foundation. Nonlinear damper elements are used to simulate different connections between the deck and pylons. A high-tensioned top cable system is suspended between each span and anchored within the spreading chamber of the anchor foundation. The top cable reduces the pylon top displacement from an unfavorable traffic position. The connection between the deck and the floaters is laterally restrained and has free longitudinal bearings. The bridge deck ends have restrained lateral motion and free longitudinal motion. Additional 15 MN end stoppers are activated for excess bridge deck motion. The submerged parts of the floaters are modeled as rigid bodies connected to the seabed by massless cable elements representing the tendons. The hydrodynamic properties are included at the hydrodynamic points, defined at each pylon in one node at sea level. The wind loads are introduced as finite element loads. The investigated structural model reflects the nonlinear geometrical large-displacement theory and includes nonlinear dampers and all relevant dynamic loads.

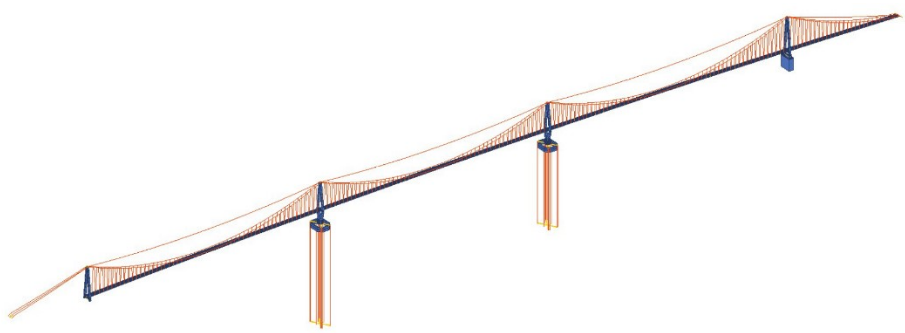

Figure 6-2: RM Bridge finite element model, 3rd phase [91].

Slika 6-2: Model končnih linijskih elementov v programu RM Bridge [91].

A form-finding procedure is carried out prior to any dynamic analysis investigations. The multiparameter optimization of approximately 3000 nonlinear variables is performed to calculate the proper initial form and structural forces. The results are stored in a permanent load file $\mathbf{F}_{\text{perm}}$ together with the horizontal static loads to build the initial tangent stiffness as a basis for further time-domain analysis.

6.2 Hydrodynamic properties

The hydrodynamic linear wave radiation loads are modeled as frequency-dependent hydrodynamic damping and added mass. Nonlinear VDD element loads are added to all submerged elements of the hull and tethers. The representative design wave condition values for locally generated wind waves are listed in Table 6-1. The time-dependent loads can be generated and imported to a time-integration scheme. The wave loads are not included at present, as the focus is on the wind buffeting response calculation only.

Table 6-1: Wind-generated waves for the Bjørnafjorden crossing, and the JONSWAP spectrum input [59].
Preglednica 6-1:Parametri obtežbe valov za JONSWAP spekter, za primer ožine Bjørnafjorden.

Return period/Sectors	**1 year**		**10 years**		**100 years**		**10 000 years**	
	Hs [m]	Tp max	Hs [m]	Tp max	Hs [m]	Tp max	Hs [m]	Tp max
345° - 75°	0.8	4.0	1.1	4.5	1.5	5.0	2.3	5.9
75° - 105°	1.6	5.3	2.2	5.9	2.8	6.6	3.9	7.6
105° - 165°	1.1	4.4	1.3	4.8	1.6	5.3	2.3	6.1
165° - 225°	1.2	4.4	1.5	4.9	1.9	5.3	2.7	6.1
225° - 315°	1.3	4.6	1.8	5.3	2.4	5.9	3.3	6.8
315 - 345°	1.5	5.1	1.9	5.6	2.5	6.2	3.5	7.2

The hydrodynamic added mass is represented as a 6×6 symmetric mass matrix, assigned to the hydrodynamic node. Here, aerodynamic damping is the recalculated input of the hydrodynamic panel theory. The VDD parameters are set as quadratic damping terms with the effective diameters of the tethers and hull cross-sections. The underwater currents are not included in the following analysis.

6.3 Dynamic wind properties

The wind velocity series are simulated using the Kaimal power spectrum and exponential wind coherence presented in Table 6-2. The mean wind properties have an exponential height distribution, with parameters defined at a 10 m reference height with a velocity V_{ref}=26 m/s and an exponential factor α=0.127. This scenario generates a mean wind speed of 32 m/s at a deck elevation h=60 m. The Kaimal power spectrum uses a spectrum factor ε=0.3. The turbulence intensity is assumed to be constant over the height of each floating pylon. This investigation considers a 100-year return period of the dynamic wind buffeting load, presenting a simulation of a nonhomogeneous wind field due to changing mean wind velocities over the height.

Table 6-2: Dynamic wind properties for a 100-year return period.
Preglednica 6-2: Lastnosti dinamičnega turbulentnega vetra pri povratni dobi stotih let.

	u along wind	**v** vertical	**w** horizontal
Kaimal power spectrum parameters			
Length scale	245	28	85
Turbulence int.	0.15	0.07	0.11
Exponential coherence			
	ΔX	ΔY	ΔZ
u	0	10	10
v	0	3	6.5
w	0	6.5	6.5

For this investigation, the QSS wind buffeting load theory applies, and a full vector wind buffeting load formulation considering all small squared terms is used. The aerodynamic damping and stiffness according to the QSS load, assuming a fully developed wind flow around the deck, are constant non-frequency-dependent matrices. The QSS formulation is evaluated from the aerodynamic coefficients of the deck, as depicted in Figure 6-3. The cable elements have an assigned drag coefficient CD=0.8. The pylon aerodynamic coefficients include the shedding effects on each other, thus making this input elevation dependent.

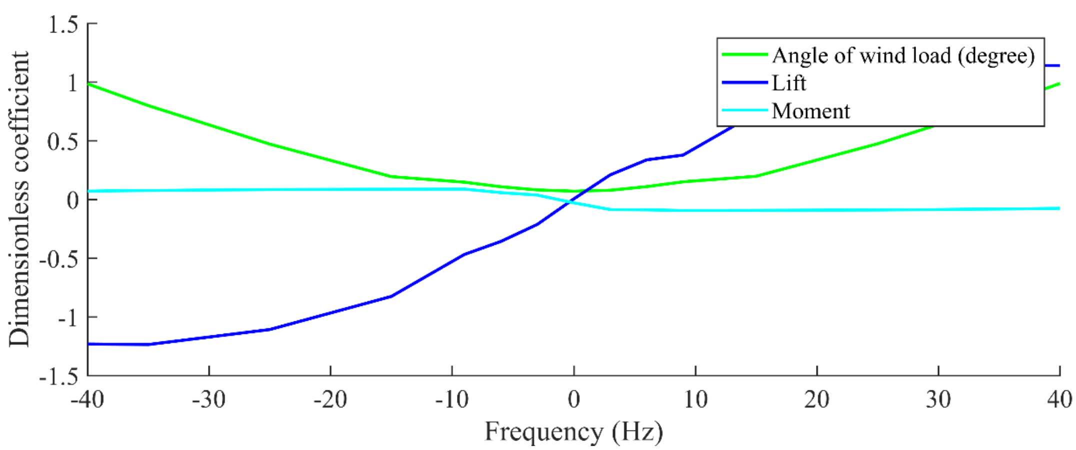

Figure 6-3: Aerodynamic coefficients for the deck, with width B normalized.
Slika 6-3: Aerodinamični koeficienti za prečni presek mostu.

6.4 Environmental equation of motion

The global analysis of all environmental loads is a comprehensive study that includes all of the above-described interactions. For demonstration purposes, an individual turbulent wind load event is calculated, after which the time domain and frequency domain results are compared. The equation of motion can be written as:

$$\begin{aligned}\left(\mathbf{M}+\mathbf{M}_{\text{hy}}(\infty)\right)\ddot{\mathbf{u}}+\left(\mathbf{C}+\mathbf{C}_{\text{hy}}(\omega)+\mathbf{C}_{\text{qss}}\right)\dot{\mathbf{u}}+\left(\mathbf{K}_{\text{nl}}+\mathbf{K}_{\text{hy}}+\mathbf{K}_{\text{qss}}\right)\mathbf{u}= \\ \mathbf{F}_{\text{perm}}-\mathbf{F}_{\text{cur}}\dot{\mathbf{u}}^{2}+\mathbf{F}_{\text{buf}}(t)\end{aligned} \tag{6.1}$$

The results of this analysis are presented for the frequency-domain and time-domain formulations. To better understand the dynamic responses of those unique structures, this thesis develops a self-excited load formulation, which is not presented in this example. Self-excited new load models have been successfully developed and validated. The commercial use of these algorithms is possible in the presented time-integration calculation. Several tests have been performed on a full bridge; however, additional software validation might be required, which represents future work.

6.5 Frequency-domain analysis

The presented frequency-domain tools calculate the dynamic properties of a floating bridge. Here, the modal decomposition is calculated for the suspension bridge structure, including the hydrodynamic added mass effects. The presented nonlinear algorithm iteratively resolves the matching of the calculated natural structure frequency and applies an appropriate hydrodynamic added mass. The procedure is repeated for each individual frequency, and the evolution of each frequency can be monitored. Changes in the natural periods, changed modal shapes and even frequency shifts due to the changed added mass are expected. The hydrodynamic mass has a large and important effect on the modal analysis.

For this analysis, an external MATLAB script was used to run the iterative eigenvalue procedure. The scripts evaluate the structural frequencies and assign the appropriate hydrodynamic added mass for the next iteration. The evolution of each frequency and the changes in frequency and shapes are observed. The *RM Bridge* software calculates the combined structural and hydrodynamic frequencies. For this floating bridge, the first 13 eigenfrequencies are changed due to hydrodynamic mass effects, as presented in Table 6-3. The first few eigenvalues are influenced considerably, approximately within a range of 12% to 20% of the changed mass. The vertical (V) and lateral (L) bridge directions are influenced by these effects in different ways. During iteration, the mode shapes do not change considerably, and no frequency shift is observed for this investigation. An exception is mode no. 13; this mode completely disappears from the eigenfrequency list due to the large activated rotational added mass. The original shape undergoes rotation at the hull, which is restrained by a large activated hydrodynamic mass. Proper control over these algorithms is important to properly evaluate the modal decomposition results.

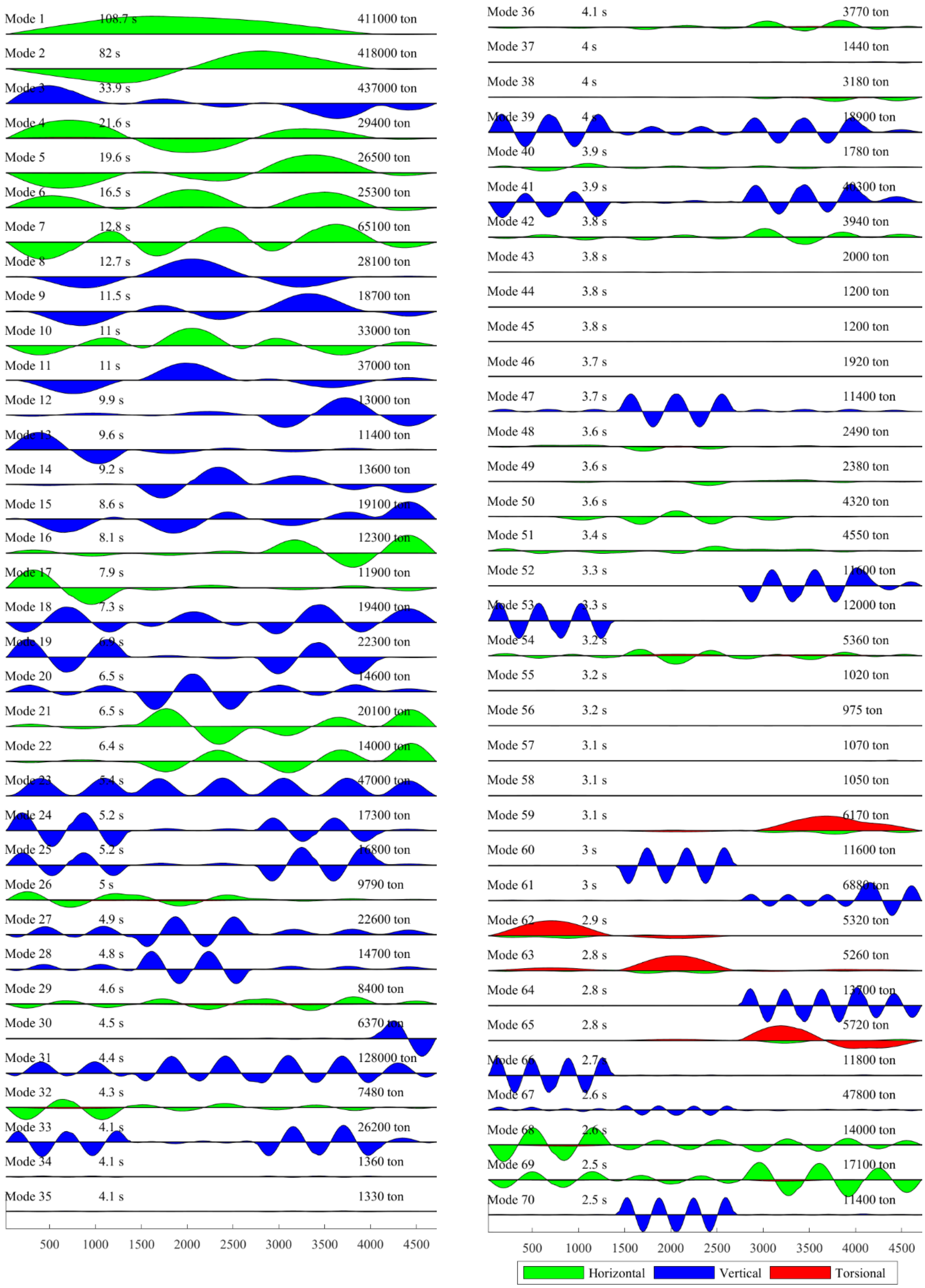

Figure 6-4: Modal analysis of the TLP bridge.

Slika 6-4: Modalna analiza TLP mostu.

Table 6-3: Eigen value frequencies of the TLP bridge.

Preglednica 6-3: Lastne vrednosti frekvenc za TLP most.

Mode	**Frequency** [rad/s]	**Change in M(∞)/M(ω)**		**DOF**
		Frequency	Mass	
1	0.062	6.1%	12.7%	L
2	0.082	5.7%	12.9%	L
3	0.196	6.7%	19.8%	V
4	0.292	0.0%	-1.4%	L
5	0.322	0.3%	-0.5%	L
6	0.382	0.8%	-1.5%	L
7	0.497	0.0%	0.9%	L
8	0.506	0.8%	8.4%	V
9	0.550	0.0%	0.2%	V
10	0.581	0.0%	-0.8%	L
11	0.630	-0.8%	-20.0%	V
12	0.653	-0.8%	-41.2%	V

For this wind buffeting analysis, this important damping properties of floating bridges are considered. The damping can be calculated in a straightforward manner for each damping mode-per-mode, presenting us with the information available on the total damping for low-damped structures. The damping is calculated according to Eq. (5.12) and is expressed relative to a logarithmic decrement as:

$$\delta_{ij} = \frac{\mathrm{C}_{ij}}{\xi_{\mathrm{critical},i}} = \frac{\mathrm{C}_{ij}}{2\sqrt{\mathrm{K}_i \mathrm{M}_i}} \tag{6.2}$$

where M is the generalized modal mass, K is the generalized modal stiffness, C is the damping component, index i is the mode and index j is the source of the damping. The Rayleigh damping formulation defines the structural damping of each mode, making it comparable to the time domain result. Hydrodynamic radiation damping is included in the pylon hull properties. This value represents 6-DOF fully correlated damping. Wind-induced vibration contributes to aerodynamic damping and aerodynamic stiffness, which are modeled with QSS theory. The linearized VDD is neglected in this analysis. The total damping C_{tot} is the sum of the structural damping C_{str}, aerodynamic damping C_{qss}, hydrodynamic damping C_{hy}, and linearized viscous damping C_{curr}, expressed as.

$$C_{\mathrm{tot}} = C_{\mathrm{str}} + C_{\mathrm{qss}} + C_{\mathrm{hy}} + C_{\mathrm{curr}} \tag{6.3}$$

Total damping is used in the wind buffeting calculation. Different sources of damping for the floating bridge frequencies are depicted in Figure 6-5. The logarithmic damping ratios for a frequency band of 0 to 1.8 rad/s are presented, with important low- and high-frequency bridge responses. Hydrodynamic damping makes a major contribution in the range from 0.5 to 0.8 rad/s because this range structure dissipates energy and introduces the energy of wave loads. Cable-suspended structures have low structural damping and are sensitive to the resonant excitation of wind turbulence. Aerodynamic damping is continuously distributed along the frequencies and is important for both a low-frequency response and a high-frequency response. Notably, aerodynamic damping is not present for no-wind conditions, and a large response is observed during swell load events.

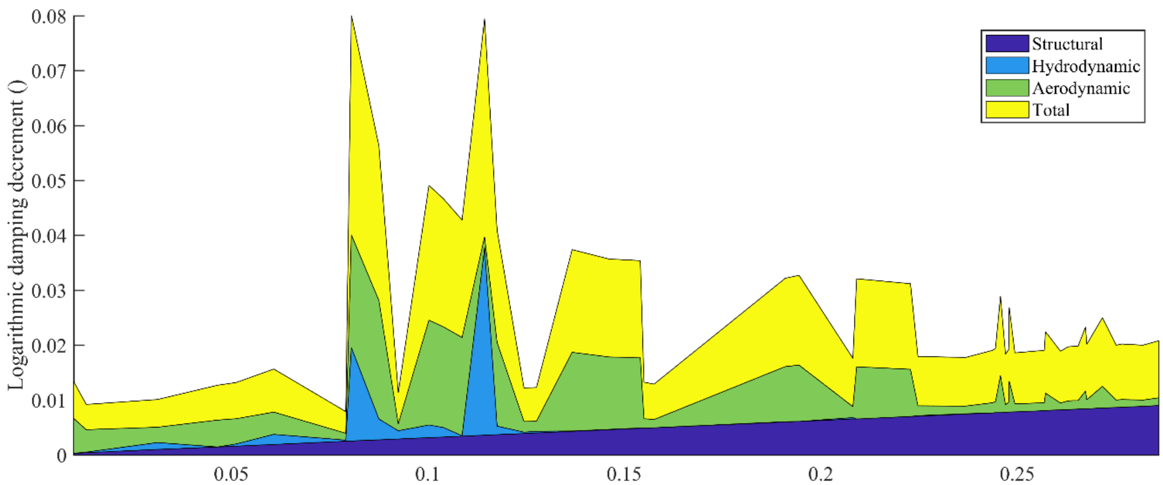

Figure 6-5: Different damping sources for TLP bridges.

Slika 6-5: Različne vrste dušenja za TLP most.

Moreover, it makes a major contribution to the total damping and a strong contribution to the vertical movement of the deck. The structural deck is the main mechanism of wind-induced damping and directly affects the global structural response. The improved self-excited forces would result in an important improvement in the prediction of aerodynamic damping and the accuracy of floating bridges.

RM Bridge software was used to calculate the wind buffeting response. The advanced wind module calculates the uncorrelated wind buffeting response with the mode-per-mode decomposition method. In this approach, the correlation between different modes is neglected, and the modes are later summed together with a modal CQC superposition rule. The total damping is externally calculated and introduced in a total table. The damping table is then included in the response calculation, which is performed by use of software integration algorithms.

6.6 Fully coupled time-domain analysis results

The time domain of hydrodynamic and aerodynamic effects is implemented in the *RM Bridge* software and used for this demonstration. The wind buffeting calculation is carried out for 1 hour of simulation time, and approximately 25 CPU hours are needed to complete the calculation on one 4 GHz core. The total fixed realizations are calculated to obtain the proper mean value statistics of the response. The RMS response is calculated for each time signal to directly compare the result to that in the frequency domain [92] [93]. Here, the bridge deck response along the 4730 m long deck station is presented. The response vibration is calculated using the two-dimensional Fourier transform along the frequency axis and along the bridge station, as depicted in Figure 6-6.

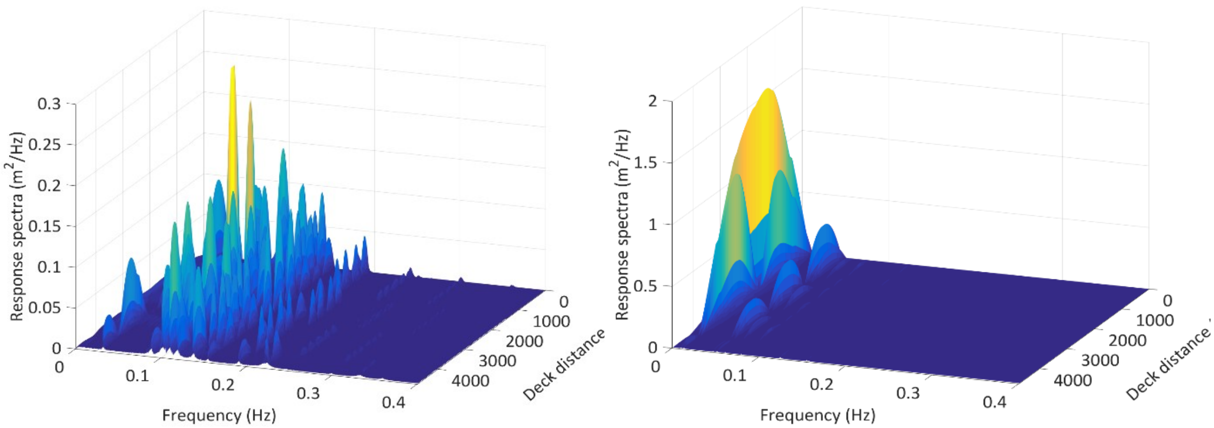

Figure 6-6: Vertical (left) and lateral (right) RMS bridge deck response.

Slika 6-6: Prikaz RMS odziva v vertikalni smeri (levo) in prečni smeri (desno).

Lateral and vertical response deck responses are the main mechanisms for aerodynamic damping. The response shows what modes have been excited and the corresponding amplitudes. The lateral response is dominated by the low-frequency response of the first few modes, where for slow motion, the QSS damping approximation may be valid. The vertical response has a wider frequency response from 0.1 to 0.2 Hz and excites multiple natural modes. The spread contribution of vertical responses for these frequencies suggests that a self-excited force model is more appropriate to reflect the measured aerodynamic damping. This compelling argument confirms the findings and research work on the suggested self-excited models.

6.7 Comparison of results

To conclude this investigation, the results of both methods for a floating bridge are presented. The frequency-domain analyses do not include any wind correlation effects and are defined with the QSS wind buffeting load formulation [94] [95]. The results are compared to the time-domain analysis results and are evaluated with the QSS wind buffeting load model. The time-domain calculations include coupling and nonlinear effects. The results of those analyses are presented for the lateral direction in Figure 6-7 and for the vertical direction in Figure 6-8.

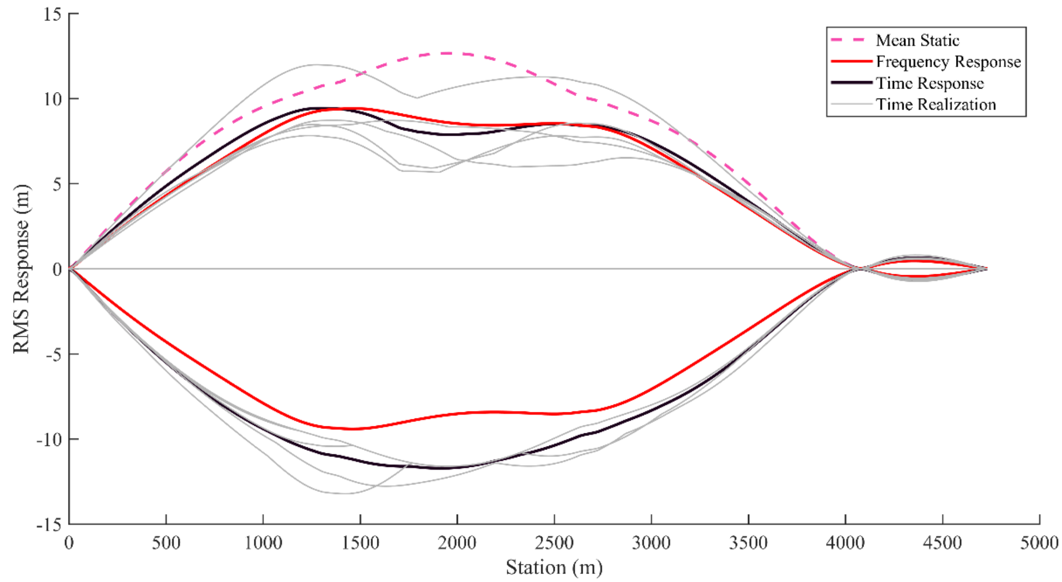

Figure 6-7: Bridge deck response in the lateral direction: time-domain vs. frequency-domain analysis.
Slika 6-7: Odziv v prečni smeri, časovna in frekvenčna metoda.

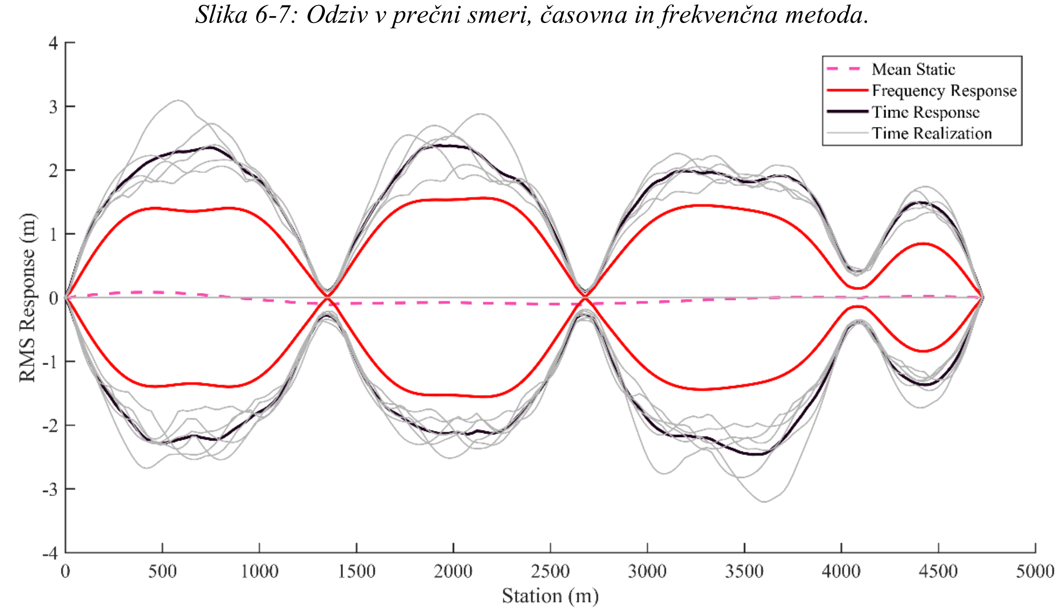

Figure 6-8: Bridge deck response in the vertical direction: time-domain vs. frequency-domain analysis.
Slika 6-8: Odziv v vertikalni smeri, časovna in frekvenčna metoda.

A comparison of the deck response with both the time- and frequency-domain approaches shows good agreement. Some differences are observed for both directions and are sourced from the nonlinear structural response and coupling effects. The lateral transversal stiffness is lower when the bridge oscillates over the initial nondeformed position, resulting in a nonsymmetrical time-domain response around the mean wind deflection. The overall lateral responses of both methods agree well. The vertical time domain results have larger osculation compared to the frequency domain results. Detailed investigations have shown a nonlinear vertical motion introduced by horizontal movement. This effect is due to the large displacement and introduces new lower-mode excitation, which does not occur in tangential matrix modal decomposition and is used for frequency-domain wind buffeting calculations. The nonlinear top cables introduce nonlinear induced motion and are directly related to the top tower horizontal motion and vertical deck motion. For lateral and vertical response calculations, the linearized frequency decomposition methods do not deliver the most reliable results, and time-domain large-displacement methods are more suitable. Important for multiexcited systems is to consider the modal coupling effects, which are neglected in this frequency-domain analysis but are included in the time-domain analysis.

Overall, the agreement of the results confirms the two independent analyses and validates the newly implemented time-domain formulations. They calculated the correct response according to the simplified QSS wind load theory. The time-domain formulation is well suited for the investigation of coupled and nonlinear structural response effects, thus validating the use of these models for further floating bridge design and development.

7 CONCLUSIONS

A comprehensive overview of environmental loads on a floating bridge structure was provided. The interaction of the bridge with wind and wave loads can be described by adding terms to the dynamical equilibrium equation. Newmark time integration successfully resolves the dynamic equation of motion under the cooperation of structural nonlinearities and environmental loads. This is the most promising approach to evaluate possible nonlinear and coupling effects. All environmental loads, i.e., wave loads, wave radiation damping, VDD, current, turbulent wind, and aeroelastic damping, were successfully introduced. Environmental loads were individually tailored to fit within the time-domain integration scheme. A series of software tests and development works was performed to validate the functionality of the proposed models, and this partly overlapped with parallel project work in the industry sector. Industry has successfully investigated different floating bridge crossing possibilities using several commercial codes. Several years of development were required to introduce the presented environmental loads and apply them to bridge design.

The main goals of the research were achieved by investigating various self-excited wind formulations. The approximative QSS formulation can provide reasonable accuracy in the early design stages and was implemented in this research work. Its convenient implementation and accessible input make it a common design choice. Since this simplified method is not accurate for higher wind speeds and does not correctly predict the aeroelastic instability, several self-excited force models were presented. The linear self-excited functions were described by 18 flutter derivative functions. An example rational function formulation was transferred into the current time-domain framework by using the hydrodynamic numerical convolution implementation. The research goal was achieved, proving that the rational function can be transformed into a suitable formation without any additional software extension. The developed formulation exhibits high numerical robustness. The accuracy of the rational function and polynomial fit was evaluated with wind tunnel testing, showing good agreement of the results with wind tunnel measurements. The presented RFs are state-of-the-art linear self-excited wind models and can now be successfully integrated into floating bridge design. This reformulated wind self-excited force is suitable for use in various other hydrodynamic software programs, where hydrodynamic-dependent damping is similarly convoluted over velocity motion. The proposed algorithms can be applied across different solutions of fully coupled environmental loads.

During the mathematical reformulation of the self-excited forces, an important relation between the aeroelastic damping and stiffness of causal dynamic systems was discovered. This allowed us to further explore the nonparametric modeling of self-excited forces and to present a new novel approach. Simplified linear regression techniques can now be successfully applied to the newly developed self-excited algorithm via numerical convolution integration. Furthermore, the frequency contribution of either the damping or stiffness can be chosen for input, thus allowing the selection of more reliable and less scattered data. This procedure considerably simplifies the modeling effort since it no longer requires nonlinear regression, achieving one of the thesis goals.

An alternative approach is offered that is very attractive for design work since it does not require any special nonparametric fitting techniques or know-how and can be used without extensions. Both parametric and nonparametric models show excellent agreement with the wind tunnel experiments. This result represents an important scientific contribution, as presented in the attached paper: a nonparametric modeling of unsteady self-excited forces based on the relations between the flutter derivatives.

The research hypothesis was proven by the successful mathematical reformulation of wind self-excited forces. Numerical validation was used to validate the transformation of RFs. The presented models are now suitable for implementation in the floating bridge dynamic equation of motion. Additional experimental tests were conducted to investigate different fitting possibilities for flutter derivatives, such as parametric and nonparametric fits. This research offers the possibility of introducing more accurate state-of-the-art self-excited formulations into floating bridge projects. Such an implementation will allow immediate feedback regarding the aeroelastic performance, thus resulting in an efficient design process. The developed models allow for accurate and economically designed bridges that meet the high industry criteria. The proposed formulation is an alternative way to implement the time-domain calculation of self-excited wind loads. Nonparametric fitting can be further utilized to improve the uncertainty, leading to important project savings. Future research is needed to confirm these ideas with various cross-sections. The author hopes that interested readers will find this work inspiring and helpful in their professions. The new bridges discussed offer hope for a sustainable future. Innovations such as these often require out-of-the-box thinking and new ideas to be investigated.

8 EXTENDED ABSTRACT IN SLOVENIAN

8.1 Uvod

V nadaljevanju je predstavljen povzetek doktorske disertacije v slovenskem jeziku. Eden od ciljev norveškega ministrstva za promet (Statens vegvesen) je izvedba projekta E39, izgradnje neprekinjene obalne avtoceste med mestoma Kristiansand in Trondheim, dolge približno 1100 km. Potovalni čas z osebnim vozilom danes znaša 21 ur in bo z vzpostavitvijo neprekinjene cestne povezave skrajšan na 11 ur. Cilj bo dosežen z zamenjavo trajektov z mostovi in tuneli. Premostitev širokih in globokih fjordov predstavlja svojevrsten inženirski izziv, saj trenutno premostitvene rešitve, ki bi premoščale razdalje več kilometrov brez vmesnega temeljenja, še ne obstajajo. V ta namen se izvajajo študije izvedljivosti in razvoj različnih tehnoloških rešitev za premostitev fjordov. V študijah izvedljivosti so bile preučevane štiri glavne možnosti premostitev z izvedbo: mostov z ekstremnimi razponi, visečega mostu na plavajočih pontonih, podvodnih tunelov in večpontonskih plavajočih mostov, prikazanih na sliki 1-1. Za vsak fjord je bila narejena presoja najustreznejših rešitev in s tem izbrana najprimernejša tehnologija premostitve. Raziskovalno delo je potekalo vzporedno s projektantskim delom avtorja na raznih študijah izvedljivosti premostitev fjordov. Raziskovalna naloga se ukvarja z razvojem novih konceptov plavajočih mostov, ki združuje multidisciplinarne inženirske strokovnjake s področja konstruiranja mostov, pomorske inženirje, raziskovalce in programerje. Disertacija navaja pregled vseh pomembnih dinamičnih obremenitev plavajočih mostov, kot je obtežba valov in turbulentnega vetra. Za konstruiranje mostov so potrebna nova numerična orodja za analizo, ki celovito obravnavajo zahtevne dinamične odzive. Sočasno delovanje različnih obtežb je pomembno pri razumevanju zapletenih dinamičnih odzivov, ki jih spremlja nelinearen odziv. Za konkreten problem je bila uporabljena nelinearna časovna integracija, v katero so bile vgrajene nove kombinacije dinamičnih obtežb. Pomanjkanje razpoložljivih numeričnih orodij in literature s tega področja delno odpravlja to doktorsko delo. Vse predstavljene dinamične obtežbe so bile vgrajene v komercialno programsko kodo *RM Bridge*, ki je bila večkrat uporabljena pri snovanju plavajočih mostov. Glavno delo avtorja je bilo razvijanje zahtevane programske razširitve za izračun dinamike vetra in valov, sestavljeno je bilo iz teoretičnega raziskovanja, načrtovanja algoritmov, implementacije kode in obsežnega testiranja. Razvoj in testiranje numeričnih orodij sta potekala postopoma v večletnih razvojnih etapah. Tako razvita numerična orodja omogočajo izvedbo različnih vrst plavajočih mostov in so na voljo konstruktorjem za nadaljnje delo. V tem delu predstavljeni in razviti numerični modeli so primerni za izračun kompleksnih scenarijev dinamičnih obremenitev. Predstavljeno delo ima dodano raziskovalno vrednost in je namenjeno bodočim raziskovalcem, investitorjem, konstruktorjem in programerjem.

Pregled raziskav

Za računanje nelinearnih odzivov mostov so pogosto uporabljene metode časovne integracije, v tem delu je bila uporabljena priljubljena Newmarkova metoda. Pregled hidrodinamičnih obtežb je predstavljen v tretjem poglavju, uvedba vetrne dinamične obremenitve je predstavljena v četrtem poglavju. Obremenitve okolja na most lahko dodatno razdelimo na konstantne, časovno odvisne obremenitve in samovzbujajoče (self-excited) obremenitve. Za ustrezno izbiro izračunov v časovni [3] ali frekvenčni domeni [4] je pogosto potrebno matematično preoblikovanje obremenitve. Samovzbujajoče vetrovne in valovne obremenitve so po definiciji linearne frekvenčno odvisne funkcije in predstavljajo harmonično superpozicijo posameznih frekvenc. Takšnih obremenitev ni mogoče neposredno uporabiti v Newmarkovi integracijski shemi, saj vrednosti ni mogoče izraziti kot časovno odvisne ali pomično odvisne matrike konstrukcije. Te obtežbe je mogoče uvesti v časovno integracijo s pomočjo matematične operacije konvolucijske transformacije [6]. V tem delu je uporabljena klasična integracija konvolucije, ki izračuna silo kot konvolucijski integral za vsa pretekla gibanja. Vrednotenje obtežb v vsakem časovnem koraku lahko v praksi predstavlja časovno intenziven izračun. Sprogramiran vmesnik konvolucije hidrodinamičnih sil je bil posebej razvit v komercialni programski opremi za dinamične časovne integracije [2] [3].

Hidrodinamični učinki so dobro raziskani v pomorskem inženiringu. V zadnjih nekaj desetletjih je bilo zgrajenih več naftnih ploščadi v razburkanem Severnem morju. V pomorskem inženiringu so na voljo različne hidrodinamične formulacije obremenitev, primerne za uporabo pri analizi plavajočih struktur [9] [7]. Dinamična analiza vetra je skupek srednje vetrne hitrosti, turbulentnega vetra in gibanja strukture. Gibanje strukture samovzbujajočih sil vetra je mogoče opisati z linearno kvazistatično metodo QSS (Quasi-Steady State), ki predpostavlja poenostavljen teoretični model interakcije, modeliran s konstantnimi matrikami aerodinamičnega dušenja in aerodinamične togosti. Model QSS se pogosto uporablja za aproksimativni izračun odziva mostov pri nizkih hitrostih vetra in je bil uspešno vgrajen v Newmarkovo shemo [4]. Pomanjkljivost metode QSS je neprimernost za raziskovanje nestabilnosti omahovanja, ki se izraža v odstopanju od v vetrovniku izmerjenih sil.

Cilji raziskav

Srčiko doktorskega dela predstavlja nadgradnja interakcije QSS z bolj natančnim modelom, ki temelji na odvodih omahovanja (flutter derivatives). Takšna formulacija je bolj natančna in je v skladu z eksperimentalnimi rezultati. Predstavljen je model interpolacije aeroelastičnih sil racionalnih funkcij, katerega različni primeri so v aeroelastičnih raziskavah dobro poznani in nudijo natančnejše podatke. Aeroelastično modeliranje prinaša nekaj izzivov, ki predstavljajo težave pri sami uporabi matematično zahtevne metode. Neposredno programiranja racionalnih funkcij ni mogoče vgraditi v obstoječe časovne domene komercialnih orodij. Raziskava preučuje alternativne možnosti matematičnih formulacij, ki lahko uporabijo že obstoječo funkcionalnost hidrodinamične analize brez dodatnega komercialnega razvoja. Hipoteza je dokaz primerne formulacije elastičnih sil v dinamičnih enačbah gibanja. Dokazovanje poteka s pomočjo numeričnega testiranja in primerjave z rezultati iz vetrovnika. Predstavljen je nov model aeroelastičnih sil vetra, ki omogoča aeroelastično modeliranje na že sprogramiranem vmesniku hidrodinamičnih konvolucij. Praktičen namen raziskave je najti eventualno poenostavitev teorije v praksi in ohraniti natančnost modelov za bodoči izračun plavajočih mostov.

8.2 Časovna integracija

To poglavje prikazuje osnove dinamičnih izračunov plavajočih konstrukcij. Prikazani so možni algoritmi časovne integracije, primerni za reševanje dinamičnih enačb gibanja. Najprej sta pojasnjeni dve skupini izračuna odziva mostu, frekvenčna domena in formulacija časovne domene, predstavljeni v reglednici 2-1. Opisani metodi sta primerni za izračun linearnih odzivov, za izračun nelinearnih odzivov pa so primernejše metode časovne domene. Frekvenčne metode temeljijo na rezultatih modalne linearne dekompozicije lastnih vrednosti in dajejo pomembno referenčno vrednost pri testiranju časovnih metod, podrobno so predstavljene v poglavju 5. Frekvenčni pristop je v projektiranju priljubljen, saj razpolaga z nazornimi informacijami o individualnem prispevku posameznih nihajnih oblik. Omenjene metode so računsko učinkovite in vgrajene v razna orodja na tržišču.

Pri metodah časovne domene se enačbe gibanja rešujejo s časovno integracijo korak za korakom, rezultati so časovno odvisni pomiki gibanja vozlišč. Časovne integracijske metode so najprimernejše za reševanje kompleksnih nelinearnih in sklopljenih enačb gibanja. Te metode so potencialno najprimernejši kandidat za dinamično analizo plavajočih mostov, saj ponujajo natančne rezultate. Raziskave in predstavljeni algoritmi temeljijo predvsem na nadgradnji časovne integracije s posameznimi dinamičnimi obtežbami vetra in valov, ki je podrobneje prikazana v tem poglavju. Linearne enačbe gibanja mostne konstrukcije se lahko zapišejo v naslednji obliki:

$$\mathbf{M}\ddot{\mathbf{u}}(t)+\mathbf{C}\dot{\mathbf{u}}(t)+\mathbf{K}\mathbf{u}(t)=\mathbf{f}_{\text{ext}}(t). \tag{8.1}$$

$\mathbf{M}$, $\mathbf{C}$ in $\mathbf{K}$ so strukturne masna, dušilna in togostna matrika, $\mathbf{f}_{\text{ext}}$ je vektor zunanje obremenitve, $\ddot{\mathbf{u}}, \dot{\mathbf{u}}, \mathbf{u}$ so vektorji vozliščnih pospeškov, hitrosti in premikov, t je čas. Upoštevajoč geometrijske nelinearnosti, nelinearne (in neelastične) materialne modele, gibljive mase, nelinearno strukturno dušenje, se nelinearne dinamične enačbe oblikujejo kot:

$$\mathbf{M}(t)\ddot{\mathbf{u}}(t)+\mathbf{C}(\mathbf{u})\dot{\mathbf{u}}(t)+\mathbf{F}(\mathbf{u}(t))=\mathbf{f}_{\text{ext}}(t,\ddot{\mathbf{u}},\dot{\mathbf{u}},\mathbf{u}). \tag{8.2}$$

Pri nelinearni analizi visečih mostov so pogosti učinki velikih deformacij, ki so opisani s teorijo tretjega reda. Prisotni so lahko tudi materialna nelinearnost, časovno odvisne mase in dušenja. Zunanje obremenitve hidrodinamične in vetrne sile se lahko naknadno izrazijo kot dodatki matrike mase, dušenja in togosti. Prikazana je izpeljava Newmarkove metode reševanja dinamičnih enačb za linearne (8.1) in za nelinearne sisteme (8.2). Predstavljene so priporočene vrednosti β in γ, ki uravnavajo natančnost metode in numerično dušenje. Razumevanje metode lahko v praksi pripomore k uspešnemu numeričnemu reševanju dinamičnih enačb. Numerično reševanje plavajočih sistemov ni vedno trivialno in uspešno, zato je poleg teoretičnih osnov podanih tudi nekaj izkušenj z računanjem dejanskih odzivov plavajočih mostov. Kompleksnost je v obremenitvah, ki so nelinearne ali odvisne od izračunanega pomika in zahtevajo dovolj majhen časovni korak za pravilen izračun. Izbrani časovni koraki in dolžina analize morajo tudi ustrezati različnim konvolucijskim transformacijam. Predstavljenih je nekaj možnosti spreminjanja različnih parametrov za doseganje stabilne numerične sheme, ki pomagajo poiskati pravo ravnotežje med hitrim, natančnim in stabilnim reševanjem odziva.

8.3 Hidrodinamične obtežbe

Potopljeni deli plavajočega mostu so v neposrednem stiku z morjem, izpostavljeni so statičnim in hidrodinamičnim obtežbam. Statična obtežba, kot je vzgonska sila, je posledica Arhimedovega vzgona in daje podporo mostu. Poglavje obravnava dinamične obtežbe, kot so hidrodinamična togost, valovi, samovzbujajoče sile konstrukcije in morski tokovi. Hidrodinamične obremenitve pomembno prispevajo k odzivu plavajočih mostov in bistveno spreminjajo njihove dinamične lastnosti. Predstavljene so tudi osnove linearne potencialne teorije v hidrodinamiki, ki se lahko uporabi za opis hitrosti gibanja podvodnih delcev. Sprememba potenciala pa povzroči obtežbe na samo konstrukcijo, opisane s hidrodinamičnimi silami. Posledica sile valovanja je gibanje morske površine in posledica samovzbujajoče sile so pomiki konstrukcije v morju. V tem delu so opisani le hidrodinamični pojavi, pomembni za globalni odziv, vsekakor je poznanih še več pojavov, navedeni so v literaturi [9]. Osnovna predpostavka je ločeno modeliranje posameznih učinkov obtežbe, ki so matematično modelirani v »hidrodinamičnem vozlišču«. Hidrodinamično vozlišče je nato dodeljeno vozlišču posameznega pontona, ki predstavlja šest dodatnih vezanih dinamičnih enačb.

Obtežba valov

V splošnem obstajajo različni mehanizmi nastajanja valov, kot so veter, potres, podvodni plazovi, astronomska plima itd. Trenutno univerzalni matematični model, ki bi pokrival vse scenarije gibanja valov, ne obstaja, zato se uporabljajo različni poenostavljeni modeli. Valovanje morske gladine na odprtem morju lahko v grobem razdelimo na [30]: morske valove kot posledico lokalnega vetra (wind sea waves) in enakomerne valove z daljšimi periodami (swell waves). Za modeliranje obeh se lahko uporabljajo isti matematični modeli, vendar z različnimi vhodnimi podatki predstavljajo ločen obtežbeni primer. Valovi se lahko opišejo kot prostorska nihanja morske gladine, samo gibanje pod gladino pa lahko matematično opišemo s potencialom. Nihanje gladine predstavlja zapleten sistem valov in se lahko opiše kot superpozicija različnih trigonometričnih nihanj višin. Vsak val je opisan z enodimenzionalno višino proste površine, ki povzroči vodoravno in navpično gibanje podvodnih delcev. Posamezen val je trigonometrična funkcija, definirana z valovnim številom, valovno frekvenco in amplitudo vala, kar je prikazano na sliki 3-3 in sliki 3-5. Modeliranje trigonometrične superpozicije valov je najpogosteje opisano v frekvenčni domeni s spektrom valov $S_{\xi,\theta}$. Prostorski valovi imajo značilnosti glavne smeri valovanja θ in porazdelitve okoli glavne smeri, opisane s funkcijo porazdelitve D. Fouriereva transformacija omogoča modeliranje frekvenčno odvisnih obtežb ali enakovredne časovno odvisne obtežbe, prikazane na sliki 3-9. Homogeni valovi so pogosto opisani z linearnim stacionarnim Gaussovim modelom [20]. Obtežba valov se lahko modelira s šestimi komponentami sile $n \in \{1 \ldots 6\}$, izračunih kot:

$$\mathbf{F}_{\text{wave}}(x,y,t)=\sum_{i}^{N}\sum_{j}^{M}\left|F_n(\omega_i,\theta_j)\right|\sqrt{2S_{\xi,\theta}(\omega,\theta)\Delta\omega\Delta\theta}$$
$$\cos\left[\mathrm{k}_i x\cos(\theta_j)+\mathrm{k}_i y\sin(\theta_l)-\omega_i t+\varepsilon_{ij}-\phi_{ij}\right] \tag{8.3}$$

$\mathbf{F}_{\text{wave}}$ je vektor obtežbe valov, F_n je kompleksna prenosna funkcija, $S_{\xi,\theta}$ je spekter valov, ε_{ij} je naključno število spektra belega šuma, ϕ_{ij} je kot med realnim in imaginarnim delom prenosne funkcije, valovno število je $k_i = \omega_i^2/g$, θ je smer valovanja, ω je frekvenca valovanja, x in y sta prostorski koordinati.

Obtežba gibanja pontona

Gibanje pontona na morski gladini oddaja valove, ki posledično odvzemajo energijo dinamičnim sistemom. Matematični opis hidrodinamične samovzbujajoče sile je možen z dodajanjem matrik hidrodinamične mase in hidrodinamičnega dušenja. Sile so frekvenčno odvisne vrednosti gibanja, ki jih zaznamuje različna intenziteta pri različnih frekvencah nihanja, prikazana na sliki 3-10. V frekvenčni domeni se sile pogosto modelirajo kot produkt prenosne funkcije in Fouriereve transformacije pomikov, definirano kot $\mathbf{G}_{\text{hy}}(\omega)=\mathbf{H}_{\text{hy}}(\omega)\mathbf{G}_v(\omega)$. Matematično je možno pretvoriti formulacijo v časovno domeno s Cumminsovo enačbo:

$$\mathbf{q}_{\text{hy}}(t)=\mathbf{M}_{\text{hy}}(\infty)\ddot{\mathbf{u}}(t)+\frac{2}{\pi}\int_0^t\int_0^\infty \mathbf{C}_{\text{hy}}(\omega-\tau)\cos(\omega t-\tau)\dot{\mathbf{u}}(\tau)d\omega d\tau\,, \tag{8.4}$$

kjer je $\mathbf{q}_{\text{hy}}$ hidrodinamični vektor obtežbe radiacije valov, $\mathbf{M}_{\text{hy}}$ hidrodinamična masna matrika, $\mathbf{C}_{\text{hy}}$ je hidrodinamična matrika dušenja, $\ddot{\mathbf{u}}$ in $\dot{\mathbf{u}}$ sta vektorja pospeška in hitrost gibanja objekta.

Vzgon in stabilnost

Hidrostatična sila je časovno konstantna in daje mostu potrebno vzgonsko silo. Po Arhimedovem zakonu so hidrostatične sile enake volumnu pontona izpodrinjene vode:

$$\mathbf{F}_{\text{buy}}=\rho g\mathbf{V}_{\text{hull}}\,, \tag{8.5}$$

kjer $\mathbf{F}_{\text{buy}}$ predstavlja navpično silo vzgona, ρ je gostota vode, g je gravitacijski pospešek in $\boldsymbol{V}_{\text{hull}}$ je volumen plavajočega pontona. Projektna zahteva je, da je sila dviga vzgona vedno višja od največje možne kombinacije negativne navpične obremenitve na ponton. Presežene sile vzgona se lahko prevzamejo z napenjanjem kablov v morsko dno, s tem se poveča dinamična stabilnost sistema, prikazanega na sliki 3-11. Hidrodinamična stabilnost pontona je odvisna od pomikov in se pogosto modelira z linearno togostjo $\mathbf{K}_{\text{hy}}$.

Viskozno dušenje

Viskozno dušenje morskih tokov je hidrodinamična sila, ki je posledica podvodnih morskih tokov. Obtežba ima tako statično kot tudi dinamično komponento obtežbe, prikazano na sliki 3-12.

Hidrodinamična sila je definirana na podlagi relativne hitrosti med strukturnim gibanjem in hitrostjo toka $V_{\mathrm{rel}} = V_{\mathrm{stream}} - V_{\mathrm{elem}} f_{\mathrm{int}}$ in je opisana kot:

$$F_{\mathrm{cur}} = \frac{1}{2} \rho C_d D V_{\mathrm{rel}}^{\exp}, \tag{8.6}$$

kjer je ρ gostota vode, C_d koeficient vleka, D presek potopljenega elementa, f_{int} faktor interakcije in $exp = 2$ eksponent hitrosti. Viskozno dušenje ima pomemben vpliv na nizkofrekvenčne odzive horizontalnih nihajnih oblik. Obtežba je prisotna pri vseh potopljenih elementih, kot so pontoni in podvodni pritrdilni kabli.

Reševanje časovnih enačb

Opisane hidrodinamične obtežbe je možno opisati z dinamičnimi enačbami gibanja kot:

$$\begin{aligned}\left(\mathbf{M} + \mathbf{M}_{\mathrm{hy}}(\infty)\right)\ddot{\mathbf{u}} + \mathbf{C}\dot{\mathbf{u}} + \left(\mathbf{K} + \mathbf{K}_{\mathrm{hy}}\right)\mathbf{u} = \mathbf{F}_{\mathrm{buy}} + \mathbf{F}_{\mathrm{wave}}(t) + \frac{1}{2}\rho C_d D\left(V_{\mathrm{stream}} - V_{\mathrm{elem}} f_{\mathrm{int}}\right) \\ - \frac{2}{\pi}\int_0^t \int_0^\infty \mathbf{C}_{\mathrm{hy}}(\omega - \tau)\cos(\omega t - \tau)\dot{\mathbf{u}}(\tau)\, d\omega\, d\tau\end{aligned} \tag{8.7}$$

Konstantne matrike so pomaknjene na levo stran dinamične enačbe in se rešujejo eksplicitno. Nelinearne in frekvenčno odvisne obremenitve so umeščene na desno stran.

8.4 Vetrne obtežbe

Dinamična obtežba vetra je posledica aerodinamičnega upora zraka na konstrukcijo. Vetrne obtežbe se pogosto opišejo kot superpozicija obremenitev I) osrednje vetrne hitrosti, II) turbulence, III) samovzbujajočih sil in IV) vrtinčenja vetra, kar je prikazano na sliki 4-1. Modeliranje sil dinamične obremenitve vetra je možno v skladu s predpostavkami kvazistacionarne (QSS) teorije aerodinamike [54]. Predstavljene formulacije obtežb so primerne za vgraditev v končne elemente linijskih konstrukcij [6]. Popularni model QSS temelji na predpostavki razvitega in stacionarnega vetra okoli prečnega preseka. Bistvena prednost omenjenega modela so enostavni in lažje dostopni aerodinamični parametri. Formulacija je bila vgrajena v aktualne izračune plavajočih mostov s časovno domeno. V poglavju so obravnavane posamezne komponente s poudarkom na samovzbujajočih silah, ki so posledica gibanja mostu. V dinamičnih raziskavah dobro poznani aeroelastični modeli so uspešno uporabljeni v aeroelastičnih analizah omahovanja mostov [25][46] [72]. Meritve v vetrovniku potrjujejo, da aeroelastični modeli natančneje popisujejo interakcijo mostu v primerjavi s poenostavljenimi kvazistacionarnimi modeli. Natančnost se lahko odraža predvsem v natančnejših numeričnih analizah odziva in dodatni možnosti aeroelastične analize omahovanja. V najnovejših raziskavah je razširjena uporaba racionalnih funkcij za interpretacijo odvodov omahovanja v časovni domeni. Matematična formulacija racionalnih funkcij žal ni primerna za uporabo v trenutno predlagani shemi analize dinamike plavajočih mostov. Izpeljanih izrazov ni mogoče vgraditi brez dodatnega programiranja v različne komercialne kode. Raziskava preučuje možnosti uporabe racionalnih funkcij v obstoječi časovni shemi. Za pristop časovne integracije je potrebno pretvoriti frekvenčno odvisne aeroelastične sile v časovno odvisne s postopkom konvolucije. Podobna teoretična ozadja veljajo za transformacijo aeroelastičnih in za transformacijo hidrodinamičnih samovzbujajočih sil, kar pomeni, da obstajajo enake transformacije z različnimi vhodnimi podatki sil. Cilj raziskave je preoblikovanje aeroelastičnih modelov v obliko, primerno za uporabo v hidrodinamični konvoluciji. Posamezne razlike obeh matematičnih pristopov je možno rešiti z razvojem novega aeroelastičnega modela.

Turbulentni veter

Vektor hitrosti vetra se deli na konstantni in časovno spremenljiv turbulentni vektor, definiran kot $\mathbf{U}(t) = \mathbf{V} + \mathbf{v}(t)$. Vetrni vektor je opisan s tremi komponentami, opisanimi v levosučnem kartezičnem koordinatnem sistemu. Tako je smer $u(t)$ vzdolž vetra, $w(t)$ horizontalna in $v(t)$ vertikalna obratna smer gravitacije. V splošnem so dizajnirane lastnosti vetrov odvisne predvsem od orografske pozicije mostov in so pogosto opisane kot funkcije višine, hrapavosti terena v okolici ter izbranega modela. Potrebni podatki za simuliranje vetrne turbulence v prostoru so: osrednja hitrost vetra, turbulenca, spektri, koherence in prostorske koordinate. Na sliki 4-2 je prikazana Fouriereva transformacija vetrnih spektrov v časovno odvisno turbulenco. Poglavje prikazuje način modeliranja turbulence v časovni metodi z uporabo simulacije Monte Carlo kot:

$$\mathbf{v}(t) = \sum_{j=1}^{\mathrm{M}} \sum_{k=1}^{\mathrm{N}} \sqrt{2\Delta\omega}\mathbf{S}_{\mathrm{ij}}(\omega_k)\cos(\omega_k t + \psi_{i,k}). \tag{8.8}$$

$\mathbf{S}_{\mathrm{ij}}(\omega_k)$ je matrika spektrov vozlišč, $\Delta\omega$ frekvenčni korak, ψ naključno število, k predstavlja frekvence, j predstavlja prostorska vozlišča. Vhodni podatki spektralne energije vetrne turbulence, prikazane na sliki 4-3, opisujejo količino energije pri različnih frekvencah. Tako sintetizirani signali prikazanega vhodnega spektra ne reproducirajo natančno, vendar je to možno doseči za povprečno vrednost več simulacij, kar je prikazano na sliki 4-7. Opisana metoda je bila sprogramirana v časovno analizo in je bila prilagojena za izračun vetrne turbulence na 5 km dolge plavajoče mostove. Enačba (8.8) predstavlja precejšen računski izziv, saj bi izračun turbulence trajal kar mesec dni. Glavni razlog za to so razmeroma dolgi računski časi, ki so potrebni za uspešno transformacijo, pogojeno z diskretizacijo časa, frekvence in prostora. Zato je bil koncept izračuna enačbe (8.8) razvit s posebej prilagojenim algoritmom z izboljšavami na več nivojih. Primarno zmanjšanje števila vozlišč je bilo možno z uvedbo ločene vetrne mreže, pri čemer se je izračunana turbulenca projicirala na gosto mrežo končnih elementov mostu, kar je prikazano na sliki 4-4 desno. Takšen pristop omogoča neodvisno število končnih elementov in vozlišč, uporabljenih pri vetrni analizi za natančno transformacijo. Predstavljeni pristop bistveno zmanjša število vozlišč, in sicer s 40000 na 1000, kar kvadratno zmanjša računski čas. Dodatne izboljšave algoritma so bile narejene na interpolaciji frekvenc izračuna korelacijskih spektrov, ki je bil narejen na prej določenih frekvencah. Dodatna optimizacija je bila dosežena z aplikacijo hitrega Fourierevega algoritma, ki omogoča bistveno hitrejši izračun kot klasični Fourierev algoritem. Dodatni paralelni izračun je naknadno pospešil numerične simulacije. Po uvedbi zgoraj opisanih izboljšav se je čas računanja zmanjšal na približno 15 min, kar omogoča učinkovitejši izračun dinamike mostov.

Modeliranje sil

Aerodinamične sile vetra se modelirajo z dimenzionalnimi koeficienti vleka, dviga in momenta. Brezdimenzijska formulacija omogoča prenos sil, izmerjenih v vetrovniku, na realne velikosti mostov. Definicija aerodinamičnih sil izhaja iz Bernoullijeve enačbe primerjave energij zastojne točke tlaka in kinetične energije vetra. Obremenitev vetra je definirana za dolžino segmenta enega metra kot:

$$\mathbf{F}_{\text{mean}} = \frac{1}{2}\rho V^2 B \begin{bmatrix} C_{\text{D}}(\alpha) \\ C_{\text{L}}(\alpha) \\ BC_{\text{M}}(\alpha) \end{bmatrix}, \tag{8.9}$$

kjer je $\mathbf{F}_{\text{mean}}$ vektor vetrne obtežbe, ρ gostota zraka, V laminarna osrednja hitrost vetra in B širina preseka prečnega preseka. Vektor osrednje hitrosti vetra je tako določen na podlagi povprečnega kota α in povprečne hitrosti vetra. Pri dinamični analizi vetra se spreminjata vpadni kot vetra in velikost vektorja hitrosti, sestavljenega iz osrednje hitrosti, turbulentne hitrosti in hitrosti deformacij segmenta. V splošnem lahko formulacijo linearizirano, saj je doprinos kvadratnih vektorjev hitrosti zanemarljiv. Linearizirano formulacijo lahko opišemo kot:

$$\begin{aligned} \mathbf{F}_{\text{buf,lin}} &= \mathbf{F}_{\text{mean}} + \mathbf{F}_{\text{buf}}\mathbf{v}(t) + \mathbf{C}_{\text{qss}}\dot{\mathbf{u}} + \mathbf{K}_{\text{qss}}\mathbf{u} \\ &= \frac{1}{2}\rho V^2 B \begin{bmatrix} C_{\text{D}} \\ C_{\text{L}} \\ BC_{\text{M}} \end{bmatrix} + \frac{\rho V B}{2} \begin{bmatrix} 2C_{\text{D}} & C'_{\text{D}} - C_{\text{L}} \\ 2C_{\text{L}} & C'_{\text{L}} + C_{\text{D}} \\ 2BC_{\text{M}} & BC'_{\text{M}} \end{bmatrix} \begin{Bmatrix} u(t) \\ w(t) \end{Bmatrix} \\ &\quad - \frac{\rho V B}{2} \begin{bmatrix} 2C_{\text{D}} & C'_{\text{D}} - C_{\text{L}} & 0 \\ 2C_{\text{L}} & C'_{\text{L}} + C_{\text{D}} & 0 \\ 2BC_{\text{M}} & BC'_{\text{M}} & 0 \end{bmatrix} \begin{Bmatrix} \dot{u}_{\text{y}} \\ \dot{u}_{\text{z}} \\ \dot{u}_{\text{rx}} \end{Bmatrix} - \frac{\rho V^2 B}{2} \begin{bmatrix} 0 & 0 & C'_{\text{D}} \\ 0 & 0 & C'_{\text{L}} \\ 0 & 0 & BC'_{\text{M}} \end{bmatrix} \begin{Bmatrix} u_{\text{y}} \\ u_{\text{z}} \\ u_{\text{rx}} \end{Bmatrix} \end{aligned} \tag{8.10}$$

Linearna kvazistatična analiza je bila uporabljena za vrsto dinamičnih analiz v dosedanjih študijah izvedljivosti plavajočih mostov [8] [41] [90] [99]. Implementacija v Newmarkovo časovno integracijsko shemo je bila narejena kot:

$$\mathbf{M}\ddot{\mathbf{u}} + \left(\mathbf{C} + \mathbf{C}_{\text{qss}}\right)\dot{\mathbf{u}} + \left(\mathbf{K} + \mathbf{K}_{\text{qss}}\right)\mathbf{u} = \mathbf{F}_{\text{mean}} + \mathbf{F}_{\text{buf}}\mathbf{v}(t). \tag{8.11}$$

Zgoraj prikazano kvazistatično modeliranje interakcije vetra je moč opisati s kvazistatičnimi matrikami dušenja $\mathbf{C}_{\text{qss}}$ in togosti $\mathbf{K}_{\text{qss}}$. Te so teoretična izpeljanka zgoraj opisanega analitičnega modela in so pogosto uporabljene za dinamične vetrne analize. Žal takšno modeliranje odstopa od dejanskih aeroelastičnih meritev v vetrovniku, predvsem za frekvenčno odvisno gibanje mostu. V nadaljevanju je predlagana izboljšava z aeroelastičnimi modeli kot primernejšimi kandidati, ki bi dali natančnejše rezultate odzivov plavajočih mostov [6] [73] [95].

Aeroelastično modeliranje interakcije

Na začetku 20. stoletja je gradnja dolgih visečih mostov nudila stroškovno učinkovito rešitev. Razvita teorija drugega reda je bila ključna za analizo visečih konstrukcij in je omogočala do 30 % prihranka materiala, kar je vodilo do vitkejših mostov. Vitki mostovi so bili precej bolj dovzetni za dinamične vibracije, kar je povzročilo nekaj porušitev mostov. Najbolj odmevna je bila porušitev mostu Tacoma Narrows leta 1940, ki je bila posledica zelo nizke hitrosti vetra, komaj $V = 17\ m/s$. Podrobna preiskava je pokazala, da se je most porušil zaradi takrat še neznanega pojava, ki je povzročil nestabilno nihanje mostu. Osnovna teorija aeroelastike je bila razvita v 60. letih 20. stoletja in je bila posledica razvoja vesoljske industrije. Teorija je bila sprva narejena na osnovi teoretične nestabilnosti aerodinamične plošče in je omogočila raziskavo aeroelastičnih kritičnih hitrosti vetra, poznana je kot Scanlanova teorija nestabilnosti [22]. Vhodni podatki so linearno frekvenčno odvisne funkcije, izražene z brezdimenzijskimi odvodi omahovanja (flutter derivatives). Koeficienti za turbulentne prečne preseke se lahko izmerijo v vetrovniku ali pa se izračunajo s pomočjo računalniške dinamike tekočin (CFD). Aeroelastična formulacija, uporabljena pri preverjanju nestabilnosti omahovanja, je zapisana kot:

$$\mathbf{C}_{\mathrm{se}}(K)\dot{\mathbf{u}} + \mathbf{K}_{\mathrm{se}}(K)\mathbf{u} = -\frac{\rho VBK}{2}\begin{bmatrix} P_1^* & P_5^* & BP_2^* \\ H_5^* & H_1^* & BH_2^* \\ BA_5^* & BA_1^* & B^2A_2^* \end{bmatrix}\begin{Bmatrix} \dot{u}_{\mathrm{y}} \\ \dot{u}_{\mathrm{z}} \\ \dot{u}_{\mathrm{rx}} \end{Bmatrix} - \frac{\rho V^2K^2}{2}\begin{bmatrix} P_4^* & P_6^* & BP_3^* \\ H_6^* & H_4^* & BH_3^* \\ BA_6^* & BA_4^* & B^2A_3^* \end{bmatrix}\begin{Bmatrix} u_{\mathrm{y}} \\ u_{\mathrm{z}} \\ u_{\mathrm{rx}} \end{Bmatrix} \tag{8.12}$$

$K = \omega B/V$ je reducirna frekvenca in $\omega = 2\pi f$ je frekvenca pomikov, odvodi omahovanja predstavljajo vlek P_i^*, vzgon H_i^* in A_i^* moment z indeksom $i = (1,2,...,6)$. Oznaka * označuje odvode omahovanja kot funkcije brezdimenzijske reducirane hitrosti $\hat{V} = K^2 = \omega\mathrm{B}/V$. Meritve v vetrovniku so bile izmerjene z diskretnimi točkami v omejenem območju reduciranih frekvenc, kar zahteva interpolacijo in ekstrapolacijo podatkov. Direktno reševanje enačbe

$$\mathbf{M}\ddot{\mathbf{u}} + \left(\mathbf{C} + \mathbf{C}_{\mathrm{se}}(\omega)\right)\dot{\mathbf{u}} + \left(\mathbf{K} + \mathbf{K}_{\mathrm{se}}(\omega)\right)\mathbf{u} = \mathbf{F}_{\mathrm{mean}} + \mathbf{F}_{\mathrm{buf}}\mathbf{v}(t) \tag{8.13}$$

v časovni domeni ni mogoče, saj vsebuje aeroelastične matrike v odvisnosti od frekvenc. V tej raziskavi je bila raziskana nova možnost formulacije s pomočjo numerične konvolucije preko zgodovine hitrosti z uporabo enakih algoritmov kot pri hidrodinamični analizi gibanja mostu. Predlagani sistem aeroelastičnih matrik je mogoče vključiti v časovno domeno kot:

$$\begin{aligned} &\mathbf{M}\ddot{\mathbf{u}} + \left(\mathbf{C} - \mathbf{C}_{\mathrm{se,v}}^{\infty}\right)\dot{\mathbf{u}} + \left(\mathbf{K} - \mathbf{K}_{\mathrm{se,v}}^{0}\right)\mathbf{u} = \mathbf{F}_{\mathrm{mean}} + \mathbf{F}_{\mathrm{buf}}\mathbf{v}(t) + \\ &\qquad \frac{2}{\pi}\int_0^t\int_0^\infty \left[\mathbf{C}_{\mathrm{se}}(\omega) - \mathbf{C}_{\mathrm{se,v}}^{\infty}\right]\cos\left(\omega(t-\tau)\right)\dot{\mathbf{u}}(\tau)\,d\omega\, d\tau \end{aligned} \tag{8.14}$$

Konstantni matriki $\mathbf{C}_{\mathrm{se,v}}^{\infty}$ in $\mathbf{K}_{\mathrm{se,v}}^{\infty}$ sta podani na levi strani enačbe, frekvenčno odvisna matrika $\left[\mathbf{C}_{\mathrm{se}}(\omega) - \mathbf{C}_{\mathrm{se,v}}^{\infty}\right]$ je pomaknjena na desno stran enačbe. V dosedanjih raziskavah uporabljene interpolacijske funkcije temeljijo na izrazih s teoretično izpeljavo časovnega modela. Iz tega razloga so bile polinomske interpolacije pogosto uporabljane za frekvenčne modele, nikoli pa za časovne. Ker je predlagani format enačbe (8.14) precej splošen in omogoča uporabo številnih novih interpolacijskih funkcij, predstavlja novost na tem področju. Demonstracija uporabe enačbe (8.14) je nadalje izpeljana na primeru interpolacije racionalnih funkcij kot primer parametrične interpolacije, velikokrat uporabljene v raziskavah. V nadaljevanju bodo predstavljene tudi neparametrične interpolacije z uporabo polinomske interpolacije.

Modeliranje aeroelastičnih sil v časovni domeni

Zvezno funkcijo, ki opisuje odvode omahovanja, je možno preoblikovati v časovno odvisno funkcijo. Funkcija mora biti zvezna in mora konvergirati h končni vrednosti. Direktno vrednotenje enačbe (8.12) veljala samo za eno frekvenco harmoničnega gibanja. Z uvedbo superpozicije je možna razširitev veljavnosti za vse periodične ter aperiodične sisteme. Z uporabo Fouriereve transformacije je tako možno izraziti aeroelastične sile v frekvenčni domeni kot produkt prenosne matrike in Fouriereve transformacije pomikov kot $\mathbf{G}_{\mathrm{q}}(\omega) = \mathbf{F}_{\mathrm{se}}(\omega)\mathbf{G}_{\mathrm{u}}(\omega)$. Aeroelastična prenosna matrika je definirana z analitično rešitvijo v frekvenčni domeni, predstavljeni v kompleksni ravnini, in se za odvode omahovanja zapiše kot:

$$\mathbf{F}_{\mathrm{se}}(K) = \frac{1}{2}\rho V^2 \begin{bmatrix} K^2(P_1^* i + P_4^*) & K^2(P_5^* i + P_6^*) & K^2 B(P_2^* i + P_3^*) \\ K^2(H_5^* i + H_6^*) & K^2(H_1^* i + H_4^*) & K^2 B(H_2^* i + H_3^*) \\ K^2 B(A_5^* i + A_6^*) & K^2 B(A_1^* i + A_4^*) & K^2 B^2(A_2^* i + A_3^*) \end{bmatrix}. \tag{8.15}$$

V splošnem poteka transformacija iz frekvenčne domene v časovno v dveh korakih. Najprej se izračuna Fouriereva transformacija prenosne matrike $\mathbf{F}_{\mathrm{se}}$ kot

$$\mathbf{I}_{\mathrm{se}}(t) = \frac{1}{2\pi}\int_{-\infty}^{\infty} \mathbf{F}_{\mathrm{se}}(\omega) e^{i\omega t} d\omega\,, \tag{8.16}$$

kjer je $\boldsymbol{I}_{\mathrm{se}}$ impulzni odziv aeroelastičnih sil. Nato se izračuna konvolucija z integracijo impulzne sile preko celotne zgodovine pomikov

$$\mathbf{q}_{\mathrm{u}}(t) = \int_{-\infty}^{\infty} \mathbf{I}_{\mathrm{se}}(t-\tau)\, \mathbf{u}(\tau) d\tau\,. \tag{8.17}$$

Dobljene aeroelastične sile so tako izračunane v odvisnosti od celotne zgodovine pomikov. Iz enačbe (8.17) je razvidno, da je postopek konvolucije treba izračunati v vsakem koraku, saj se vektor hitrosti spreminja v časovnointegracijski metodi.

Racionalne funkcije

Racionalne funkcije (rational functions) in indicialne funkcije (indicial functions) se običajno uporabljajo za interpoliranje razpršenih meritev odvodov omahovanja. Obe funkciji sta posebej prilagojeni za transformacije v časovno domeno, saj omogočata analitične rešitve. Opremljeni izrazi imajo priročne lastnosti, saj težijo h konstantni vrednosti pri neskončnih frekvencah ∞, kar omogoča analitično rešitev konvolucije. Podrobneje je predstavljen sistem z eno prostostno stopnjo na primeru popularnih racionalnih funkcij, v mnogo raziskavah uporabljen izraz:

$$F_{\mathrm{se}}(K)=\frac{1}{2}\rho V^2(a_1+a_2 iK+a_3(iK)^2+\sum_{l=1}^{N-3}a_{l+3}\frac{iK}{iK+d_l})\,. \tag{8.18}$$

Kadar je a_1 interpolacijski koeficient, je d_l koeficient prileganja pola in N je število izbranih polov. Za praktično uporabo se prilegajo približno od dva do trije poli. Koeficienti v povezavi z vztrajnostjo a_3 so praviloma zanemarjeni. Interpolacijska racionalna funkcija se prilega kompleksnemu vektorju sile, kar zahteva postopek hkratne interpolacije realnih in imaginarnih delov. Nelinearna regresijska interpolacija zahteva učinkovit numerični pristop, ki je povzet v nadaljevanju zapisa. Najprej se izberejo koeficienti a_i, preostali koeficienti pa se izračunajo z linearno regresijo. Nato se z uporabo nelinearne regresije poišče d_l. Tretji korak sledi, ko je dosežen optimalni niz vrednosti d_l, potem se ponovno uporabi nelinearna regresija za iskanje vseh koeficientov hkrati. Ta metoda zahteva kar nekaj pozornosti, saj vsak začetek ne vodi do uspešne konvergence. Prilagajanje izhodiščne vrednosti, parametrov konvergence in komplicirani končni izrazi konvolucije nakazujejo precej zahteven postopek. Za uspešno uporabo prikazanih postopkov so v splošnem potrebne dobre teoretične osnove in osnove nelinearne regresije. Navedeni argumenti predstavljajo pogosto oviro pri uporabi časovnih modelov v praksi in v dosedanjih dinamičnih analizah plavajočih mostov. Po uspešni interpolaciji lahko koeficiente uporabimo v razvitih izrazih. Razvite izraze je mogoče analitično rešiti skladno s postopki Fouriereve transformacije (8.16) in konvolucije preko pomikov (8.17). Dobljen analitični izraz za konvolucijo preko pomikov je:

$$q_{\mathrm{se}}(t)=\frac{1}{2}\rho V^2\Biggl(\underbrace{a_1 u(t)+a_2\frac{B}{V}\dot{u}(t)+\sum_{l=1}^{N-3}a_{l+3}\Bigl(u(t)}_{\text{Neskončni delež }(\infty)}-\frac{d_l V}{B}\underbrace{\int_{-\infty}^{t}e^{\left(-\frac{d_l V}{B}(t-\tau)\right)}u(\tau)\,d\tau}_{\text{Frekvenčno odvisen delež}}\Bigr)\Biggr)\,. \tag{8.19}$$

Izraz ima koeficiente, ki so povezani z neskončnim prispevkom in so rezultat konstantnih vrednosti. Frekvenčni prispevek se izračuna z eksponentnim integralom. Prispevek z neskončnim in frekvenčnim deležem je prikazan na sliki 3-8. Alternativno je aeroelastične sile mogoče izračunati s konvolucijo preko zgodovine hitrosti. Na aeroelastični prenosni matriki, deljeni z vrednostjo $i\omega$, se analogno ponovi matematični postopek transformacije in vodi v izraz:

$$q_{\mathrm{se}}(t)=\frac{1}{2}\rho V^2\Biggl(\underbrace{a_1 u(t)+a_2\frac{B}{V}\dot{u}(t)}_{\text{Neskončni delež }(\infty)}+\sum_{l=1}^{N-3}a_{l+3}\Biggl(\underbrace{\int_{0}^{t}e^{\left(-\frac{d_l V}{B}(t-\tau)\right)}\dot{u}(\tau)\,d\tau}_{\text{Frekvenčno odvisen delež}}\Biggr)\Biggr)\,. \tag{8.20}$$

Nekoliko spremenjen izraz ima tako neskončni delež kot tudi frekvenčno odvisen delež, ki je razrešen z integralom preko zgodovine hitrosti. Izpeljani so tako delitev na neskončne in frekvenčno odvisne deleže kakor tudi razmerja med transformacijami. Predstavljeni izrazi so primerni kandidati za vgraditev v Newmarkovo časovno integracijo. Nadalje je treba izraze spremeniti v izraze, ki jih bo mogoče vgraditi v dosedanje sheme dinamične analize plavajočih mostov, predstavljene v tem delu.

Novi postopek

Predstavljen je nov izračun aeroelastičnih sil s postopkom numerične transformacije aeroelastičnih sil v časovno domeno. Glavni namen razvitega postopka je možnost vgradnje v do zdaj uporabljeno integracijsko shemo. Prednost razvitega postopka so dodatne možnosti uporabe različnih interpolacijskih funkcij, kot so polinomi, kubični zlepki, racionalne funkcije, povprečna interpolacija itd. Teh ni bilo mogoče uporabiti z do zdaj opisanimi postopki, saj so vse interpolacijske funkcije morale imeti analitično rešitev. Ideja numerične transformacije prihaja iz hidrodinamičnega modeliranja in predstavlja tudi ciljno končno formulacijo izrazov. Za uporabljene interpolacijske funkcije velja, da zavzemajo zvezne numerične vrednosti. Tako interpolirane vrednosti tvorijo prenosno aeroelastično funkcijo, sestavljeno iz neskončnega in frekvenčno odvisnega dela. Neskončni deli imajo analitično rešitev, frekvenčno odvisni deli pa so izračunani z numerično transformacijo v časovno domeno, saj analitična rešitev ni mogoča. Poskrbljeno mora biti, da interpolacijske vrednosti konvergirajo h končni vrednosti, kar je mogoče naknadno doseči z numerično korekcijo ekstrapoliranih vrednosti. Tako razvit postopek je bil razvit v konvolucijo preko pomikov:

$$q(t)=\frac{1}{2}\rho V^2\left(K_{\mathrm{se,u}}^{\infty}u(t)+C_{\mathrm{se,u}}^{\infty}\dot{u}(t)+\frac{2}{\pi}\int_0^t\int_0^\infty\left[K_{\mathrm{se}}(\omega)-K_{\mathrm{se,u}}^{\infty}\right]\cos\left(\omega(t-\tau)\right)u(\tau)d\omega d\tau\right). \tag{8.21}$$

in hkrati v izraz za konvolucijo preko hitrosti:

$$q(t)=\frac{1}{2}\rho V^2\left(K_{\mathrm{se,v}}^{0}u(t)+C_{\mathrm{se,v}}^{\infty}\dot{u}(t)+\frac{2}{\pi}\int_0^t\int_0^\infty\left[C_{\mathrm{se}}(\omega)-C_{\mathrm{se,v}}^{\infty}\right]\cos\left(\omega(t-\tau)\right)\dot{u}(\tau)d\omega d\tau\right). \tag{8.22}$$

Prikazana je teoretična izpeljava zgornjih izrazov, ki temelji na teoriji realnih dinamičnih sistemov. Narejene predpostavke so skladne s postavkami, narejenimi pri razvoju racionalnih funkcij. Izraza (8.22) in (8.25) se lahko uporabita za modeliranje tako parametričnih kot neparametričnih interpolacijskih funkcij. Za demonstracijo je prikazan primer parametričnega modeliranja racionalnih funkcij z vstavljanjem

$$\begin{gathered}K_{\mathrm{se,u}}^{\infty}=a_1+\sum_{l=1}^{N-3}a_{l+3}\\ C_{\mathrm{se,u}}^{\infty}=a_2\frac{B}{V}\\ \left[K_{\mathrm{se}}(\omega)-K_{\mathrm{se,u}}^{\infty}\right]=\sum_{l=1}^{N-3}a_{l+3}\frac{-d_l^2}{K^2+d_l^2}\end{gathered} \tag{8.23}$$

v nov postopek numerične konvolucije preko pomikov (8.21). Dobimo enak rezultat kot za analitično rešitev racionalnih funkcij v enačbi (8.19). Enakost velja za vstavljene izraze

$$\begin{gathered} K^0_{\text{se,v}} = a_1 \\ C^\infty_{\text{se,v}} = a_2 \frac{B}{V} \\ \left[C_{\text{se}}(\omega) - C^\infty_{\text{se,v}} \right] = \sum_{l=1}^{N-3} a_{l+3} \frac{B}{V} \frac{d_l}{K^2 + d_l^2} \end{gathered} \tag{8.24}$$

v nov postopek numerične konvolucije preko hitrosti (8.22) dobimo enak rezultat kot za analitično rešitev racionalnih funkcij v enačbi (8.20). Vsi štirje izrazi analitične in nove numerične rešitve so bili testirani numerično in dajejo povsem enak rezultat, kar dokazuje pravilno izpeljane izraze.

Posebej pomembna teoretična izpeljava simetrije realnih dinamičnih sistemov opisuje razmerje med zveznim frekvenčno odvisnim dušenjem ter frekvenčno odvisno togostjo, izraženo kot:

$$\int_0^\infty \left(\left[C_{\text{se}}(\omega) - C^\infty_{\text{se}} \right] \cos(\omega t) \right) d\omega = \int_0^\infty \left(\frac{1}{\omega} \left[K_{\text{se}}(\omega) - K^0_{\text{se}} \right] \sin(\omega t) \right) d\omega \, . \tag{8.25}$$

To velja tudi za zvezni opis odvodov omahovanja. Razmerje je bilo v nadaljevanju dokazano na primeru racionalnih funkcij in tudi za poljubno interpolacijsko funkcijo. Razmerje je veljavno tako v posameznih meritvah kot tudi v korespondenčnih interpolacijah. Dokaz je osnova za nadaljnji razvoj neparametričnega modeliranja aeroelastičnih sil s poljubnimi interpolacijskimi funkcijami. To omogoča neodvisno interpolacijo aeroelastičnega dušenja in aeroelastične togosti ter uporabo polinomske linearne regresije. Polinomske interpolacije višjih redov lahko divergirajo zunaj razpoložljivih podatkov, zato se ekstrapolacije korigirajo z zvezno funkcijo prehoda. Zvezna korekcija se lahko opravi z izrazom

$$B(\omega) = \frac{1}{1 - \exp\left(-2k(\omega - \omega_n)\right)} \tag{8.26}$$

za območja ekstrapolacij. Neskončne konstantne vrednosti so lahko določene v višini vrednosti zadnjih razpoložljivih interpolacijskih podatkov. Sprememba je potrebna pri vseh divergentnih interpolacijskih funkcijah in je lahko opravljena numerično. Bistvena prednost neparametričnega modeliranja je izognitev nelinearni regresiji in s tem bistveno poenostavljen postopek modeliranja.

Vrednotenje aeroelastičnih modelov

Poleg numeričnih simulacij, izvedenih v tej raziskavi, so bili narejeni tudi laboratorijski preizkusi v vetrovniku na trondheimski univerzi na Norveškem [59]. Predstavljeni so podatki za aerodinamični presek mostu Hardanger na Norveškem [71]. Prerez je bil pomanjšan v razmerju 1 : 50, nanj so bili pritrjeni detajli ograj. Vetrovnik ima moderen servomehanizem, ki lahko generira različna gibanja segmenta mostu in hkrati meri aeroelastično silo, kar je prikazano na sliki 4-10. Najprej so bili narejeni harmonični vsiljeni pomiki pri različnih reduciranih hitrostih za izračun odvodov omahovanja. Diskretne točke so bile nato interpolirane z racionalnimi funkcijami kot predstavniki parametričnega modela, kjer sta bila uporabljan dva pola N=2 za dobro natančnost. Prileganji posameznih interpolacijskih krivulj sta prikazani na sliki 4-12 in sliki 4-13, kjer je vidno zelo dobro prileganje obeh krivulj. Razlike je možno opaziti v ekstrapolacijskih vrednostih, ki niso del testiranja in posledično nimajo vpliva na rezultate. V splošnem je točnost izmerjenih odvodov omahovanja neposredno odvisna od točnosti meritev, načina preizkusa in vetrovnika. Pomembna lastnost v tej raziskavi uporabljenih odvodov omahovanja je izredno nizek raztros posameznih meritev, kar naznanja dobro izmerjene in reprezentativne odvode omahovanja. Nadaljnje testiranje je bilo narejeno na primeru večharmonskega odziva, kjer so bile izmerjene aeroelastične sile v spektru pomikov med 0,25 in 2,5 Hz z amplitudami 16 mm in 2,4°. Gre za najzahtevnejši test aeroelastičnih modelov, ki ga je možno rešiti le z ustrezno modeliranimi frekvenčno odvisnimi silami. Gibanje segmenta je simulirana superpozicija naključno izbranih faz, amplitud in frekvenc in je prikazano na sliki 4-15. Preizkus posameznih modelov je bil sestavljen iz treh faz testiranja:

1. faza je numerično primerjala analitične izraze (8.19) in (8.20) ter nova numerična postopka (8.21) in (8.22). Za vhodne podatke vseh modelov so bile uporabljene racionalne funkcije. Časovno odvisni rezultati se povsem ujemajo in so prikazani na sliki 4-14. To potrjuje pravilno matematično formulacijo in implementacijo modelov.
2. faza je primerjala parametrični model racionalnih funkcij in neparametrični model individualne polinomske interpolacije ter ju primerjala z meritvami iz vetrovnika. Na sliki 4-16 je prikazano dobro ujemanje sil dviga in momenta, kar potrjuje primernost neparametričnih modelov. Sila vleka se ne ujema za vse modele zaradi nelinearne karakteristike, zato so linearni modeli neprimerni.
3. faza je numerično testiranje v programskih jezikih *MATLAB* in *RM Bridge*, ki je primerjano z rezultati iz vetrovnika. Obe kodi se dobro ujemata z meritvami v skladu s teorijo.

8.5 Frekvenčna analiza

Tehnike modalne dekompozicije so široko uporabljane in priljubljene v različnih inženirskih disciplinah. Poleg prikazanih časovnih metod integracije ponujajo dodaten vpogled v razumevanje odziva mostu, informacijo o najpomembnejših frekvencah, nihajnih oblikah in participacije mase. Rezultate je enostavno interpretirati in ne potrebujejo dodatne statistične obdelave časovnih signalov. Frekvenčne metode so v primerjavi s časovno domeno precej manj računsko potratne. To poglavje ponuja kratko predstavitev metode linearne modalne dekompozicije, v nadaljevanju imenovane frekvenčna metoda. Frekvenčna metoda je bila uporabljena pri končni primerjavi rezultatov s časovno metodo in tako uporabljena za odkrivanje morebitnih napak pri implementaciji dinamičnih obtežb. Podan je postopek modalne dekompozicije, ki je bil narejen upoštevajoč zunanje vplive vseh obtežb okolja. Predlagani postopek dekompozicije je izveden v dveh korakih. Prvi korak je dekompozicija mostu skupaj s frekvenčno odvisno hidrodinamično maso, drugi korak pa modeliranje preostalih obtežb okolja. Nelinearni sistem mostu je aproksimiran s tangentno togostjo $\mathbf{K}_{\mathrm{nl}}$, ki je posledica velikih deformacij mostu pod stalnimi obtežbami. Za linearizirani sistem je mogoče izračunati lastne vrednosti plavajočih sistemov kot:

$$\left[\left(\mathbf{K}_{\mathrm{nl}}+\mathbf{K}_{\mathrm{hy}}\right)-\omega^{2}\left(\mathbf{M}+\mathbf{M}_{\mathrm{hy}}(\omega)\right)\mathbf{u}(t)\right]\boldsymbol{\phi}=0\,. \tag{8.27}$$

Ker so prispevki hidrodinamične mase relativno veliki, je treba zajeti maso pri posameznih frekvencah, zato je postopek izračuna frekvence iterativen in podan s shemo na sliki 5-1. Tako pridobljene lastne vrednosti so primerne za izračun v drugem koraku izračuna interakcije preostalih obtežb, ki predstavljajo obtežbo in hkrati spreminjajo dinamične karakteristike mostu. Dodane obtežbe so v splošnem nesimetrične vezane dinamične enačbe, ki jih ni mogoče razrešiti s klasičnimi lastnimi tehnikami realne vrednosti. Predstavljen je sistem lastnih vrednosti nesimetričnih vezanih dinamičnih enačb, ki daje kompleksne vrednosti modalnih vektorjev:

$$\boldsymbol{\phi}^{\mathrm{T}}\mathbf{M}_{\mathrm{s+hy}}\boldsymbol{\phi}\ddot{\boldsymbol{\eta}}+\boldsymbol{\phi}^{\mathrm{T}}\left(\mathbf{C}_{\mathrm{s}}-\mathbf{C}_{\mathrm{curr}}-\mathbf{C}_{\mathrm{hy}}\left(\omega\right)-\mathbf{C}_{\mathrm{se}}\left(\omega\right)\right)\boldsymbol{\phi}\dot{\boldsymbol{\eta}}+\boldsymbol{\phi}^{\mathrm{T}}\left(\mathbf{K}_{\mathrm{nl+hy}}-\mathbf{K}_{\mathrm{se}}\left(\omega\right)\right)\boldsymbol{\phi}\boldsymbol{\eta}=\boldsymbol{\phi}^{\mathrm{T}}\mathbf{F}_{\mathrm{env}}\,. \quad (8.28)$$

Na desni strani enačbe so obtežbe valov in vetra, na levi strani so interakcijske vrednosti spremembe dušenja in togosti. V poglavju je prikazan postopek izračuna deležev posameznih matrik interakcije in nakazan postopek reševanja enačb. Prikazan je primer postopka izračuna nestabilnosti omahovanja pri naraščajočih hitrostih vetra. Podan je tudi pregled postopka dinamičnega izračuna vetrne obtežbe, uporabljenega v naslednjem poglavju.

8.6 Primer plavajočega visečega mostu

Prikazan je praktični primer dinamične analize iz študije izvedljivosti plavajočega mostu. Študija izvedljivosti je bila izvedena za 5 km širok fjord Bjørnafjorden z morskim dnom na globini 0,6 km. Predstavljeni primer visečega mostu s temeljenjem »Tension Leg Platform« prikazuje atraktivno premostitev. Koncept mostu je bil razvit v sodelovanju med NPRA in skupino svetovalcev: Aas-Jakobsen, COWI, Johs Holt, Moss Maritime, Wind OnDemand, Aker Solutions, NGI in Plan arkitekter. Posebna pozornost je bila namenjena kombiniranim vplivom dinamičnega vzbujanja različnih obtežb, ki so bili predmet preučevanja omenjenih raziskav. Ta disertacija ponuja pregled različnih dinamičnih obremenitev na plavajoče mostove. Zaradi kompleksnosti vseh obtežb in samega primera je bila narejena demonstracija za najbolj dominantno obtežbo vetra. Pri analizi sta bili upoštevani kvazistatična interakcija in radiacija valov:

$$\begin{aligned}\left(\mathbf{M}+\mathbf{M}_{\mathrm{hy}}\left(\infty\right)\right)\ddot{\mathbf{u}}+\left(\mathbf{C}+\mathbf{C}_{\mathrm{hy}}\left(\omega\right)+\mathbf{C}_{\mathrm{qss}}\right)\dot{\mathbf{u}}+\left(\mathbf{K}_{\mathrm{nl}}+\mathbf{K}_{\mathrm{hy}}+\mathbf{K}_{\mathrm{qss}}\right)\mathbf{u}=&\\ \mathbf{F}_{\mathrm{perm}}+\mathbf{F}_{\mathrm{buf}}\left(t\right)&\end{aligned} \quad (8.29)$$

Rezultati dinamičnega odziva mostu so prikazani na sliki 6-7 in sliki 6-8. Iz rezultatov je razvidno, da gre za dobro ujemanje v horizontalni in srednje dobro ujemanje v vertikalni smeri. Bistveno natančnejša časovna domena daje možnost vpogleda v nelinearnost sistema. Zaključen primer ponazarja pomembnost časovne integracije pri nelinearni analizi plavajočih mostov. Možnosti vgraditve aeroelastičnih modelov bi lahko nadalje izboljšale natančnost odzivov, kar je prikazano v tej raziskavi.

8.7 Zaključek

Predstavljeno modeliranje okolijskih obremenitev je bilo uspešno vgrajeno v časovno integracijo odziva mostov. Newmarkova integracijska shema je primerna za reševanje vezanih nelinearnih dinamičnih enačb gibanja. Različne obremenitve so bile dodane k dinamičnim enačbam in so na razpolago za nadaljnje inženirsko in raziskovalno delo. Razvoj modelov je spremljalo intenzivno testiranje razvitih modelov. Raziskave so potekale vzporedno z delom v praksi, ki je omogočalo vpogled v izzive inženirsko zahtevnega področja in možnost izboljšav. Sam razvoj plavajočih mostov in spremljajočih metod predstavlja pionirsko delo in je sad večletnega dela več skupin.

Glavni cilji raziskave so bili uspešno doseženi z raziskovalno nalogo, za vse obtežbe valov in vetra so bili uspešno vgrajeni v časovnointegracijsko metodo. Testiranje je potekalo vzporedno z različnimi študijami izvedljivosti. Trenutno vgrajeni model kvazistatične interakcije vetra je bil vgrajen v časovno domeno in ponuja sprejemljivo natančnost v zgodnjih fazah študije izvedljivosti. Izveden je bil glavni cilj študije, ki prikazuje primernost aeroelastičnih modelov v uporabljeni časovnointegracijski shemi. Cilj je bil dosežen z uvedbo novega postopka numerične konvolucije, ki omogoča simuliranje aeroelastičnih sil brez dodatnih posegov v komercialne kode, s čimer je bila potrjena hipoteza. Primer interpolacije aeroelastičnih sil z racionalnimi funkcijami je bil demonstriran v uporabljeni časovni shemi. Prikazan je nov način modeliranja aeroelastičnih sil z neparametričnim interpoliranjem, ki predstavlja pomemben znanstveni prispevek. Primer polinomske interpolacije bistveno poenostavi postopek, saj omogoča linearno regresijo in nadomešča težavne nelinearne regresijske sheme. Primera racionalne funkcije in polinomske interpolacije sta bila testirana v vetrovniku in dajeta spodbudne rezultate za nadaljnjo uporabo predstavljenih modelov v časovni shemi.

Ta raziskava odpira vrata natančnejšim aeroelastičnim modelom za direktno apliciranje v projekte plavajočih mostov. Predstavljene izboljšave bodo omogočile takojšnje povratne informacije o aeroelastičnih lastnostih in so bistvene za učinkovito zasnovo mostu. Razviti modeli lahko omogočajo natančen dinamični izračun, ki vodi do ekonomično oblikovanega mostu. Delo zainteresiranemu bralcu ponuja vrsto referenc, uporabljenih pri raziskovanju, z navdihujočimi plavajočimi mostovi.

9 REFERENCES

[1] StatensVegvesen, "The E39 Coastal Highway Route," June 2018. [Online]. Available: https://www.vegvesen.no/en/roads/Roads+and+bridges/Road+projects/e39coastalhighwayroute.

[2] *RMBridgeAdvancedSoftware.* [Performance]. Bentley Systems, 2018.

[3] BentleySystems-Austria, "Final Report: Wind buffeting in time domain," Graz, 2016.

[4] BentleySystems-Austria, "FAQ: Buffeting analysies theory - Dynamic Wind Analysis Buffeting," Graz, 2013.

[5] E. D. Newland, Random Vibrations, Spectral & Wavelet Analysis, Third edition, New York: Dover Books Engineering, 2016.

[6] O. Øiseth, A. Rönnquist and R. Sigbjörnsson, "Finite element formulation of the self-excited forces for time-domain assessment of wind-induced dynamic response and flutter stability limit of cable-supported bridges," *Finite Elements in Analysis and Design,,* vol. 50, p. 173–183, 2012.

[7] BentleySystems-Austria, "RM Bridge Customization: Implementation of Hydro-dynamics Features RM Bridge," Graz, 2015.

[8] J. Stampler, J. Sello, M. Papinutti, A. Bruer, M. H. Marley, J. Veie and S. H. Holtberget, "Prediction of Wave and Wind induced Dynamic Response in Time Domain using RM Bridge," in *IABSE Conference*, Geneva, 2015.

[9] J. Newman, Marine hydrodynamics, The MIT press, 1977.

[10] A. multiphisics, "Workbench, COWI," Ansys, USA, 2018.

[11] A. Rahman, "Dynamic Analysis of Floating Bridges," *Procedia Engineering,* vol. 194, pp. 44-50, 2017.

[12] K. A. Kvåle, O. Øiseth, A. Rønnquist and R. Sigbjornsson, "Modal Analysis of a Floating Bridge Without Side-Mooring," *Dynamics of Civil Structures,* vol. 2, pp. 127-136, 2015.

[13] T. Viuff, B. J. Leira, X. Xiang and O. Øiseth, "Dynamic Response of a Floating Bridge Structure," *IABSE Congress in Stockholm,* 2016.

[14] F. I. G. Giske, B. J. Leira and O. Øiseth, "Stochastic Modelling of Wave Loads on Floating Bridges: Efficient Calculation of Cross-Spectral Densities," *IABSE Congress at Stockholm,* 2016.

[15] Y. Xu, O. Øiseth and T. Moan, "Time Domain Modelling of Frequency Dependent Wind and Wave Forces on a Three-Span Suspension Bridge With Two Floating Pylons Using State Space Models," *ASME International Conference on Ocean, Offshore and Arctic Engineering,* vol. 36, 2017.

[16] Y. Xu, O. Øiseth and T. Moan, "Time domain simulations of wind-and wave-induced load effects on a three-span suspension bridge with two floating pylons," *Marine Structures,* vol. 58, pp. 434-452, 2018.

[17] X. Xiang, T. Viuff, B. J. Leira and Ø. Ole, "Impact of Hydrodynamic Interaction Between Pontoons on Global Responses of a Long Floating Bridge Under Wind Waves," *ASME International Conference on Ocean, Offshore and Arctic Engineering,* vol. 37, 2018 .

[18] T. Viuff, X. Xiang, B. J. Leira and O. Øiseth, "Code-to-Code Verification of End-Anchored Floating Bridge Global Analysis," *ASME International Conference on Ocean, Offshore and Arctic Engineering,* vol. 37, 2018.

[19] Y. Xu, O. Øiseth, T. Moan and A. Naess, "Prediction of long-term extreme load effects due to wave and wind actions for cable-supported bridges with floating pylons," *Engineering Structures ,* vol. 172, pp. 321-333.

[20] T. Viuff, B. J. Leira, X. Xiang and O. Øiseth, "Effects of wave directionality on extreme response for a long end-anchored floating bridge," *Applied Ocean Research,* vol. 90, 2019.

[21] T. Viuff, X. Xiang, B. J. Leira and O. Øiseth, "Software-to-Software Comparison of End-Anchored Floating Bridge Global Analysis," *Journal of Bridge Engineering,* vol. 25, no. 5, p. 14, 2020.

[22] R. H. Scanlan and J. J. Tomko, "Airfoil and Bridges Deck Flutter Derivatives.," *Journal of the Engineering Mechanics Division (ASCE),* vol. 97, p. 1717–1737, 1971.

[23] R. H. Scanlan, "The action of flexible bridges under wind, II: Buffeting theory," *Journal of Sound and Vibration,* no. 2, p. 60, 1978.

[24] Y. H. Farsani, T. D. Valentine, A. Arena, W. Lacarbonara and P. Marzocca, "Indicial functions in the aeroelasticity of bridge decks," *Journal of Fluids and Structures,* vol. 48, pp. 203-215, 2014.

[25] O. Øiseth, A. Rönnquist and R. Sigbjørnsson, "Simplified prediction of wind-induced response and stability limit of slender long-span suspension bridges, based on modified quasi-steady theory: A case study," *Journal of Wind Engineering and Industrial Aerodynamics,* vol. 98, no. 12, p. 730–741., 2010.

[26] StatensVegvesen, "Bjonafjord final report," Oslo, 2017.

[27] T. J. R. Hughes, The Finite Element Method: Linear Static and Dynamic Finite Element Analysis, US, 2000.

[28] N. M. Newmark, "A method of computation for structural dynamics.," *Journal of Engineering Mechanics,* vol. 85, pp. 67-94., 1959.

[29] StatensVegvesen, "Bjørnafjorden Suspension Bridge - K1 & K2 Environmental Load Analysis Report," Oslo, 2017.

[30] P. Boccotti, Wave Mechanics and Wave Loads on Marine Structures, USA: Elsevier, 2015.

[31] Z. Cheng, Z. Gao and M. T., "Hydrodynamic load modeling and analysis of a floating bridge in homogeneous wave conditions," *Marine Structures,* vol. 59, pp. 122-141, 2018.

[32] DNV, "Recommended Practice, Environmental conditions and environmental loads," Det Norske Veritas, Oslo, 2007.

[33] DNV, "Recommended Practice, Environmental conditions and environmental loads," Det Norske Veritas, Oslo, 2017.

[34] metocean, "http://www.metocean.co.nz/news/2018/8/24/metocean-solutions-wavespectra-library-finalist-for-new-zealand-open-source-awards," Met Ocean Solutions, 12 December 2018. [Online].

[35] StatensVegvesen, "Bjørnafjorden Suspension Bridge - K1 & K2 Hydrodynamic Model Test Report," Oslo, 2017.

[36] StatensVegvesen, "Bjørnafjorden Suspension bridge - K1 & K2 Hydrodynamic Analysis Report," Oslo, 2017.

[37] "Sintef," June 2018. [Online]. Available: https://www.sintef.no/en/.

[38] StatensVegvesen, "Bjørnafjorden Suspension Bridge - K1 & K2 Hydrodynamic Hull Design Report," Oslo, 2017.

[39] R. Taghipour, T. Perez and T. Moan, "Time-domain hydroelastic analysis of a flexible marine structure using state-space models," *Journal of Offshore Mechanics and Arctic Engineering,,* 2009.

[40] T. Fossen, Marine Craft Hydrodynamics and Motion Control, Trondheim: Wiley, 2014.

[41] M. Papinutti, J. Sello, A. Bruer, M. H. Marley, J. Veie and S. H. Holtberget, "Comparison of Alternative Floater concepts for a 2-span Suspension Bridge supported by a Tension Leg Platform," in *IABSE Congress Stockholm*, Stockholm, 2016.

[42] J. Holmes, "Wind Loading on Structures," *Taylor&Francis,* 2007.

[43] L. T. Hoa, "Time Domain numerical buffeting response prediction - I.Theory," 2005.

[44] E. Cheynet, J. B. Jakobsen and J. Snæbjörnsson, "Buffeting response of a suspension bridge in complex terrain," *Engineering Structures,* p. 474–487, 2016.

[45] J. M. W. Brownjohn, M. Bocciolone, A. Curami, M. Falco and A. Zasso, "Humber bridge full-scale measurement campaigns 1990-1991," *Journal of Wind Engineering and Industrial Aerodynamics,* vol. 52, p. 185–218, 1994.

[46] A. Fenerc and O. Øiseth, "Measured Buffeting Response of a Long-Span Suspension Bridge Compared with Numerical Predictions Based on Design Wind Spectra," *Journal of Structural Engineering ,* vol. 9, p. 143, 2017.

[47] G. Diana, "Messina bridge project-Technical challenges," Mokpo, 2006.

[48] "Wind tunnels and experimental fluid-dynamics research," [Online]. Available: http://www.google.at/url?sa=i&source=images&cd=&cad=rja&docid=MYu6TW_6k9924M&tbnid=lT4Xjd0jOJNmAM:&ved=0CAgQjRwwAA&url=http://www.intechopen.com/

books/wind-tunnels-and-experimental-fluid-dynamics-research/tall-buildings-under-multidirectional-winds-respon.

[49] A. Naess and O. Gaidai, "Estimation of extreme values from sampled time series," *Structural Safety,* vol. 31, no. 4, pp. 325-334, 2009.

[50] J. Bietry, D. Delaunay and E. Conti, "Comparison of full-scale measurement and computation of wind effects on a cable-stayed bridge," 1995.

[51] G. Solari and G. Piccardo, "Probabilistic 3-D turbulence modeling for gust buffeting of structures," *Probabilistic Engineering Mechanics,* vol. 16, p. 73–86, 2001.

[52] S. Hansen, M. Lollesgaard, S. Rex, J. Jacobsen and E. Hansen, "The Hardanger Bridge: Static and Dynamic Wind Tunnel Tests with A Section Model," p. Copenhagen, 2006.

[53] K. Aas-Jakobsen and E. Strømmen, "Time domain buffeting response calculation of slander structures," *Jurnal of Wind Engineering and Industrial Aerodynamics,* vol. 89, no. 5, pp. 341-364, 2001.

[54] S. Einar, Theory of Bridge Aerodynamics, 2nd edition, Norway, 2010.

[55] A. G. Davenport, "Buffeting of a suspension bridge by storm winds," *Journal of structural Division,* p. 233–268, 1962.

[56] A. Bentely Systems, Final Report: Wind buffeting in time domain, RM Bridge Advanced, Bentley Systems Austria, 2016.

[57] T. Von Kármán, "Progress in the Statistical Theory of Turbulence," *Proceedings of the National Academy of Sciences. ,* p. 530–539, 1948.

[58] COWI, Mathias Marley, MATLAB scripts, Norway, 2016.

[59] StatensVegvesen, "Medocean wave report for Bjornafjorden," Oslo, 2017.

[60] StatensVegvesen, "N400 Handbook for bridge design," StatensVegvesen, Oslo, 2009.

[61] Y. Meyer, Wavelets and Operators. Cambridge, Cambridge : Cambridge University Press., 1992.

[62] Y. L. Xu, Wind Effects on Cable-Supported Bridges., John Wiley & Sons, 2013.

[63] Y. Fujino, K. Kimura and T. H., Wind Resistant Design of Bridges in Japan, Developments and practice, New York: Springer, 2012.

[64] L. Caracoglia and N. P. Jones, "Time domain vs. frequency domain characterization of aeroelastic forces for bridge deck sections.," *Journal of Wind Engineering and Industrial Aerodynamics,* vol. 91, no. 3, p. 371–402, 2003.

[65] X. Chen and A. Kareem, "Nonlinear response analysis of long-span bridges under turbulent winds," *Journal of Wind Engineering and Industrial Aerodynamics,* vol. 89, no. 14–15, pp. 1335-1350, 2001.

[66] X. Chen, A. Kareem and M. Matsumoto, "Multimode coupled flutter and buffeting analysis of long span bridges.," *Journal of Wind Engineering and Industrial Aerodynamics,* p. 649–499, 2001.

[67] M. Guido, "Fluid-Structure Interaction in Bluff-Body Aerodynamics and Long Span Bridge Design: Phenomena and Methods," in *Magdalene Collage*, Cambridge, 2000.

[68] M. Papinutti, J. K. Stajnko and R. Jecl, "Aeroelastična analiza mostov s pomočjo modernih orodij računalniške dinamike tekočin," in *Slovensko Društvo za mehaniko*, Rogaška slatina, 2013.

[69] M. Papinutti, J. K. Stajnko, R. Jecl, A. Štrukelj, M. Zadravec and J. A. Jurado, "Assessment of flutter speed on the long span bridges," in *Fluid structure interaction*, London, 2013.

[70] B. Siedziako, O. Øiseth and A. Rönnquist, "A new setup for section model tests of bridge decks," *Proceedings of 12th UK Conference on Wind Engineering, Nottingham,* p. 11–14, 2016.

[71] *NTNU - Norges teknisk-naturvitenskapelige universitet,* 2018.

[72] O. Øiseth, A. Suyuthi, B. Leira, K. M. Mathisen, A. Rönnquist, R. Sigbjörnsson and S. Remseth, "Prediction of wave inducted dynamic response in time domain using the finite elementh method," Strait crossing, Trondheim, 2016.

[73] O. Øiseth, A. Rönnquist and R. Sigbjörnsson, "Time domain modeling of self-excited aerodynamic forces for cable-supported bridges: A comparative study," *Computers and Structures,* vol. 89, p. 1306–1322, 2011.

[74] O. Øiseth and R. Sigbjornsson, "An alternative analytical approach to prediction of flutter stability," *JournalofSoundandVibration,* vol. 330, p. 2784–2800, 2011.

[75] O. Øiseth, A. Rønnquist and R. Sigbjornsson, "Simplified prediction of wind-induced response and stability limit of slender long-span suspension bridges, based on modified quasi-steady theory," *Journal of Wind Engineering and Industrial Aerodynamics,* vol. 98, no. 12, pp. 730-741, 2011.

[76] R. H. Scanlan and T. J. J., "Airfoil and bridge deck flutter derivatives," *Journal of Engineering,* pp. 1717-1737, 2010.

[77] C. Costa and C. Borri, "Application of indicial functions in bridge deck aeroelasticity.," *Journal of Wind Engineering and Industrial Aerodynamics,* vol. 94, pp. 859-81, 2016.

[78] C. Costa, C. Borri, O. Flamand and G. Grillaud, "Time-domain buffeting simulations for wind-bridge interaction," *Journal of Wind Engineering and Industrial Aerodynamics,* p. 991–1006, 2007.

[79] J. P. Hespanha, Linear Systems Theory, New Jersey: Princeton University Press, 2009.

[80] Y. Tamura and A. Kareem, Advanced Structural Wind Engineering, New York: Springer, 2013.

[81] L. Salvatori and C. Borri, "Frequency- and time-domain methods for the numerical modeling of full-bridge aeroelasticity," *Computers & Structures,* vol. 85, pp. 675-87, 2007.

[82] B. Siedziako, O. Øiseth and A. Rønnquist, "An enhanced forced vibration rig for wind tunnel testing of bridge deck section models," *Journal of Wind Engineering & Industrial Aerodynamics,* 2017.

[83] E. Simiu and R. H. Scanlan, "Winds Effects on Structures: Fundamentals and Applications to Design," *Wiley,* 1996.

[84] X. Chen, M. Matsumoto and A. Kareem, "Time domain Flutter and Buffeting response Analysies of Bridges," in *Journal of engineering mechanics*, 2000.

[85] Y. Xu, O. Øiseth and T. Moan, "Time domain simulations of wind- and wave-induced load effects on a three-span suspension bridge with two floating pylons," *Marine Structures,* vol. 58, pp. 434-452, 2018.

[86] M. Papinutti, A. Bruer, M. H. Marley and J. Kvaleid, "A frequency domain tool for investigation of wind response of TLP suspension bridges," in *IABSE Symposium*, Vancouver, 2017.

[87] A. Hernandez, F. Nieto, A. Baldomir and J. A. Jurado, "Some chalanges on the aeroelatic analysies and design of long span bridges," in *Fluid structure interaction conference,*, Gran Canaria, 2012.

[88] J. J. A. and H. S., "Theories of Aerodynamic forces on deck of long span Bridges," *Jurnal of Bridge engineering,* pp. 18-13, 2000.

[89] J. A. Jurado, S. Hernandez, F. Nieto and A. Mosquera, Bridge Aeroelasticity, La Coruna: WIT Press, 2011.

[90] M. Papinutti, Wind load on cable-stayed and suspension bridges - Master thesis, Maribor: University of maribor, 2013.

[91] W. OnDemand, "Software engineering and wind consultancy services," Mitja Papinutti, Graz, 2018.

[92] O. Øiseth, A. Rönnquist, A. Naess and R. Sigbjörnsson, "Estimation of extreme response of floating bridges by Monte Carlo simulation," in *Proceedings of the 9th International Conference on Structural Dynamics*, Porto, 2014.

[93] A. Naess, O. Gaidai and O. Batsevych, "Prediction of extreme response statistics of narrow-band random vibrations," *Journal of Engineering Mechanics,* vol. 136, no. 3, pp. 290-298., 2010.

[94] T. Pérez and T. I. Fossen, "Time-vs. frequency-domain Identification of parametric radiation force models for marine structures at zero speed," *Modeling, Identification and Control,* vol. 29, no. 1, pp. 1-19, 2008.

[95] O. Øiseth, A. Rønnquist and R. Sigbjörnsson, "Finite element formulation of the self-excited forces for time-domain assessment of wind-induced dynamic response and flutter stability limit of cable-supported bridges," *Finite Elements in Analysis and Design,* vol. 50, pp. 173-183, 2012.

[96] S. Krenk, "Wind Field Coherence And Dynamic Wind Forces," *IUTAM Symposium on 533 Advances in Nonlinear Stochastic Mechanics: Proceedings of the IUTAM Symposium held in Trondheim,* p. 269–278, 1996.

[97] J. C. J. Kaimal, J. C. J. Wyngaard, Y. Izumi, O. R. Coté and O. R. Cote, "Spectral Characteristics of Surface-Layer Turbulence," *Quarterly Journal,* p. 563–589, 972.

[98] L. Salvatori, Assesment and Migitation of Wind Risk of Suspended-Span Bridge, Firenze, Italy: Faculty of Architecture, Civil Engineering and Environmental Sciences, 2007.

[99] M. Papinutti, K. Aas-Jakobsen, L. H. Kaasa, A. Bruer, M. H. Marley, J. Veie and S. H. Holtberget, "Coupled wind and wave load analyses of multi-span suspension bridge supported by floating foundations," in *IABSE Symposium*, Vancouver, 2017.

(end)